PAWEŁ PODKOPAŁ

INVESTIGATIONS OF THE CHARGE SYMMETRY CONSERVING REACTION $dd \rightarrow {}^{3}He n \pi^{0}$ WITH THE WASA DETECTOR

A DOCTORAL DISSERTATION
PERFORMED IN THE RESEARCH CENTRE JÜLICH, GERMANY
AND SUBMITTED TO THE FACULTY OF PHYSICS, ASTRONOMY
AND APPLIED COMPUTER SCIENCE
OF THE JAGIELLONIAN UNIVERSITY

THESIS SUPERVISOR:
PROF. DR. HAB. ANDRZEJ MAGIERA

CRACOW 2011

PAWEŁ PODKOPAŁ

BADANIE REAKCJI $dd \rightarrow {}^3He n \pi^0$ ZACHOWUJĄCEJ SYMETRIĘ ŁADUNKOWĄ PRZY UŻYCIU DETEKTORA WASA

DYSERTACJA DOKTORSKA
WYKONANA W CENTRUM BADAWCZYM JÜLICH, NIEMCY
I PRZEDSTAWIONA RADZIE WYDZIAŁU FIZYKI, ASTRONOMII
I INFORMATYKI STOSOWANEJ
UNIWERSYTETU JAGIELLOŃSKIEGO

PROMOTOR:
PROF. DR HAB. ANDRZEJ MAGIERA

KRAKÓW 2011

Contents

1 Introduction

Investigations of the charge symmetry breaking (CSB) in strong interaction is one of the most challenging topics in hadron physics. The charge symmetry is an invariance of a system under a rotation by 180° around the second axis in the isospin space. In quantum chromodynamic (QCD) the charge symmetry requires the invariance under exchange of up and down quarks. However, this quarks have different masses and charges, therefore the charge symmetry is not a strict symmetry of the QCD Lagrangian. It may be expected that this elementary sources of the CSB will show up also on the hadronic level. In this way CSB studies may help to connect quark-gluon dynamics to hadronic degrees of freedom, allowing in particular to access the mass difference of up and down quarks. Once those contributions can be treated theoretically, a study of CSB in low energy hadron physics is a unique window to the quark masses and thus to fundamental parameters of the standard model. Desire to find such interlink motivated extensive investigations in which a lot of attention was paid to the experimental and theoretical studies of CSB [1].

Many studies comprise investigations of various nuclear systems and reactions. The first evidence of CSB comes from the difference of the low energy nucleon-nucleon scattering lengths of n-p and p-p systems [2] in the same spin singlet state after necessary corrections for electromagnetic effects. The experimentally determined (Coulomb corrected) 71 keV difference of the binding energies of ^{3}H and ^{3}He may arise from the CSB [2]. Unfortunately in both discussed cases the results are strongly influenced by non-negligible theoretical uncertainties due to the Coulomb corrections. Such problems do not arise for neutron-proton elastic scattering where the effect of electromagnetic interaction is negligible. In these studies the CSB manifests as non vanishing difference of analysing powers for neutron and proton. Very small difference of analysing powers was observed [3–6] indicating CSB in nucleon-nucleon scattering, however still large controversies exist about the origin of CSB in nucleon-nucleon scattering [7–10]. From all such studies it is known that at the nuclear level charge symmetry is broken due to the presence of the electromagnetic effects and due to mass difference in isomultiplets of nucleons and mesons. Net effect of CSB on strong interaction is strongly obscured when investigating nuclear systems. There are, however, some nuclear processes in which CSB is dominated by properties of strong interaction, the best candidates being charge symmetry forbidden $dd \to {}^4\mathrm{He}\pi^0$, which was searched for since many years.

Only recently the first observation of $dd \rightarrow {}^4He\pi^0$ reaction was reported [11] for the beam energies very close to the reaction threshold. At the same time the information on the CSB in $np \rightarrow d\pi^0$ manifesting as the forward-backward asymmetry became available [12]. Those new data triggered also advanced theoretical calculations, which provides the opportunity to investigate the influence of the quark masses in nuclear physics [13]. In order to access such information the advanced calculation within effective field theory are necessary. This becomes possible with the use of chiral perturbation theory (ChPT) [14, 15], which has been extended to pion production reaction [16]. The first steps toward theoretical understanding of $dd \rightarrow {}^4He\pi^0$ reaction have been taken [17, 18]. It was found that the existing data are not sufficient for the precise determination of the parameters of the ChPT and the new data are required. These new data should comprise the measurement of charge symmetry forbidden $dd \rightarrow {}^4He\pi^0$ reaction and charge symmetry conserving $dd \rightarrow {}^3Hen\pi^0$ channel. The measurement of first reaction should be performed at beam energy higher than used in Ref. [11], preferentially with determination of the polarization observables. This would enable to study the contribution of the higher partial waves allowing to extract relevant parameters of ChPT. The measurement of the second reaction is necessary in order to study the relevance of the initial and final state interaction, which strongly influence the results for $dd \rightarrow {}^4He\pi^0$ reaction.

The goal of this thesis was experimental investigation of $dd \rightarrow {}^3Hen\pi^0$ reaction. These studies are an important part of the general program of investigation of CSB in the $dd \rightarrow {}^4He\pi^0$ reaction forbidden by charge symmetry. As there are no experimental data whatsoever for the $dd \rightarrow {}^3Hen\pi^0$, already the information on the total cross section may contribute significantly to the understanding of the CSB sources in the forbidden reaction. The measurements of the full differential cross section for $dd \rightarrow {}^3Hen\pi^0$ reaction may deliver even stronger constraints for the theoretical analysis of the $dd \rightarrow {}^4He\pi^0$ reaction. The measurement presented in this thesis is also a first step toward the experimental investigation of $dd \rightarrow {}^4He\pi^0$ reaction including the polarization observables, which are planned at COSY in the future.

In this thesis the first results for the $dd \rightarrow {}^3Hen\pi^0$ reaction are presented. The experiment was performed with the WASA detection system at COSY accelerator. Chapter 2 is dedicated to the presentation of the present knowledge on the $dd \rightarrow {}^4He\pi^0$ reaction including the existing data and their theoretical analysis. The problems arising from this analysis are presented, which call for the new data on the charge symmetry conserving reaction. In chapter 3 the WASA detection system at the Cooler Synchrotron in Jülich is introduced with extended information on the components used in the present experiment. Chapter 4 describes methods used in the data analysis and the first steps necessary for identification of the investigated reaction. Chapter 5 is devoted to the phenomenological model necessary for the acceptance correction of the experimental data. This model was also used to extract physical information about the reaction mechanism. In chapter 6 the analysis of the data is presented. Final experimental distributions and the comparison of the obtained experimental results with the phenomenological model are discussed in chapter 7. Finally, the summary and conclusions resulting from this work are presented in chapter 8.

2 Data and Theory Overview

The most promising data allowing to access the CSB effects in the strong interaction for hadronic systems are the forward-backward asymmetry measurement in $np \to d\pi^0$ reaction [12] and cross section measurement for $dd \to {}^4He\pi^0$ reaction [11]. In those investigated systems the electromagnetic effects are negligible, allowing direct observation of CSB in strong interaction.

The measurement of $np \to d\pi^0$ reaction was performed at TRIUMF with a 279.5 MeV neutron beam. This beam energy corresponds to only 2 MeV excess energy. Therefore, with the use of magnetic spectrometer, the whole angular distribution was measured by detecting scattered deuterons. CSB manifests as a non-vanishing forward-backward asymmetry:

$$A_{fb} = \frac{d\sigma(\theta) - d\sigma(\pi - \theta)}{d\sigma(\theta) + d\sigma(\pi - \theta)} \tag{2.1}$$

where θ is the c.m. deuteron scattering angle. If charge symmetry holds the forward-backward asymmetry should be zero. This is shown schematically in Fig. 2.1 where the considered reaction is drawn also when exchanging up and down quarks (which corresponds to the exchange of proton and neutron). In order to achieve better accuracy, only angle integrated forward-backward asymmetry was extracted with the final value of $A_{fb} = [17.2 \pm 8.0(\text{stat}) \pm 5.5(\text{syst})] \cdot 10^{-4}$. The reached accuracy is not very high with the statistical deviation of only two standard deviations from zero.

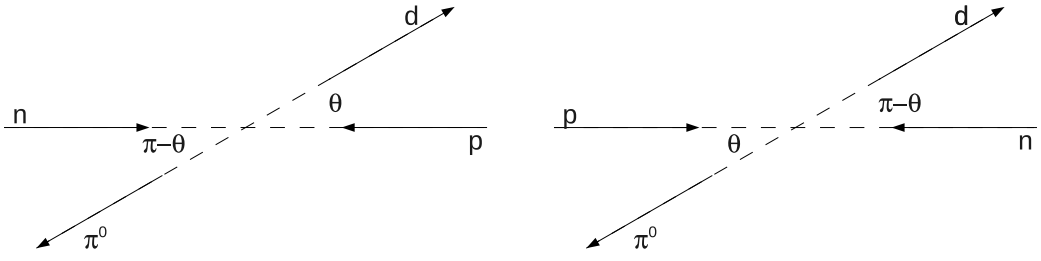

Figure 2.1: Schematic drawing of the $np \to d\pi^0$ reaction demonstrating the symmetry of the process when exchanging up and down quarks.

Among various processes in which CSB may be investigated the reaction dd $\rightarrow {}^4\mathrm{He}\pi^0$ is very well suited for such studies. Since deuteron and ^{4}He have isospin equal to zero and π^0 has isospin equals to one, it is obvious that this reaction is forbidden without isospin symmetry breaking. In self-conjugate systems (which have third isospin component equal zero) a charge symmetric Hamiltonian cannot connect states which differ in total isospin. Therefore the reaction dd $\rightarrow {}^4\mathrm{He}\pi^0$ is also forbidden if charge symmetry holds. The only possibility of CSB due to electromagnetic interaction is isospin 1 admixture to the ground state of ^{4}He nuclei. Such an isospin impurity was estimated to be very small [19] even if not discovered up to now isospin 1 excited state exists. Therefore the observation of the dd $\rightarrow {}^4\mathrm{He}\pi^0$ reaction gives the clear evidence of CSB in the strong interaction only.

Attempts to measure dd $\rightarrow {}^4\mathrm{He}\pi^0$ reaction have been undertaken since many years. The early measurement of this reaction yields only the upper limit for the differential cross section (see Ref. [20] and references therein). In one experiment only at deuteron incident energy of 1100 MeV this reaction was observed [21] with the differential cross section of $d\sigma(\theta_{c.m.}=107^o)/d\Omega = 0.97 \pm 0.20 \pm 0.15$ pb/sr. However, this result was questioned even by some participants of the experiment (Ref. [22]).

The situation was clarified by measurement of the total cross for dd $\rightarrow {}^4\mathrm{He}\pi^0$ reaction at beam energies very close to the reaction threshold [11]. The measurement was performed at two beam energies corresponding to 1.4 MeV and 3.0 MeV excess energy. The background was substantially reduced by coincidence measurement of all reaction products. Outgoing ^{4}He nuclei were detected with the magnetic spectrometer and π^0 was detected with neutral particle calorimeter via its two γ decay. The total cross section reported is 12.7 ± 2.2 pb for lower beam energy and 15.1 ± 3.1 pb for higher beam energy.

Those two independent observations of CSB effects in the np $\rightarrow$ dπ^0 and the dd $\rightarrow {}^4\mathrm{He}\pi^0$ reactions should be analysed within an appropriate theoretical framework in order to extract the information about the microscopic sources of CSB such as e.g. up and down quarks mass difference. A theory collaboration group, aiming at calculation of the CSB effects in hadronic processes has been formed and the work on the theoretical frontier is in progress. The most appropriate theory for such a goal is the Chiral Perturbation Theory [15]. The formalism uses the fact the the interaction of pions with matter is largely controlled by the approximate chiral symmetry of QCD, with pions being the Goldstone bosons resulting from the spontaneous breakdown of this symmetry. In this effective field theory quark and gluon degrees of freedom are replaced by hadronic degrees of freedom. The most general Lagrangian with symmetries the same as the QCD Lagrangian may be constructed with the use of the power expansion in the momenta small to the scale of about 1 GeV. Up to now most work within ChPT was done for the two pion system, the πN system and, more recently, the NN system [14, 23]. In addition, a promising scheme was derived to also analyze pion production in nucleon-nucleon collisions [24–26], and recently to meson production in various reactions [16]. At the present stage ChPT may be also applied to light nuclei and other many-body systems [27]. Since chiral perturbation theory allows for a systematic analysis of hadronic reactions, also the breaking of QCD symmetries can be addressed quantitatively, one example being the isospin. In this way

ChPT has become an ideal tool for the theoretical analysis of CSB in $np \to d\pi^0$ and $dd \to {}^4He\pi^0$ reactions.

The first calculations conducted for $np \to d\pi^0$ using ChPT [28] lead to the predicted effect much larger than observed experimentally resulting from charge symmetry violation in π^0-nucleon interaction. The recent calculations [29] are successful in describing total cross sections, the shape of angular distributions and the analysing power for pion production reactions $np \to d\pi^0$ and $pp \to d\pi^+$. However, they fail in reproducing the forward-backward asymmetry induced by CSB overestimating the data by 2.4 standard deviations. Therefore further theoretical analysis is required and more precise data on CSB in this reaction are necessary.

The first calculations using ChPT were performed for the $dd \to {}^4He\pi^0$ reaction [17] using very simplified model what allowed to identify the most important ingredients necessary for more precise calculations. It was found that at the leading order (LO) only charge symmetry violation in pion re-scattering contributes, there is no next-to-leading-order (NLO) contribution and some next-to-next-leading-order (NNLO) contributions were identified. The diagrams for LO contributions are shown in Fig. 2.2. Diagram (a) in this figure contributes for $\pi^0 - {}^4He$ relative angular momentum equals 0 (*s*-wave) and equals 1 (*p*-wave). Diagrams (b) and (c) may contribute for the *p*-wave only. Calculations were performed for *s*-wave using plane wave approximation in the entrance channel and simplified ^{4}He nucleus wave function. It was found that the contribution from the LO term becomes negligibly small due to spin-isospin selection rules and the symmetry of ^{4}He nucleus wave function. The NNLO terms result in the cross section by one order of magnitude smaller than the experimental one. A value closer to the experimental cross section can be obtained only for surprisingly large value of the graph used to estimate the influence of the short range physics. More reliable calculations were performed [18] using realistic two- and three-nucleon interactions together with the recent advantages of the four-body theory [30–32]. That allowed to properly treat effects of deuteron-deuteron interaction in the initial state and to use realistic ^{4}He bound-state wave function. This calculations confirmed that for *s*-wave the LO contribution is negligible and at NNLO the cross section is of the same order as the value determined experimentally. One of the most important issue was the identification of dramatic influence of initial-state interactions. It necessitates in the new independent measurements providing information on pion-production reactions with the same initial state.

At NNLO new terms with unknown strength contribute to *s*-wave pion production in the $dd \to {}^4He\pi^0$ reaction. Their strength can be fixed by the combined analysis of forward-backward asymmetry observed in the $np \to d\pi^0$ reaction and the $dd \to {}^4He\pi^0$ reaction. However, in order to get a non-trivial prediction of CSB in pion production an additional observable is needed. This missing observable may be provided by CSB *p*-wave pion production in $dd \to {}^4He\pi^0$ reaction. In this case the coupling strengths are given by the leading CSB π-nucleon amplitude (diagram (a) in Fig. 2.2) and the leading CSB π-nucleon-nucleon vertex (diagram (b) and (c) in Fig. 2.2). However, similarly as for the *s*-wave pion production, the contribution of diagram (a) is suppressed as a consequence

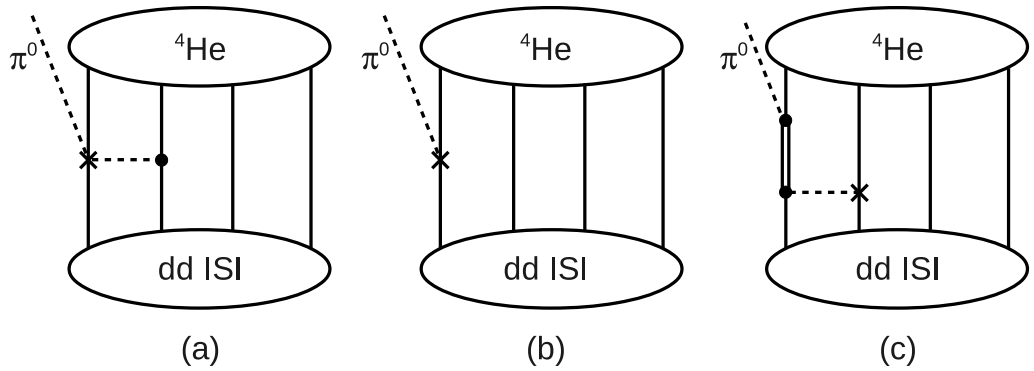

Figure 2.2: Leading-order diagrams inducing strong CSB for dd $\rightarrow {}^4$Heπ^0 reaction. Diagram (a) occurs for *s*- and *p*-waves, while diagrams (b) and (c) contribute only for *p*-wave. The crosses indicate the occurrence of CSB, the dots represent a leading-order charge invariant vertex. Dashed lines denote pions, single solid lines denote nucleons and double solid lines denote Δ.

of selection rules. Therefore *p*-wave pion production provides direct access to the CSB π-nucleon-nucleon coupling constant.

The presented overview of the existing data and the status of the theory demonstrate the necessity of the new measurements that would allow to complete the program of the CSB studies for hadrons. In order to successfully carry out this program and especially to isolate the isospin violating matrix elements of interest, more information on the related isospin conserving interactions is needed. For the dd $\rightarrow {}^4$Heπ^0 reaction a close relative is given by dd $\rightarrow {}^3$Henπ^0. Especially since the initial state is the same, from this reaction important constraints will follow for the initial state interaction to be used in the analysis of the isospin violating channel. In addition, experimental information on this reaction will at the same time help to show how well in general the isospin conserving part of the four nucleon system is understood. In turn the dd $\rightarrow {}^4$Heπ^0 reaction should be measured at higher beam energy, preferentially with the polarization observables which allow to extract unambiguously the *p*-wave contribution directly from the experimental data. This defines the whole experimental program which can be realized at the COSY accelerator. The results of this thesis are the first important step towards the successful execution of the CSB studies.

3 Experimental Setup

The experiment which is described in this thesis was carried out at the Institute for Nuclear Physics of the Forschungszentrum Jülich, Germany. For the measurement the Cooler synchrotron COSY together with the WASA detection system was used. WASA (Wide Angle Shower Apparatus) was originally installed at the CELSIUS storage ring at the TSL in Uppsala, Sweden [33] and was operated until the shutdown of the accelerator in 2005. After the end of the experimental program [34] the facility was shipped to Jülich, Germany. The move was motivated by several significant factors which allowed to continue and enhance the physics program foreseen for CELSIUS. Major advantages of use of the WASA detector in combination with COSY are:

- significantly higher beam momentum up to 3.7 GeV/c (at CELSIUS beam momentum was limited up to 2.1 GeV/c)
- polarized and phase space cooled proton and deuteron beams.

Combining COSY and WASA together we obtained multi-purpose detection system, focused on the investigation of the properties and interactions of nucleons in the strongly nonpertubative region of QCD [35]. After successful installation and first commissioning runs in the fall of 2006 WASA has been taking data since April 2007.

In this chapter a technical overview of the accelerator and the detector systems is given, moreover, the unique pellet target and the data acquisition system is described. The chapter closes with a section where a short overview is given on the different software tools which were used throughout the analysis.

3.1 Accelerator System

The accelerator and storage ring COSY (COoler SYnchrotron) [36] at the Forschungszentrum Jülich can provide high quality polarized and unpolarized, proton and deuteron beams in the momentum range from 295 MeV/c up to 3.7 GeV/c, corresponding to an energy range between 45 MeV and 2.94 GeV for protons, and from 67 MeV to 2.23 GeV for deuterons. The COSY operates in cycles. In each cycle, first the H^- or D^- ions are preaccelerated in the cyclotron JULIC and injected into the storage ring via a charge exchanging stripper carbon foil. In the standard operation up to 10^{11} particles can be stored in the ring, yielding typical luminosities of 10^{31} cm^{-2} s^{-1} for internal experiments. After

filling the ring the ions are accelerated until they achieve desired energy, then the magnetic field is kept stable and particles are stored for a certain time. This part of the cycle is called flat top. At the end of the flat top, the beam is dumped and the dipole magnets are ramped down to injection level, so that a new cycle can begin.

The synchrotron is equipped with two cooling systems. Electron cooling is applied up to 645 MeV/c, while in the higher momentum regime the stochastic cooling [37] is used. They guarantee high quality beams with small emittance and momentum spread which can be used for internal (one of which is the WASA detector) end external experiments. In addition to the cooling of the beam a barrier bucket cavity [38] can be used, to counteract the energy loss induced by the interaction of the beam with the target. The method is quite efficient in case of a target thickness $\geq 10^{15}$ atoms/cm^2 as used by the WASA facility. The layout of the facility is shown in Fig. 3.1. The technical parameters of COSY are gathered in Table 3.1.

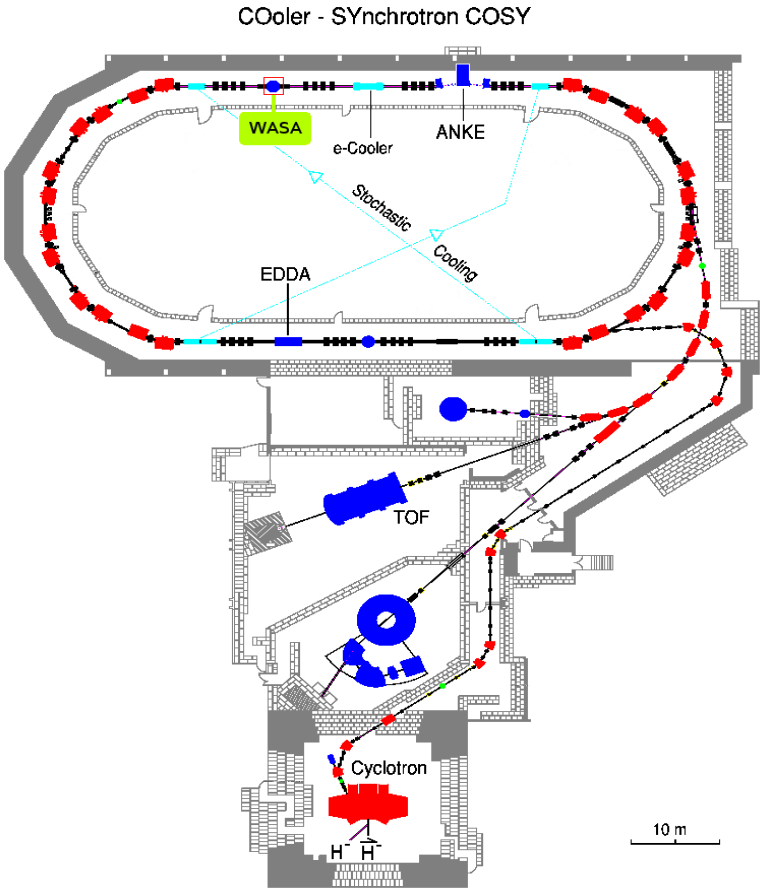

Figure 3.1: The view of the COSY–facility.

The COSY storage ring	
circumference	184 m
number of magnets	24 dipoles, 54 quadruples
momentum range	0.295 GeV/c – 3.7 GeV/c
cooling	electron (p_{beam} <645 MeV/c)
	stochastic (p_{beam} >1.5 GeV/c)
momentum resolution	10^{-3} without cooling
	10^{-4} with cooling
number of particles stored	10^{11} (uncooled, unpolarized)

Table 3.1: Characteristic features of the the COSY synchrotron.

3.2 Pellet Target

The key experiments proposed in the WASA program set high demands on the performance of the target system. Since we want to study rare processes, there are several things which are mandatory for the type of the target to be used. First of all the density should be as high as possible to guarantee luminosities of the order of 10^{32} cm^{-2} s^{-1}. In parallel the background conditions, and secondary interactions within the target have to be kept on low level. To cope with these demands, it is not possible to use conventional gas or cluster jet target, instead pellet target can be used.

The pellet target system was originally developed for the CELSIUS experiment [39] and installed in the TSL in Uppsala, Sweden. After the shutdown of the accelerator the pellet system was transferred to Juelich and assembled in the COSY hall. In 2006, after a lot of tests and optimization steps, first droplet beam was obtained. The construction of the target station have been designed in such a way, that only a thin tube used to guide the pellets is inside the detector while the rest of the apparatus is located outside. This is an

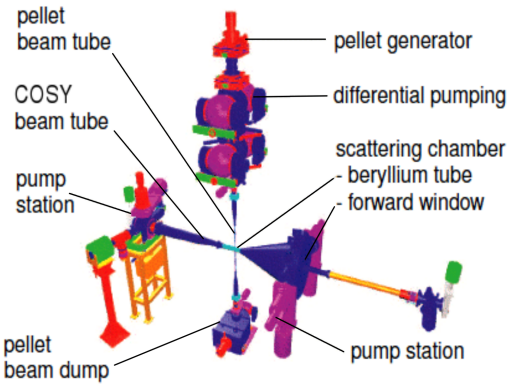

Figure 3.2: The WASA Pellet Target system.

important prerequisite for 4π detection. Figure 3.2 shows a schematic of the Pellet Target system. The pellets (hydrogen or deuterium) are produced in the pellet generator where a high purity liquid jet is broken up into uniformly sized and spaced micro spheres by means of acoustic excitation of the jet nozzle. The droplets freeze by evaporation in the droplet chamber and form pellets which are injected through capillary into the vacuum chamber. Here, the pellet beam is collimated by the skimmer and travels down the narrow pellet tube to the scattering chamber. After passing the interaction point with the COSY beam, the pellets are collected in the cryogenic pellet dump situated below the detector. Some characteristic features of the target are listed in Table 3.2.

The Pellet Target system	
pellet diameter	$\simeq 35\ \mu$m
pellet frequency (at interaction vertex)	5 - 12 kHz
pellet - pellet distance	9 - 20 mm
pellet stream diameter at vertex	2 - 4 mm
pellet velocity	60 - 100 m/s
effective target thickness	$> 10^{15}$atoms $\cdot$ cm^{-2}

Table 3.2: Performance of the Pellet Target.

During the winter shutdown in 2007, first deuterium pellets were produced at COSY, however, at that time the problem with the blocking of the glass nozzle occured. After a lot of investigations the problem was identified with the help of the infrastructure established for glass nozzle manufacturing in the Central Department of Technology (ZAT) at the Forschungszentrum Jülich. It was found that blocking the nozzles was due to debris from sinter filters at the gas input side of the nozzle. This material problem was eventually solved prior to the experiment described in this thesis. In that way a reduction of time necessary for the target regeneration from approximately 12 to only 3 hours was achieved. With a stable pellet beam a deuterium target thickness close to $4{\cdot}10^{15}$ atoms $\cdot$ cm^{-2} and pellet rates up to 10^4 pellets/s were obtained.

3.3 WASA Detector Setup

The design of the WASA detector is optimised to tag a reaction by measuring the forward-going recoil nucleon and nuclei by an array of plastic scintillators and straw tube layers and to identify decay patterns of produced mesons by a straw tube tracker in a solenoidal magnetic field, a barrel of plastic scintillators and a close to 4π electromagnetic calorimeter (see Fig. 3.3). Performing exclusive or semi-exclusive measurements allows an effective discrimination of background channels and a clean event identification.

The position (x,y,z) in the WASA detector is given in a right handed rectangular coordinate system with origin positioned close to the intersection of the pellet beam with the

circulating COSY beam. The *Z*- axis is directed along the beam. The *X*- and *Y*- axes are in the plane orthogonal to the beam. The *X*- axis is directed outwards from the beam ring in the horizontal plane while the *Y*- axis is directed upwards. Two angles can be defined in this coordinate system; the angle measured towards the *Z*- axis is the polar or scattering angle θ, the angle in the (*X*,*Y*) plane is the azimuthal angle φ.

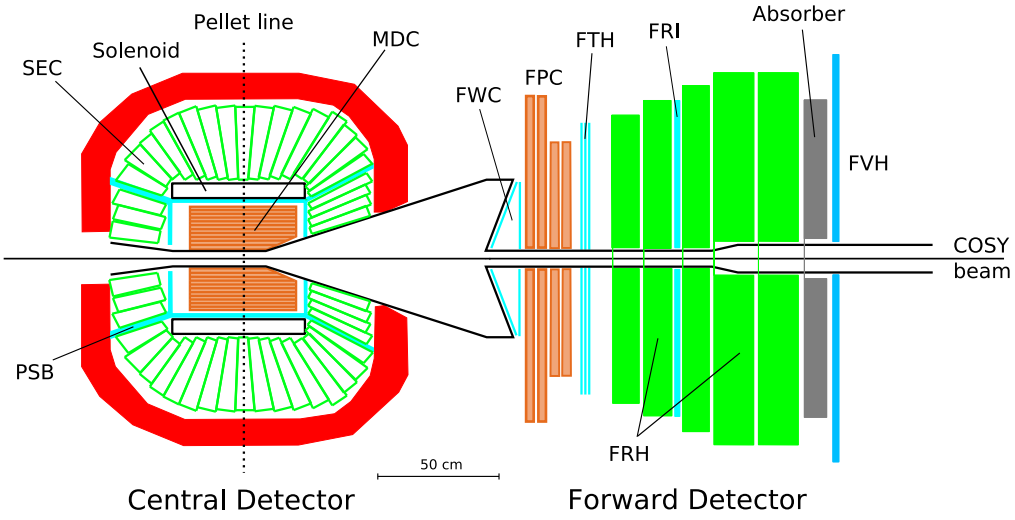

Figure 3.3: Schematic layout of the WASA detector as installed at COSY. The abbreviations used for different detector are explained in the subsequent section.

3.3.1 Forward Detector

The main purpose of the Forward Detector (FD) is the detection of scattered projectiles and charged recoil particles like protons, deuterons and He nuclei. It comprises a set of plastic scintillator detectors allowing for particle identification by means of energy loss and for the determination of the total energy. In addition it consists of a straw tube tracker which provides a precise measurement of angles. Combining these information altogether, the forward detector is capable to reproduce the complete 4-vector of a particle. All FD plastic scintillators may supply information for the first level trigger logic. Some properties of the forward detector are summarized in Table 3.3.

3.3.1.1 Forward Window Counter

The first subdetector of the Forward Detector in beam direction is the Forward Window Counter (FWC). It is located directly behind the scattering window. The FWC consist of two layers made of 3 mm thick BC408 plastic scintillator material (Fig. 3.4). Each

element in first layer is inclined by 20° relative to the plane perpendicular to the beam to follow as close as possible the conical shape of the exit window of the scattering chamber. The second layer is perpendicular to the beam axis and is rotated in φ direction by half an element with respect to the first layer. This geometry provides an effective granularity of 48 elements which coincides with the granularity of the subsequent scintillator detector. This allows for a track reconstruction of forward going particles.

The FWC plays crucial role in the first level trigger. It allows for a very effective selection of events based on the multiplicity of charged tracks. Hits with similar position and time information in subsequent detectors which are pointing to the target region are considered as a good candidates to be accepted by trigger, while the events not fulfilling this condition are rejected. This method significantly suppresses the amount of background caused by secondary interactions in the beam pipe or in the flange at the entrance to the FD. In our experiment it was essential to incorporate the FWC in the trigger for inducing a high threshold on deposited energies in order to separate ^{3}He from protons and deuterons. More detailed information concerning this detector can be found in [40].

The Forward Detector	
number of scintillators	340
scattering angle coverage	2.5° - 18°
scattering angle resolution	$\sim 0.2°$
amount of sensitive material	50 g/cm^2
- in radiation lengths	$\approx$ 1 g/cm^2
- in nuclear interaction lengths	$\approx$ 0.6 g/cm^2
maximum kinetic energy for stopping (T_{stop})	
$\pi^{\pm}$, p, d, ^{4}He	170 / 300 / 400 / 900 MeV
hit time resolution	$\leq$ 3 ns
relative energy resolution	
- stopped particles	1.5% - 3%
- particles with $T_{stop} < T < 2T_{stop}$	3% - 8%
particle identification	ΔE - E, ΔE - ΔE

Table 3.3: Basic properties of the Forward Detector.

3.3.1.2 Forward Proportional Chamber

The Forward Proportional Chamber (FPC) is a straw tube tracker. It is used for accurate reconstruction of track coordinates and for precise determination of the angles of charged particles originating from the target region. It is composed of four modules, each with four staggered layers of 122 proportional drift tubes. The modules are rotated by 90° in the plane perpendicular to the beam with respect to each other. The straws are cylindrical drift tubes made of 26 μm thick, aluminized Mylar foil with the anode wire located in

the coaxial center of the tube. Depending on whether only geometrical information or drift time is used, we can expect a spatial resolution of 8 mm and 200 μm, respectively. In Fig. 3.5 a schematic layout is shown. A detailed description of the FPC can be found in [41].

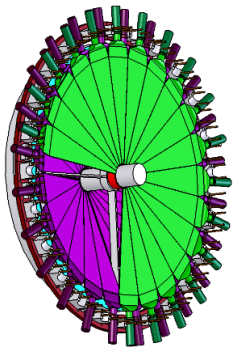

Figure 3.4: The Forward Window Counter.

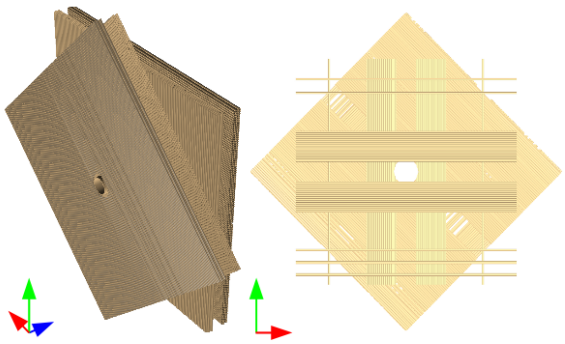

Figure 3.5: The Forward Proportional Chamber, 3D view (left), structure of planes (right).

3.3.1.3 Forward Trigger Hodoscope

The Forward Trigger Hodoscope (FTH) shown in Fig. 3.6 consists of three layers of 5 mm thick, BC408 plastic scintillators. The first layer is segmented into 48 straight, wedge-shaped elements. The second and third layer are assembled from 24 elements, shaped as an Archimedean spirals, oriented clockwise and counter-clockwise, respectively (see Fig. 3.6). The radius of the active surface of FTH is 580 mm, with an inner hole of 48 mm diameter for the beam pipe. The unique geometry of this detector results in a pixel structure obtained by overlap of two or three scintillation detectors. In that way the multi-hit situations can be resolved and the noise contribution is reduced significantly. The fast readout signals are used in the first level trigger in coincidence with the FWC and FRH to settle the charge multiplicity conditions. The FTH detector can be also used for identification of particles like ^{3}He or ^{4}He with kinetic energy below 350 MeV, which are stopped before first layer of FRH. Due to the radiation damage and aging effects of the scintillator material, the FTH detector have been refurbished in 2008 [42].

3.3.1.4 Forward Range Hodoscope

The Forward Range Hodoscope (FRH) is positioned downstream of the FTH. It consists of 5 layers made of plastic scintillator BC400. The first three planes have a thickness of 11 cm, whereas the last two have a thickness of 15 cm. Each plane incorporates 24 elements, read out individually by XP2412 photomultiplier tubes. The main purpose of the FRH

is to measure the energies of the forward going particles. The multi-layered structure of the FRH allows many ΔE - E combinations which are used for particle identification. In addition, FRH supplies the information about the azimuthal angle and the multiplicity, for the first level trigger logic. In the near future, also the usage of the energy will be possible to have as a final trigger output, the information about the missing mass of an event.

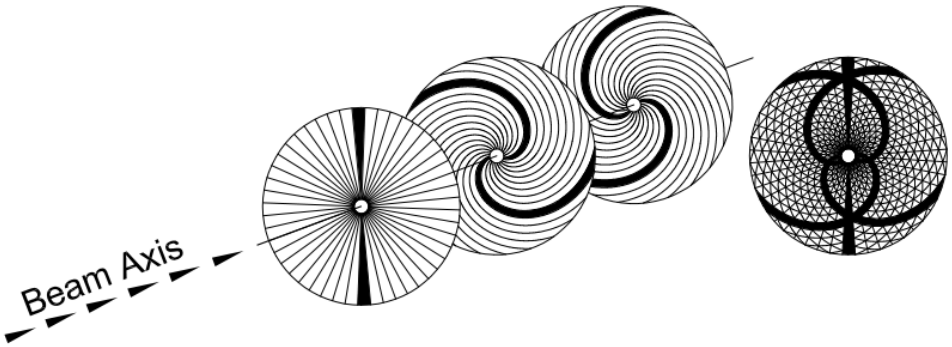

Figure 3.6: The three layers of the Forward Trigger Hodoscope hit by two particles (left), pixel structure obtained from the intersection of the hit modules, projected onto one plane (right).

3.3.1.5 Forward Range Intermediate Hodoscope

The Forward Range Intermediate hodoscope (FRI) is placed between the third and fourth layer of the FRH. It consists of two layers of 5.2 mm thick bars of plastic scintillator. The modules are rotated by 90° with respect to each other, forming rectangular pixels. Its purpose is to deliver precise time and two-dimensional position information. More detailed information about the design and performance of this detector is presented in [43].

3.3.1.6 Forward Range Absorber

The Forward Range Absorber (FRA) is a passive iron absorber positioned directly downstream, after the last layer of FRH. The thickness of this absorber can be adjusted so that protons originating from η production are just stopped in the absorber, whereas higher energy protons produced in background reactions, e.g. multi pion production, penetrate the FRA and induce signal in the FVH which can be used in the trigger to reject those events.

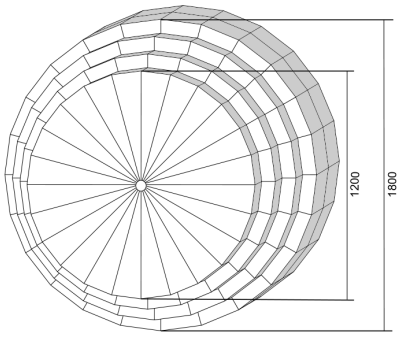

Figure 3.7: The Forward Range Hodoscope, diameters of layers are given in mm.

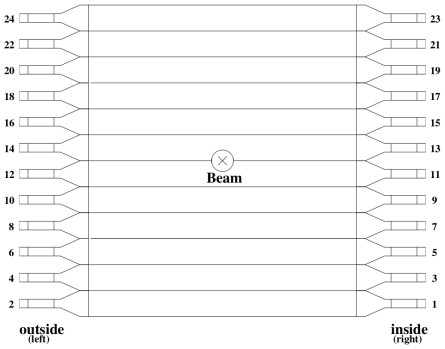

Figure 3.8: Scheme of the Forward Veto Hodoscope.

3.3.1.7 Forward Veto Hodoscope

The Forward Veto Hodoscope (FVH) shown in Fig. 3.8 is the most downstream detector plane in the WASA setup. It consists of 12 horizontal plastic scintillator bars with a thickness of 2 cm and a width of 13.7 cm, equipped with photomultipliers on both sides. The hit position along a bar may be reconstructed from signal time information. In the first level trigger the signals are used for rejection (or selection) of particles punching through the FRH and FRA.

3.3.1.8 Light Pulser Monitoring System

The Light Pulser Monitoring System provides reference light pulses via light fibers to all scintillation counters in order to monitor their gain during the experiment. Since both organic and inorganic scintillators are used, two types of light sources were designed. A xenon flash tube from Hamamatsu is used for the CsI elements of the calorimeter and three LED-based light sources for all plastic scintillators. From those four sources the light signals are transmitted to individual elements via a network of light fibers. A more detailed description of the LPS can be found in [44].

3.3.2 Central Detector

The central detector (CD) surrounds the interaction point and is designed mainly for detection and identification of photons and charged particles produced directly or originating from light meson decays. It consists of an inner drift chamber (MDC) for precise tracking of charged particles, a solenoid (SCS) providing magnetic field for momentum reconstruction, thin plastic scintillators in a cylindrical geometry (PSB) for particle identification and

a CsI calorimeter (SEC) used for energy measurement of neutral and charged particles. The main components of the Central Detector, shown in Fig. 3.3, are presented below in more details.

3.3.2.1 Mini Drift Chamber

The innermost part of the CD is the Mini Drift Chamber (MDC). It is assembled from 17 layers consisting (see Fig. 3.9) of 1738 straw tubes. Each straw tube is made of 25 μm thin aluminized mylar foil and a sensing wire made of 20 μm stainless steel. The straws in nine layers are parallel to the beam axis, and in the remaining eight they are skewed by small angle (6° to 9°) with respect to the beam pipe in order to allow position sensitivity in z-direction. The tubes are filled with a mixture of argon and ethane gases (80% Ar and 20% C_2H_6). Particles passing through the tube ionize the gas mixture and as a result electron-ion pairs are created. Under the action of the electric field the electrons are accelerated towards the anode wire and the ions toward the cathode where they are collected. The signal induced in the wire by electrons is very fast in comparison to the pulse generated by ions and can be used for precise reconstruction of the trajectory of a traversing particle. The MDC is placed within the magnetic field of the superconducting solenoid (see Fig. 3.10), which allows us to determine the parameters of the helix describing the trajectory and reconstruct vertex position, polar and azimuthal angles at the vertex, as well as the momentum of charged particles. More detailed information about momentum reconstruction procedures and performance of MDC can be found in [45].

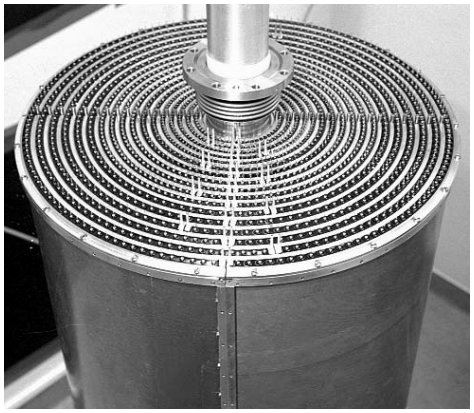

Figure 3.9: The Mini Drift Chamber (MDC) inside the Al-Be cylinder.

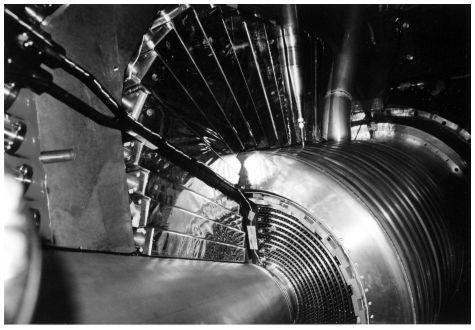

Figure 3.10: The MDC surrounded by PSB elements inside of the solenoid.

3.3.2.2 Superconducting Solenoid

The magnetic field needed for momentum reconstruction in MDC is provided by the Superconducting Solenoid (SCS). The SCS is capable of producing a magnetic field up to

1.3 T. The strength of the field inside of the drift chamber has been mapped by measuring the axial, radial and tangential components of the field with Hall probes. The results of measurement were compared to simulations of the magnetic flux and proper maps of magnetic field were established. In order to maintain the accuracy of energy measurements in the calorimeter, the wall thickness of the solenoid and its cryostat was minimized. The operation temperature of 4.5 K for the coil is provided by the helium refrigerator. The magnetic field is confined by a five ton iron yoke with very low carbon content. The yoke also protects the photomultipliers and the readout electronics from the magnetic field and serves as a mechanical support for the crystals. More information on the SCS can be found in [46].

3.3.2.3 Plastic Scintillator Barrel

The Plastic Barrel is an 8 mm thick layer of fast plastic scintillators, enclosing the Mini Drift Chamber. It consists of a cylindrical central part, formed by 48 scintillator bars, and two endcaps (48 trapezoidal elements each) allowing a close to 4π acceptance. The main purpose of PSB is reliable separation of neutral and charged tracks especially on trigger level, but also later in the event analysis. The deposited energy in the Plastic Barrel is used for particle identification via $\Delta E - E$ method in conjunction with the total energy information from the calorimeter, or via $\Delta E - p$ method using the momentum information from the MDC.

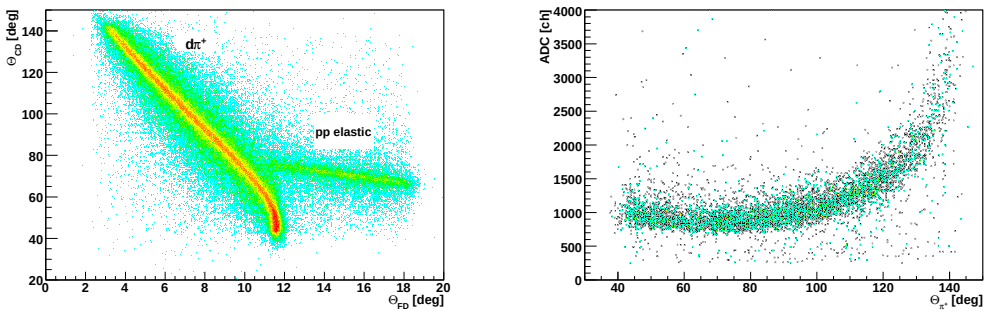

Figure 3.11: Left: Correlation between reconstructed polar angles of particles going to forward and central detector, after applying cuts on deuteron band in FD and coplanarity condition. Angles were reconstructed by means of MDC. Clear sample of $pp \to d\pi^+$ events is visible. Right: The pulse height as a function of polar angle of π^+ for one chosen element of PSB.

The PSB was calibrated using $pp \to d\pi^+$ events selected from data collected with a proton beam of E_{kin} = 600 MeV. For event selection the following criteria were applied:
- a trigger requiring one or more hits in the Forward Range Hodoscope;
- a corresponding hit in the calorimeter (azimuthally matching the hit in PSB);

- one charged track in the Forward Detector;
- cuts on the 2-body angular correlation shown in Fig. 3.11.

In the calibration procedure we exploit fact that for binary reaction the scattering angle and energy are strongly correlated. It implies that π^+ scattered at a certain angle has well defined energy. Therefore, whole PSB detector can be divided into several angular bins, and for each bin, experimentally measured light output can be compared to corresponding energy deposit obtained from MC simulation. Typical light output as a function of scattering angle is presented in right panel of Fig. 3.11. It can be noted that particles which hit the scintillator close to the PMT produce higher light output then particles which are emitted at small polar angle (larger distance to the PMT). This behavior can be attributed to the light attenuation effect (see 4.2.1).

The procedure for obtaining calibration and nonuniformity constants is sketched in Fig. 3.12.For MC simulation and data the mean energy deposit in each bin is obtained by fitting Gaussian function to the deposited energy distribution. This information is used to calculate the averaged ratio between real data and Monte Carlo. Subsequently, the ratio is normalized to unity at the point (in this work 70°) for which the linear calibration constant was extracted. In order to derive the non-uniformity corrections the obtained dependence (see Fig. 3.12) is fitted with an exponential function. This procedure makes use of the fact that the simulation does not account for the light attenuation along the scintillator bars. Having a consistent set of parameters, after the calibration is applied, the real energy can be computed as:

$$E_{dep} = QDC \cdot Calib_{cons} \cdot NU(\theta) \tag{3.1}$$

where $NU(\theta)$ is the non-uniformity correction dependent on scattering angle of π^+, $Calib_{cons}$ is the individual calibration constant and QDC denotes the measured charge (in QDC channels). More details about energy calibration method as well as about performance of PSB detector can be found here [47, 48].

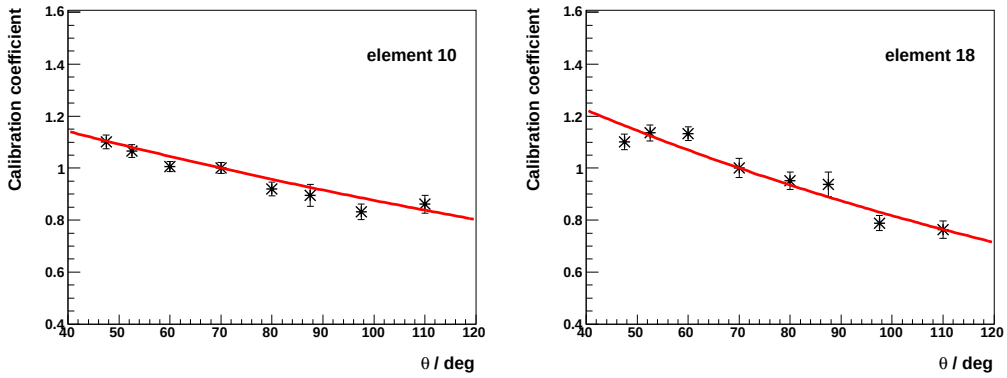

Figure 3.12: Calibration coefficients and non-uniformity of two modules in central part of PSB detector. The light attenuation is parametrized by fitting an exponential function.

3.3.2.4 Scintillator Electromagnetic Calorimeter

The major component of the central detector is the Scintillator Electromagnetic Calorimeter (SEC). The design of the SEC (see Fig. 3.13 and Fig. 3.14) was optimised to provide high-efficiency photon detection with good energy and spacial resolution over an energy range of 5 MeV to 1000 MeV. The SEC detector is assembled from 1012 sodium-doped CsI(Na) scintillating crystals arranged in a vertex-pointing geometry forming the shape of a bubble. All crystals are placed in a 24 circular layers along the beam pipe, covering scattering angles from 20° to 169° what accounts for 96% of the full solid angle. The spherical geometry of the calorimeter was achieved by the usage of trapezoidally shaped crystals with lengths from 20 to 30 cm. The elements are read out individually by photomultiplier tubes. The connection between PMTs which are attached to the outer side of the iron yoke and crystals was obtain via plastic light guides, 120 - 180 mm long. The analog signals from SEC are used in the data acquisition system to enhance the selectivity of the trigger by providing the information (with use of the PSB detector) on the multiplicity of charged and neutral tracks. The calorimeter energy resolution for photons is given by $\frac{\Delta E}{E} = \frac{5\%}{\sqrt{E/GeV}}$ while the angular resolution is limited by the size of a crystal. More details about the geometry, design and performance of the SE are given in [49].

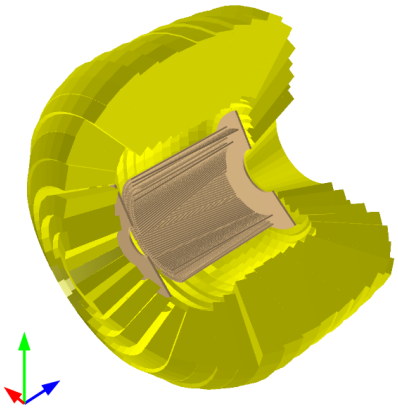

Figure 3.13: Schematic view of the Scintillator Electromagnetic Calorimeter. The Mini Drift Chamber tubes and both forward and backward Plastic Scintillator Barrel end caps are indicated.

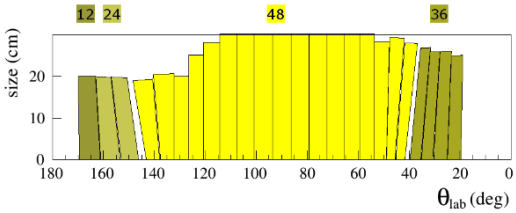

Figure 3.14: Coverage of the polar angle in calorimeter. The shape and size of the CsI crystals for 24 layers are shown, from backward (left) to forward (right) part of the SE. The numbers correspond to the number of crystals in each ring.

3.4 Data Acquisition System

All components of the WASA detector are served by the upgraded data acquisition system (DAQ) designed to cope with the high luminosities. The currently used DAQ system evolved from the second generation of DAQ systems [50] used in experiments at COSY and it was optimized to reach the highest possible event rates. The major development was focused on implementation of new synchronization system and digitization modules. The

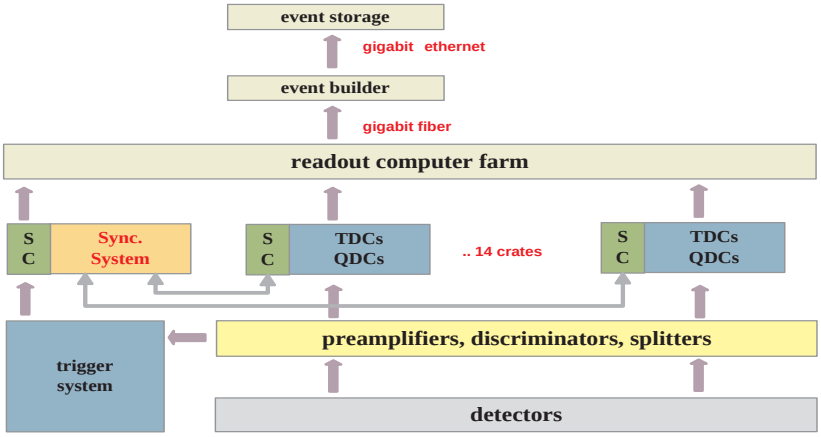

Figure 3.15: Structure of the new DAQ system of WASA detector. The figure is adapted from [50].

new DAQ system of the WASA experiment is hierarchically structured into layers, as illustrated by Fig. 3.15. Signals from the front-end electronics (preamplifier, splitters, discriminators) are connected to the digitizing modules in the 14 crates. Each crate is equipped with an optimized LVDS[1] system bus and so-called system controller (SC) which is responsible for the readout of the digitizing modules and the transfer of data to the readout computer farm. The evaluation of the digitized signals is done by FPGAs. The digitized information is stored in the internal buffers until the valid trigger arrives. This allows trigger delays up to 2 μs and avoids delaying the data signals. When the trigger appears an FPGA selects the digitized signals inside a predefined time interval.

All crates are connected to the readout computer farm via optical links. An event builder collects the data streams from the individual readout systems and writes them in the cluster format to a disc array. Each cluster can contain data from more than one event, thus the decoding of the cluster format into events is necessary. The conversion can be done by the EMS software [51].

[1] Low Voltage Differential Signaling

3.4.1 Read-Out Electronics

The main purpose of the read-out electronics is to convert the analog signals of the detector components into digital information. In case of the WASA facility all analog signals from the plastic scintillator detectors are transmitted via coaxial cables, to the active or passive splitters. There, the signals are distributed into two branches. One branch feeds the signals to the continuous-sampling front-end FastQDCs modules equipped with 12-bit ADC converters running at 160 Msamples/s while the other branch delivers the signals to the leading edge discriminators. The logic signals from discriminators are passed to the long-range TDCs for hit time measurement. The 64 channel module based on the GPX ASIC is multi hit capable, this means time information for several hits within certain time window relative to the trigger can be stored. Additionally, all logic signals are also passed to the trigger logic described in next section.

Due to the different shape of the pulses derived from the calorimeter, special kind of SlowQDCs modules with a sampling rate of 80 MHz have been developed. In both types of QDCs the charge integration is done in FPGA. In addition, double pulse detection, baseline information, pedestal subtraction and time stamping by zero crossing detection is performed. To extract time information from calorimeter an algorithm for time-stamping provided by FPGA is used. In case of faster signals from the plastic scintillators in forward detector the TDCs channels are required, which are connected to the corresponding discriminator outputs.

For the measurement of the drift time of the straw tubes in the WASA detector system, a 64 channel TDC module based on the F1 ASIC was used, which already had been developed for the ANKE [52] experiment. Before the signals reach the LVDS inputs of the TDCs, they are amplified and discriminated by CMP-16 chips.

3.4.2 Trigger

One of the most crucial challenges of the experiment is the proper set-up of the trigger which allows to retrieve the information related to the events of interest. It is obvious that data acquisition is not fast enough to record all events which are registered in the detectors therefore, some kind of event selection must take place.

The WASA trigger system is based on a set of multiplicity, coincidence and track alignment conditions which have to be fulfilled in order to accept the event. In the Fig. 3.16 a flow chart of the trigger system is shown.

During data taking for this experiment there were two trigger levels, both implemented in hardware. The first trigger level is intended for triggering the hardware acquisition, and for generating gate and control signals for the front end electronics. The signals of the plastic scintillator detectors are passed to the multiplicity units where the clustering of neighboring hits takes place (up to four clusters in each detector plane can be detected). In the next step geometrical overlap between clusters in FWC, FTH, and FRH is performed and a set of primary triggers is produced. The simple multiplicity sig-

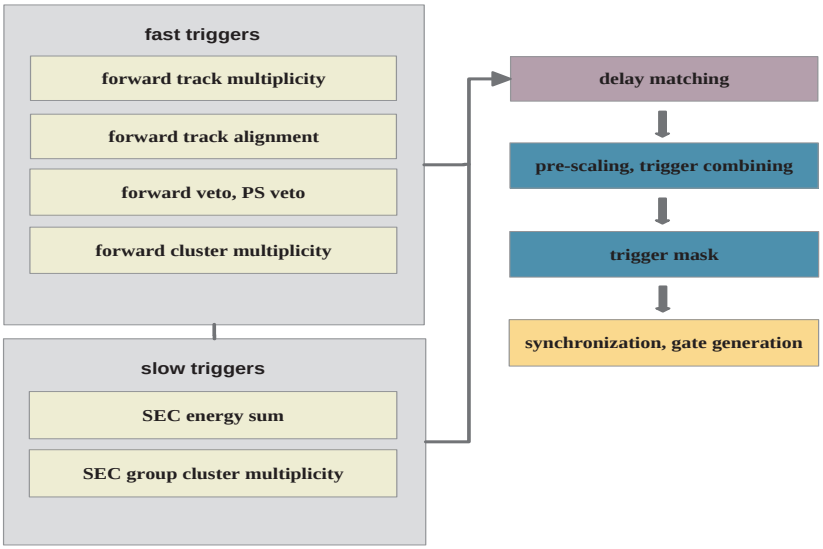

Figure 3.16: Structure of the new trigger system of WASA detector.

nals are combined in coincidence matrices to form more complex trigger expressions after individual delay matching in programmable delay units.

The purpose of the second level trigger is to increase selectivity of the accepted events by using additional information about cluster multiplicity and total energy sum [53] in the calorimeter. A cluster in the SEC is defined as a group of hits in adjacent elements, while a multiplicity of clusters can be associated with the number of possible meson decay products. Additionally, to distinguish charged clusters among neutral, the geometric overlap of the crystals and coincident hits in PSB is checked. In SEC the analog sums are obtained from groups of signals corresponding to 16 crystals in the central part of the calorimeter, 12 crystals in the forward and 9 in backward part. The summed signals are evaluated by a dual threshold discriminator giving logic signals for low and high energy deposits.

The balance of the event rates is achieved by prescaling all high rate triggers. The triggers are connected to a trigger selector unit with 48 trigger inputs. It has 4 programmable 48 bit masks, connected to one OR output each. The masks allow to set in parallel, up to 32 different coincidence conditions which can activate the readout. The logic output signals of all trigger channels are passed to an additional FastTDC and this information is used later in the offline analysis to determine which trigger was responsible for starting the data acquisition.

4 Event Reconstruction

4.1 Analysis Framework

The software used for the analysis is split into three main packages which allow for event reconstruction, Monte Carlo detector simulation and event generation. In following section, the role of individual programs in the process of data analysis will be briefly discussed. For better understanding, the flow chart showing the consecutive steps in the analysis chain is presented in Fig. 4.1.

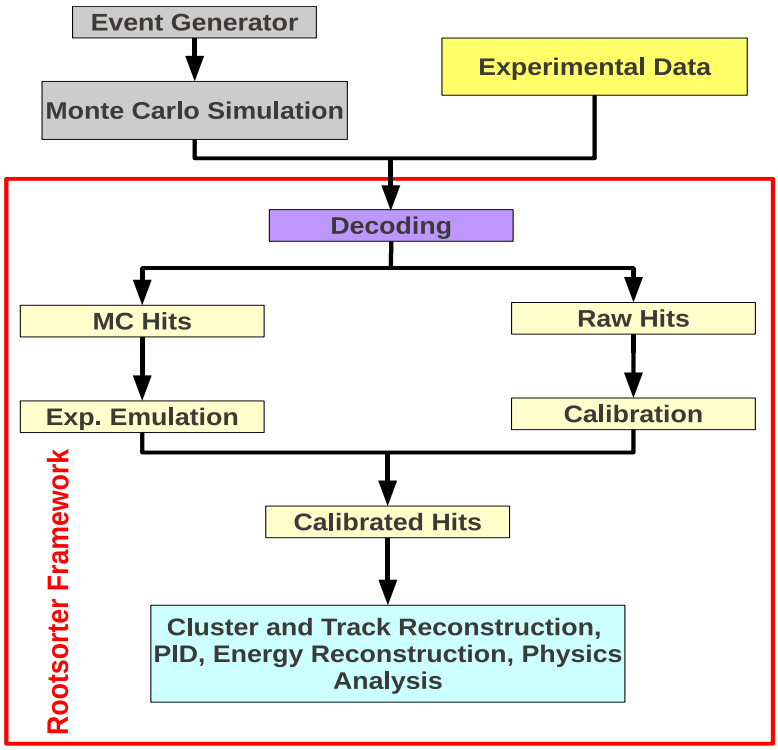

Figure 4.1: Flow chart of the analysis chain.

4.1.1 Event Generator

In this thesis for an event generation the Pluto++ package [54] was used. It is aimed at the study of hadronic interactions from pion production threshold to intermediate energies of a few GeV per nucleon. Originally it was designed mainly for the HADES [55] experiment, but with the time software evolved and now other collaborations like WASA or CBM2 [56] are using Pluto++ to perform simulations. The package consists of a collection of C++ classes and is entirely based on the ROOT [57] environment. After the user specifies the reaction channel, Pluto generates kinematically allowed sets of momentum 4-vectors for all final state particles. The calculation of homogeneous and isotropic phase space is based on the GENBOD [58] procedures. If there is no any specific reaction dynamics defined, kinematical weight per generated event is constant. When any distribution in the phase space is expected to follow a certain reaction model, the aforementioned weight is multiplied by a factor according to the model parametrization. This weight has to be considered during the analysis. Pluto++ offers several elementary reactions where the angular distribution models based on the parametrization of existing data are included, however for more complicated channels the event generator should be adapted to the corresponding physics by the user.

In case of dd $\rightarrow$ ^{3}Henπ^0, the reaction is composed of two possible reaction mechanisms: the direct production with the three-body phase space and the production in pd subsystem with a spectator neutron stemming from the deuteron beam or the deuteron target. The quasi-free reactions mean that only one of the nucleons in the deuteron is participating in the interaction while the other does not take part in the momentum transfer (see Fig. 4.2). This is to some extent the consequence of the small binding energy of the deuteron.

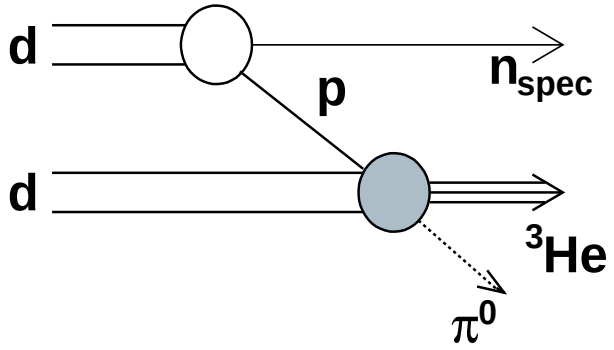

Figure 4.2: Quasi-free model for a particle production reaction via dd $\rightarrow$ n$_{sp}$^{3}Heπ^0.

4.1.2 Quasi-Free Process

In this work for parametrization of the quasi-free reaction, the empirical angular distribution and energy dependent cross section from [59] were included. Authors of the cited publication measured reaction $\vec{d}p \to {}^3He\pi^0$ at twenty beam energy settings from 397.35 MeV up to 429.75 MeV. For each energy the differential cross section was fitted with the following function:

$$\frac{d\sigma}{d\Omega} = \frac{\eta m_\pi}{3p_p}\left(A_0^2 + 2B_0^2 + 2\eta A_0|A_1|\cos\varphi\cos\theta + |A_1|^2\eta^2\cos^2\theta\right) \tag{4.1}$$

where $A_0, |A_1|, \varphi, B_0$ are parameters for which the fit function best matches all data. The θ is the angle of ^{3}He in d-p c.m. system (see Fig. 4.3), η and p_p can be calculated as:

$$\eta = \frac{p_\pi}{m_\pi} \tag{4.2}$$

$$p_p = \sqrt{(s-(m_p+m_d)(m_p+m_d))(s-(m_p-m_d)(m_p-m_d))/4s} \tag{4.3}$$

where p_π denotes the pion momentum in global c.m. system and s stands for the square of total energy. To understand how these informations were incorporated in the generator, the crucial parts of implementation of the quasi-free process for the case of neutron being a spectator from target will be explained. In the first step the considered reaction is subdivided into a spectator and the quasi-free sub-reaction:

$$\mathbb{P}_d^b + \mathbb{P}_d^t \to \mathbb{P}_{sp} + \mathbb{P}_x \tag{4.4}$$

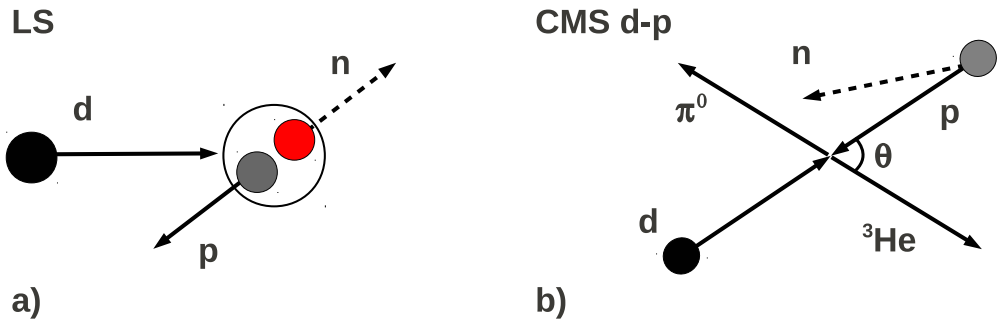

Figure 4.3: Simplified sketch of the deuteron-deuteron collision in the quasi-free model visualized in the laboratory system (left). Quasi-free process represented in the deuteron-proton center of mass system. The θ angle shown in the picture corresponds to the ^{3}He emission angle in reaction $\vec{d}p \to {}^3He\pi^0$ (right).

with $\mathbb{P}$ marked with subscripts being the four-momentum of the beam, target, spectator and sub-reaction, respectively. In order to assure reasonable speed of computations and

to get directly from the generator absolutely normalized cross-section, the map of the probabilities for pairs [$\vec{p}_{fermi}$, cosθ] in the form of two dimensional histogram was prepared (see Fig. 4.4). On the z-axis, expression $\sigma(\eta)$ denotes the total cross section as a function of η while term $p(\vec{p}_{fermi})$ is used to populate the momenta of nucleon inside the deuteron according to Fermi distribution. For the latter, an analytical parametrization of the deuteron wave function [60] based on the Paris potential (see Fig. 4.4) was exploited. For parametrization of the total cross section data presented in Ref. [59] and Ref. [61] were used. Integration over $\vec{p}_{fermi}$ and cosθ of the distribution presented in Fig. 4.4, results in the total cross section $\sigma_{tot} = 580\,nb$ for $dd \rightarrow {}^3He n\pi^0$ reaction at beam momentum 1.2 GeV/c with the neutron being the spectator from the target. This information makes possible to perform absolute normalisation of any spectrum produced from the generator. The benefit is that one can compare normalized data directly with the generator output and judge about the contribution of the quasi-free process. To calculate $\sigma(\eta)$ in the generator we need to compute invariant mass s_x of the system ${}^3He + \pi^0$. Knowing the spectator four-momentum vector $\mathbb{P}_{sp}$ and making use of the energy and momentum conservation we can write:

$$\mathbb{P}_x = \mathbb{P}_d^b + \mathbb{P}_d^t - \mathbb{P}_{sp} \tag{4.5}$$

$$s_x = |\mathbb{P}_x|^2 \tag{4.6}$$

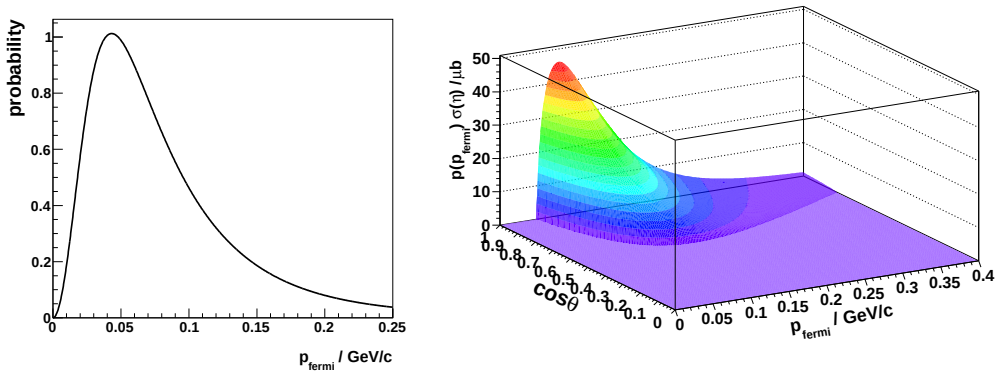

Figure 4.4: Fermi distribution of nucleon momentum inside the deuteron (left). Map of the probabilities for pairs (p_{fermi}, cosθ). Function $p(p_{fermi})$ is used to populate the momenta of nucleon inside the deuteron according to Fermi distribution. The $\sigma(\eta)$ term expresses the total cross section as a function of η (right).

Considering the Eq. 4.2 one sees that η is a function of the pion momentum which can be calculated as:

$$p_\pi = \sqrt{((s_x - m_{^3He}^2 - 4m_{\pi^0}^2)^2 - m_{^3He}^2 \cdot m_{\pi^0}^2)/4s_x} \tag{4.7}$$

The following description refers to the situation where we have neutron as a spectator from target. If one wants to focus on case where spectator is stemming from the beam, then

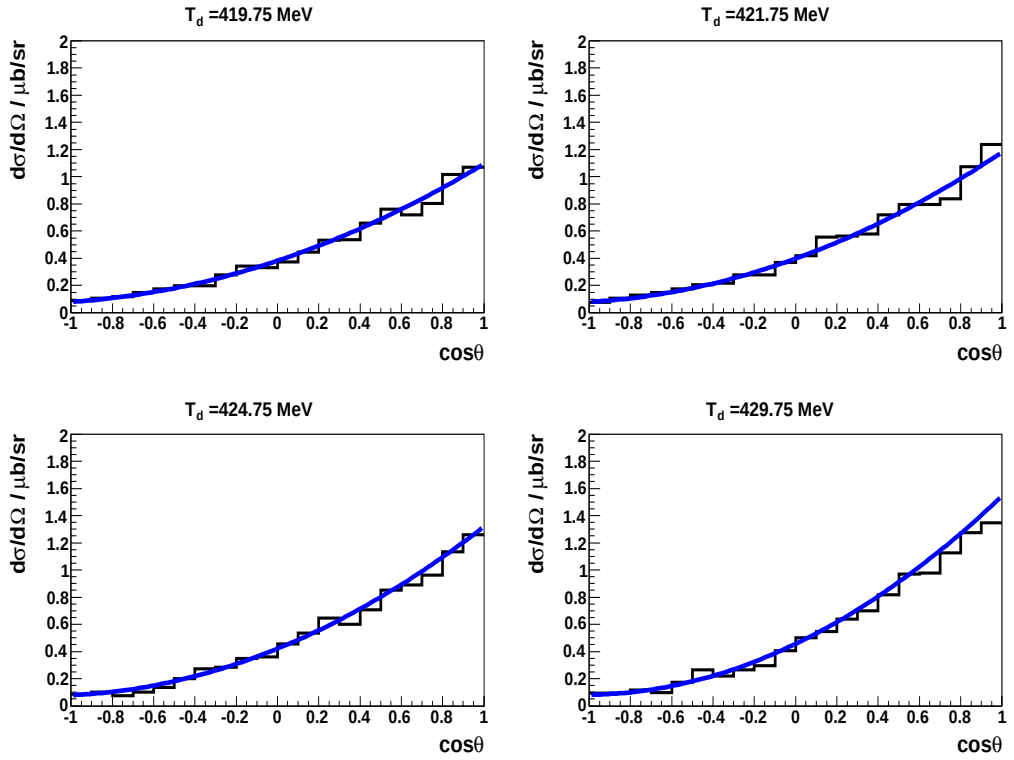

Figure 4.5: Differential cross section (black lines) obtained from Pluto for few selected beam energies. On each spectrum function 4.1 fitted to the data of Ref. [59] is superimposed (blue lines).

additionally, Lorentz boost of the $\mathbb{P}_{sp}$ to the beam system should be performed. In the main event loop the direction and Fermi momentum of the participant nucleon is determined according to the distribution presented in Fig. 4.4. In the deuteron rest frame, participant moves in opposite direction to the spectator having the same momentum. Finally, the subreaction $X \rightarrow {}^3He\pi^0$ is processed. As this is a 2-body reaction, the momenta of ${}^3He$ and π^0 in global c.m system are determined only by the mass of subsystem X. In order to sample events with a specified angular distribution the rejection method [62] has been applied. To make use of it, the function from Eq. 4.1 was normalised at $\cos\theta = 1$ to one and random number $N \in (0,1)$ was generated. In the subsequent step the loop where the $X \rightarrow {}^3He\pi^0$ is placed is repeated till the random value N is larger than the normalised cross. Events which satisfied following criterion have expected angular distribution. After the event loop is finished the four momentum vectors of all particles are transformed to the laboratory frame by means of Lorentz transformation and saved for further processing.

To check the quality of angular parametrization in the generator we tried to reproduce cross section presented in [59]. The function 4.1 perfectly describes the data what means

that if one had implemented it in the generator than obtained angular distribution should reproduce the data points in the exact way. Before the comparison, all spectra from the generator has been normalised accordingly. The agreement between function 4.1 describing the data of Ref. [59] and output from the generator is shown in Fig. 4.5. As can be seen there is no discrepancy what implies that parametrization was successfully incorporated.

4.1.3 Event Generator Based On Partial Wave Decomposition

In order to describe the data, apart from the quasi-free model the partial wave expansion for dd $\rightarrow {}^3\mathrm{He}n\pi^0$ reaction has been developed (see Section 5.4). As a result the production amplitude was decomposed according to the angular momenta of the final state particles. This information was used to implement appropriate matrix element in 3-body generator. Taking the angular momenta $\vec{L}_{23}$ of particle 2 in subsystem 2-3 and $\vec{L}_1$ of particle 1 in global CM we can list the seven partial wave contributions which have been incorporated in the generator. According to the formula for four-fold differential cross section (see Eq. 5.17 in Section 5.4.2) the following matrix elements presented in Tab. 4.1 were implemented in 3-body generator. The implementation of 3-body generator based

$H_0 = \|T\|^2 \propto$ constant	sS wave ($\vec{L}_1 = 0, \vec{L}_{23} = 0$)
$H_1 = \|T\|^2 \propto \|\vec{p}\|^2 cos^2\theta_p$	sP wave ($\vec{L}_1 = 0, \vec{L}_{23} = 1$)
$H_2 = \|T\|^2 \propto \|\vec{p}\|^2 sin^2\theta_p$	sP wave ($\vec{L}_1 = 0, \vec{L}_{23} = 1$)
$H_3 = \|T\|^2 \propto \|\vec{q}\|^2 cos^2\theta_q$	pS wave ($\vec{L}_1 = 1, \vec{L}_{23} = 0$)
$H_4 = \|T\|^2 \propto \|\vec{q}\|^2 sin^2\theta_q$	pS wave ($\vec{L}_1 = 1, \vec{L}_{23} = 0$)
$H_5 = \|T\|^2 \propto \|\vec{q}\|\|\vec{p}\| cos\theta_q cos\theta_p$	interference sP and pS
$H_6 = \|T\|^2 \propto \|\vec{q}\|\|\vec{p}\| sin\theta_q sin\theta_p cos\varphi$	interference sP and pS

Table 4.1: The matrix element parametrisation based on partial wave formalism applied for dd $\rightarrow {}^3\mathrm{He}n\pi^0$ reaction.

on partial wave decomposition has been done as a two-step process. First the reaction $\mathrm{d}+\mathrm{d} \rightarrow 1+\mathrm{X}_{23}$ is sampled and one dimensional histogram containing probability distribution for invariant mass of two-particle intermediate system is created. In the second step the reaction $\mathrm{X}_{23} \rightarrow 2+3$ is processed. Let's denote the mass of subsystem X_{23} by M_{23}, one can write that M_{23} may vary between the limits $\mathrm{M}_2+\mathrm{M}_3 \leq \mathrm{M}_{23} \leq \mathrm{s}-\mathrm{M}_1$, where s corresponds to the square of the total energy. In order to construct the probability distribution of M_{23} the loop over all possible masses is processed and each entry in the histogram is weighted according to $\mathrm{p}^{2\mathrm{L}_{23}+1}\mathrm{q}^{2\mathrm{L}_1+1}$, momenta p and q are calculated using Eq. 5.1. The kinematics of the reaction $\mathrm{d}+\mathrm{d} \rightarrow 1+\mathrm{X}_{23}$ can be written in terms of four-momentum vectors as:

$$\mathbb{P}_{\mathrm{d}}^{\mathrm{b}} + \mathbb{P}_{\mathrm{d}}^{\mathrm{t}} \rightarrow \mathbb{P}_1 + \mathbb{P}_{23} \tag{4.8}$$

In the generator this decay is implemented in the global CM system, thus from the momentum conservation we can write:

$$\vec{p}_1^{\,*} = -\vec{p}_{23}^{\,*} \tag{4.9}$$

Based on that, we can express four-momentum vectors in the global CM system as:

$$\mathbb{P}_1^* = (\sqrt{(M_1^2 + |\vec{p}_1^{\,*}|^2)}, \vec{p}_1^{\,*}) \tag{4.10}$$

$$\mathbb{P}_{23}^* = (\sqrt{(M_{23}^2 + |\vec{p}_1^{\,*}|^2)}, \vec{p}_1^{\,*}) \tag{4.11}$$

where M_{23} is sampled from the histogram which contains the probability distribution of having correctly distributed masses in subsystem X_{23}. The momentum $|\vec{p}_1^{\,*}|$ in the global CM system may be calculated in following way:

$$s = |\mathbb{P}_d^b + \mathbb{P}_d^t|^2 \tag{4.12}$$

$$E_1^* = (s - M_{23}^2 + M_1^2)/2\sqrt{s} \tag{4.13}$$

$$|\vec{p}_1^{\,*}| = \sqrt{E_1^{*^2} + M_1^2} \tag{4.14}$$

In parallel, the angular distribution for particle denoted as "1" is sampled. The azimuthal φ angle is evenly distributed in the interval $[0, 2\pi]$, while scattering angle θ follows the $\sin^2\theta$ or $\cos^2\theta$ function if we are interested in *p*-wave. In case of *s*-wave, $\cos\theta$ is sampled from isotropic distribution. The similar operations are conducted for $X_{23} \to 2+3$ process. First the momentum of particle indicated as "2" is calculated in the rest frame of subsystem X_{23} and the angles φ and θ are sampled isotropically. Since we are in CM system, we have complete information to construct four-vector of particle marked as "3". What's left to be done is to sample angular distribution for particles in subsystem X_{23} according to expected partial wave contributions. This has been achieved by employing the rejection sampling [62] method. After the event loop is finished the four momentum vectors of all particles are transformed to the laboratory frame by means of Lorentz transformation and saved in ROOT Trees [57] format.

4.1.4 WASA Monte Carlo

The WMC detector simulation is based on the GEANT3 [63] software package, which was originally designed for the high energy physics experiments. The GEANT program simulates the passage of elementary particles through the matter using Monte Carlo techniques. Before starting simulation user has to provide set of parameter files which contains description of the detector geometry used in the experiment. Here the definition of shapes and materials of all active detector elements, e.g. scintillators, as well as all passive ones like scattering chamber or beam pipe should be included.

The WMC reads the information about the particle four-vectors from the output of the external event generator. Those particles are then tracked through the detector and their

interaction with the active and passive detector material is simulated by taking into account the energy losses, multiple scattering, decays and other processes with known cross sections. The scintillator response and hence the light output depends on efficiency for converting ionization energy to photons. This effect is called quenching and it is a complex function of mass, charge and energy of the incident particle. The WMC compensates this effect by modifying the energy losses using semi-empirical Birks's formula [64]. The processes like light attenuation in the scintillators, response of photo multiplier tubes or electronic noises are not implemented in the WASA Monte Carlo. The match between simulations and the response of the detector can be obtained via smearing of the simulated observables. The parameters used for smearing are defined in proper filters which are applied in the analysis program.

The output from the WMC is saved in a format which is comparable to the one used for experimental data and therefore can be analyzed by the same reconstruction program. The original four-vectors of the generated particles are also written to the WMC output together with vertex position. Those informations allow for study the reconstruction efficiency, resolution and detector acceptance.

4.1.5 RootSorter

The analysis of simulated data as well as experimental data files was performed within the event reconstruction software framework called RootSorter [65]. This is an analysis tool, based on the ROOT platform, entirely written in C++ using object oriented programming techniques. The modular structure of the software guarantees flexible analysis code management. The essential concept of RootSorter is to hold the experimental raw data as well as calibrated ones and also analysis results like clusters or tracks in class objects with common interface. The specific filters reads and interprets data from external sources (e.g. EMS event stream), decode these data and put proper information in the correct data object. In the first step of event reconstruction the assignment of data from converter modules to the according subdetectors is performed, the time and energy information is combined into hit objects and saved to the so-called RawHitBanks. In case of simulations the Monte Carlo data are stored in a MCHitBanks. At this stage treatment of experimental data and the simulated data varies. Data from the experiment have to be calibrated, TDC information is converted to time and QDC signals into deposited energy. Hits with informations outside the predefined allowed regions are discarded. The necessary parameters for the calibration are stored in a central MySQL database. They have unique tag which specifies for what period of data taking they are valid. The obtained calibration on hit level is not final since some calibration procedures depend on higher level reconstruction, however it can be used to proceed with cluster and track finding algorithms. To match the Monte Carlo simulation with the real data, set of smearing factors is applied and tuned until the experimental resolution is reproduced. After this procedure simulated and experimental data are handled identically during further steps of the analysis.

The RootSorter framework offers a user set of low level utilities which are designed for online monitoring of the data during experiment. The implemented client-server mechanism allows to connect running analysis from any host and guarantees the access to all histograms.

4.2 Detector Calibration

4.2.1 Plastic Scintillators In Forward Detector

Before we focus on the calibration method let us survey some of basic effects which occur when the scintillator material is struck by charged particle. One of the most important phenomena which can be observed during passage of the particles through the scintillation detector is their energy loss as result of atomic collisions. The consequence of the latter is the ionization or excitation of the atoms in the material. When the atoms deexcite, photons are emitted. The light is transmitted to the photomultiplier where it is converted into a weak current of photoelectrons which is then further amplified by an electron-multiplier system. Under the action of electric field, electrons are accelerated towards the anode from which the electric signal can be taken. The height of the pulse is proportional to the number of photons impinging on the photocathode. When we assume that the light collection efficiency of the scintillator is one hundred percent and the photomultiplier is a linear device then the amplitude of the pulse is proportional to the energy deposited in the scintillator by the incoming particle. This makes the scintillators a suitable instruments for measurement of particle energy. However, in the reality, this linear relation does not hold and one has to take into account several effects which cause deviations. First of all the the light collection depends on the geometry of the detector and on the absorption caused by the scintillator material. The latter begin to play severe role when the dimensions of the counter are such that the total path length traversed by the photons is comparable to the attenuation length[1]. In general also the light yield for given energy depends on different types of particles. Moreover, for given particle type it does not always vary linearly with the energy. This effect is known as a quenching and can be associated with interactions between excited molecules created along the way of incident particle. As the result a fraction of the energy which would transform into luminescence is diminished. According to [64] the amount of fluorescent light emitted per unit path length $\frac{\mathrm{dL}}{\mathrm{dx}}$ as a function of deposited energy $\frac{\mathrm{dE}}{\mathrm{dx}}$ is given by the formula:

$$\frac{\mathrm{dL}}{\mathrm{dx}} = \frac{\mathrm{A}\frac{\mathrm{dE}}{\mathrm{dx}}}{1 + \mathrm{kB}\frac{\mathrm{dE}}{\mathrm{dx}}} \tag{4.15}$$

where A is a scintillation efficiency and kB is a constant that depends on the particle type and the material. Another important effect which should be considered is the non linear response of the photomultiplier. It occurs mainly for huge pulses due to space charge

[1] The attenuation length is defined as length after which the light intensity is reduced by factor e^{-1}.

effects or the high voltage fluctuations between the dynodes. Finally, one has to check if there are no any time dependent effects. This can be done by selecting particles which have well defined energy deposit in the detector and checking if there was a drift of the energy deposit peak within a long time scale. If any of these effects is recognized in the data then it has to be parametrised and corrected on the calibration level.

In this experiment in order to do the particle identification via ΔE - ΔE technique, the energy calibration of the plastic scintillator detectors in both layers of FWC and first layer of FTH has been performed. The calibration procedure starts with the parametrization of the light output of protons stemming form the quasi-free elastic scattering dd $\rightarrow$ ppnn reaction as a function of the scattering angle. Due to the kinematics those protons have fairly constant specific energy loss independent from the scattering angle. It implies that any deviations from a constant light output can be associated to a non uniform light collection efficiency. The light output of the one module in FWC detector as a function of scattering angle is shown in Fig. 4.6. Here, in order to get rid of the dependence on the

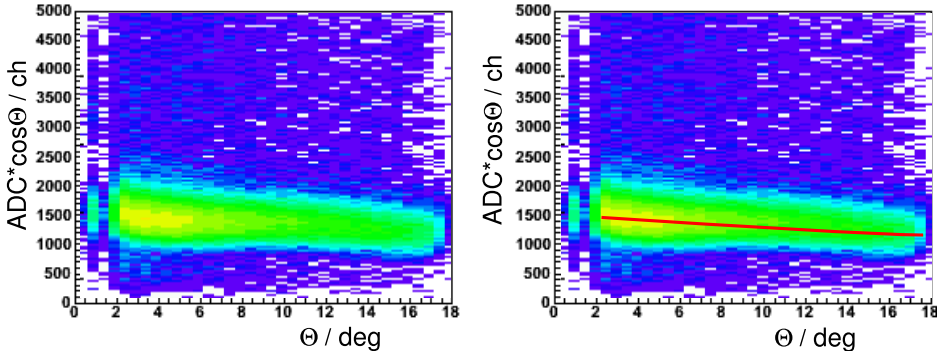

Figure 4.6: The light output for protons originating from quasi-free elastic scattering as a function of the scattering angle in one module of the FWC detector (left). In the right panel the same dependence is plotted but additionaly the polynomial (red curve) of second order which was used for parametrisation of the nonuniformity is presented.

path length traveled by protons the ADC content is multiplied by cosθ. In case of FWC detector the light output distribution was parametrized with a polynomial of second order as it is shown in the right panel of Fig. 4.6. What one sees there, slightly contradicts a naive intuition that the light collection efficiency will raise while increasing polar angle. This manner of thinking assumes that if the particle hits the module at a small polar angle, the emitted photons are less likely to reach the PMT then in case where element is struck at a large angle close to the photocathode. It is true in case of scintillators which have a shape of rectangular bars. Since the FWC modules are pizza-like this makes geometrical focusing effects, hence the light collection is slightly higher near the tip of the element which corresponds to the small polar angles. To correct for the non-uniformity of the light output in the first layer of the FTH detector similar procedure has been applied. The only difference was that for the parametrization, higher orders of polynomial have been used.

The fact that we have in total 96 modules to be calibrated, yields in huge amount of calibration constants. Thus, to minimize the number of constants, the relative calibration has been performed. As a result instead of doing calibration for each individual module we could treat whole detector as an one element. The method of relative calibration makes use of characteristic geometry of FWC and FTH detectors. Let us explain how it was done in case of FWC detector. We know that both layers in FWC are shifted by half an element with respect to each other what means that one module in FWC1 overlaps with two modules in FWC2. This feature is exploited to do alignment of the non-uniformity corrected light output within chosen layer. It is easy to understand that looking on Fig. 4.7, here the light output for element five in FWC2 is used to equalize the light yields of elements four and five in FWC1. Using these histograms we select few intervals (see grey bars in Fig. 4.7) on X-axis and project them onto Y-axis. The results of projections are fitted with gauss function and the peak position is determined. Based on that we can construct correlation between light outputs of two adjacent elements in the same layer as

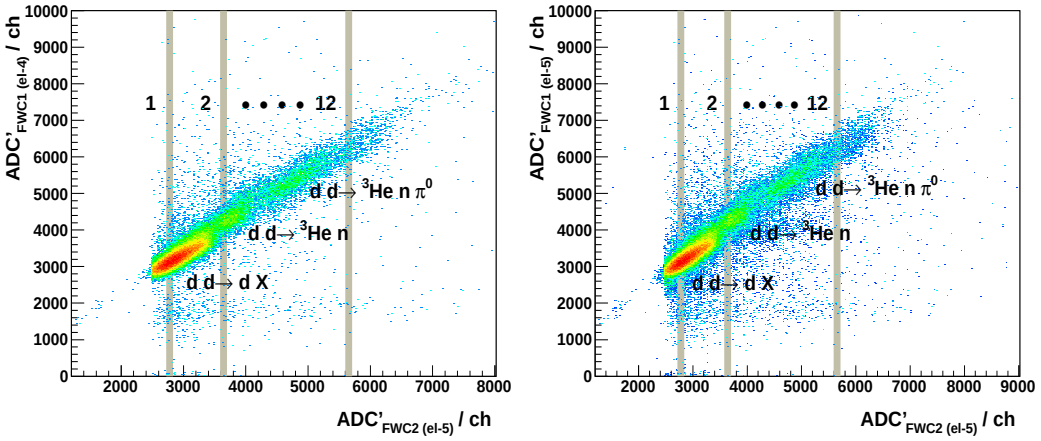

Figure 4.7: The correlation between the light outputs for ^{3}He (middle and upper band) and for deuterons stemming from break-up reactions (lower band). The $\mathrm{ADC}^{'} = \mathrm{ADC} \cdot \cos\theta / \mathrm{f}(\theta)$, where $\mathrm{f}(\theta)$ describes the corrections for non-uniformity. The grey bars denote the ranges on X-axis for which the projection onto Y-axis is performed.

it is shown in Fig. 4.8. By fitting polynomial of second order we are able to find correction factors which are used for alignment. With this method we can proceed iteratively for the rest of the modules in the FWC1 detector. The outcome of the procedure is illustrated in the right panel of Fig. 4.8. To perform relative calibration for FWC2 and FTH1 detectors an analogous technique has been applied.

The conversion of the signal amplitude to the energy deposit ΔE in a given detector was achieved by comparing the measured data to the Monte Carlo simulations. Based on assumption that the relative normalisation equalized possible non-linearities of different modules, we used for the comparison whole layers instead of doing the calibration element-wise. In order to ensure well defined energy loss special data sample containing

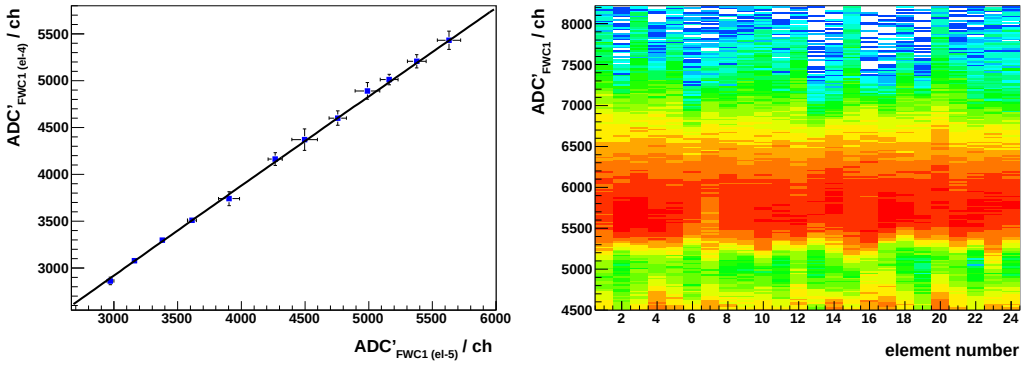

Figure 4.8: The polynomial of the second order used to equalize the light outputs of two neighboring elements in FWC1 detector (left). Relatively aligned light output in the FWC1 detector (right).

^{3}He from reaction dd $\rightarrow$ ^{3}He$n\pi^0$ and dd $\rightarrow$ ^{3}Hen was preselected. The light output of one layer (e.g FWC2) after correction for non-uniformity is plotted versus the light output of the first layer in FTH detector. This plot is then compared to the same correlations obtained from simulation. In left panel of Fig. 4.9 several distinctive points for which comparison was performed are marked by red circles. The calibration function which was used to align the Monte Carlo and the data is following:

$$\mathrm{dE} = \frac{\mathrm{a}\cdot\mathrm{ADC}'}{(1-(\mathrm{b}/\mathrm{a})\cdot\mathrm{ADC}')} \tag{4.16}$$

where parameters a and b can be expressed as:

$$\mathrm{a} = \frac{\mathrm{Y}_0}{\mathrm{c}\cdot\mathrm{X}_0} \tag{4.17}$$

$$\mathrm{b} = \frac{\mathrm{Y}_0}{\mathrm{c}\cdot\mathrm{X}_0^2}\cdot(1-1/\mathrm{c}) \tag{4.18}$$

The Y_0 and X_0 correspond to mean value of deposited energy of ^{3}He from Monte Carlo and the real data, respectively. The parameter c describes the deviation from linearity. This form of calibration function has the advantage over a polynomial, because the number of parameters is reduced, moreover, one knows which calibration constant should be modified in order to get a defined change in calibration. To control interactively the alignment of ΔE - ΔE bands special ROOT macro has been written. This tool makes possible to tune calibration constants c, Y_0 and X_0 by making slices from ΔE - ΔE plots and superimposing the Monte Carlo distributions on the experimental ones till they match. Since the non-uniformity parametrization has been carried out for six angular bins in the range from θ = 2.5° to θ = 18° also the constants for absolute energy calibration were extracted separately for each angular bin. To avoid discontinuity of calibrated energy between neighboring bins, the linear interpolation was applied. The right panel of Fig. 4.9 shows ΔE - ΔE band after applying absolute energy calibration.

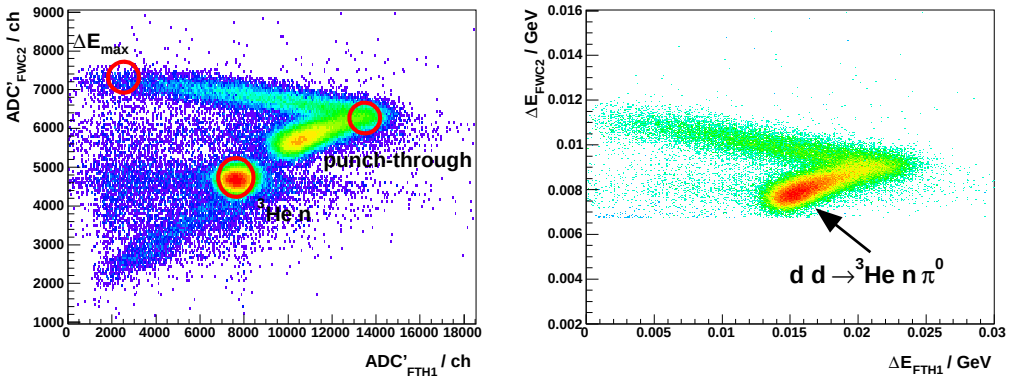

Figure 4.9: The non-uniformity corrected light outputs of ^{3}He in the second layer of FWC versus the first layer of FTH detector. Three distinctive points which were used for absolute calibration have been marked by the red circles (left). Non-uniformity and non-linearity corrected ΔE - ΔE plot. The presented energy loss band corresponds to the ^{3}He originating from dd $\rightarrow$ ^{3}He$n\pi^0$ (right).

4.2.2 Kinetic Energy Reconstruction in Forward Detector

In case of particles which are stopped in the detector, whole deposited energy is equal to the true kinetic energy. In reality, this behaviour does not hold due to the energy loss in the passive material of the detector and the inefficiencies in the scintillation process. To compensate for all these effects, the kinetic energy is reconstructed with the use of special lookup tables containing parameterized functions which allow recalculate E_{kin} from energy deposited in the detector. During preparation of individual tables one has to take into account the type of the particle, the detector plane where the particle was stopped, the scattering angle, and the number of layers used for energy reconstruction. All this informations have been derived from Monte Carlo simulations. In the first step single tracks for ^{3}He with kinetic energies varying between 0 GeV and 0.5 GeV were simulated. An analytical parametrization of energy loss as a function of kinetic energy has been obtained by fitting histograms showed in Fig. 4.10. Here, the correlation between deposited energy in specific detector layers versus the kinetic energy are presented. Since the energy loss depends on the scattering angles, the parametrization have been prepared separately for six angular bins. To keep the smoothness of reconstructed energy between neighboring bins, the linear interpolation was applied. The ^{3}He particles stemming from dd $\rightarrow$ ^{3}He$n\pi^0$ have kinetic energy in the range 125 MeV - 245 MeV therefore they are punching through the FWC and then are stopped mostly in the second and third layer of the FTH detector. This excludes the possibility of use the Forward Range Hodoscope which usually serves for energy reconstruction in most experiments carried out with the

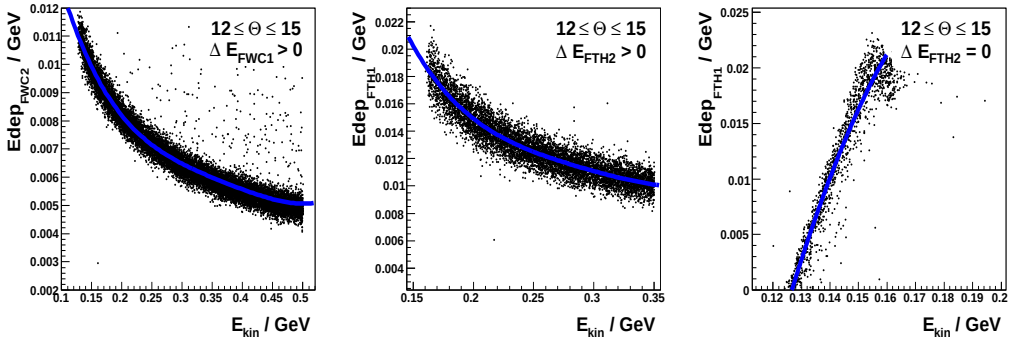

Figure 4.10: The parametrization of deposited energy as a function of initial kinetic energy performed for selected angular bin. The fitted functions are shown in blue. Different cuts on energy loss allow to distinguish between cases where ^{3}He particles are either stopped or they are punching through.

WASA detector. The studies of performance of FTH[2] detector described here [66] have shown that signals from most modules in the second and third layer were strongly position dependent, moreover, for some of the elements it was not possible to separate signals from the background though the voltage applied to the photomultiplier was at maximum. When one adds to this the complicated shape of modules (Archemedian spirals) than finally it turned out that is not possible to calibrate these two layers in plausible way. This limits the number of detectors which could be used for kinetic energy reconstruction to the FWC1, FWC2 and first layer of FTH1. For the latter, one has to separate the case where ^{3}He are stopped and when they are punching through. These situations can be disentangle by checking if helium reached or not the second layer of FTH. The blue lines in Fig. 4.10 show the fitted parametrizations, for the FWC polynomial of fourth order was used while for FTH power functions and polynomials of lower order have been applied. The values of the fit parameters together with the formulas which were used for fitting can be found in Appendix B. Having accomplished parametrization we defined χ^2 function in the following manner:

$$\chi^2 = \sum_{k=1}^{n} \frac{(\Delta E_k^m - \Delta E_k^t(E_{kin}))^2}{\sigma_k^2} \tag{4.19}$$

where n is the total number of layers traversed by the particle and σ_k denotes uncertainty of the energy deposit in layer *k*. The numerator in equation 4.19 is calculable as difference between measured energy deposit ΔE_k^m and expected energy loss $\Delta E_k^t(E_{kin})$ determined by an analytical parametrization. To find the kinetic energy in each event the minimization of χ^2 is performed. This is realized by a simple algorithm which executes quickly and returns those values of the parameter E_{kin} which give the lowest value of χ^2. The kinetic energy of ^{3}He is assumed to be properly reconstructed if the calculated χ^2 value is smaller then $\chi^2_{max} = 5$. If the χ^2_{max} is exceeded, then one can presume that ^{3}He was misidentified

[2]During this experiment the old FTH detector was used. Due to the radiation damage and aging effects of the scintillator material, it was replaced by the new one in 2008.

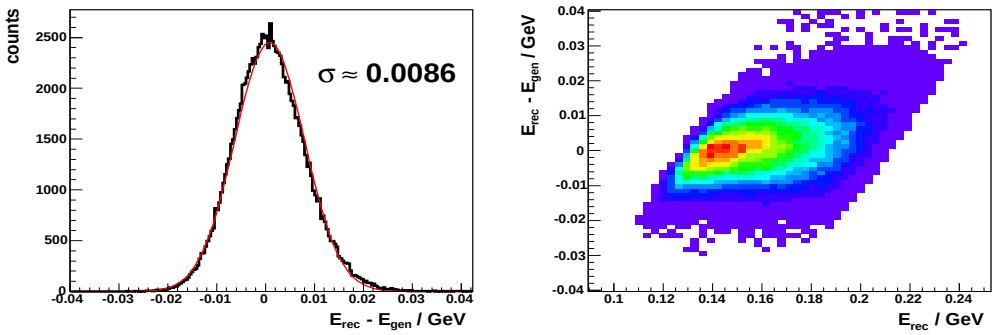

Figure 4.11: The difference between the reconstructed kinetic energy and the one obtained from the event generator. By fitting this distribution with gauss function the inaccuracy of the energy determination can be estimated (left). The evaluated from MC inaccuracy of the reconstructed energy versus ^{3}He kinetic energy (right).

and such an event is discarded. The evaluation of reconstruction error was obtained by comparing reconstructed kinetic energy from Monte Carlo data with the ”true” one, i.e. the kinetic energy given by the event generator (see Fig. 4.11).

4.2.3 Calibration of Scintillator Electromagnetic Calorimeter

In order to determine the energies of photons originating from neutral pion decay, the calibration of Scintillator Electromagnetic Calorimeter has to be performed. Prior to the installation of SEC at the COSY ring all crystals in the the calorimeter were tested and a pre-calibrated using radiative sources and cosmic muons [67]. This calibration is sufficient for online monitoring, although it can not be used for photons since the mechanism of energy deposition is different. Thus the further calibration was carried out with the use of photons from neutral pion decay. For that purpose events with exactly two neutral tracks in the Central Detector are selected. Two neutral tracks correspond to two neutral clusters (see Section 4.3.2) produced by photons which traverse the crystals in the calorimeter. The Lorentz invariant mass for each pair of photons can be calculated as:

$$M_{\gamma_1,\gamma_2} = \sqrt{2E_{\gamma_1}E_{\gamma_2}(1-\cos\theta_{1,2})} \tag{4.20}$$

where E_{γ_1} and E_{γ_2} are the measured energies of the photons based on the preliminary calibration and $\theta_{1,2}$ is the opening angle between the photons momenta. For each π^0 candidate, the invariant mass is assigned to the crystals with the largest energy deposit in the cluster. If the invariant mass distribution of two photons is shifted with respect to the π^0 mass then for each crystal of the calorimeter the calibration correction factor is applied according to:

$$E'_{\gamma_1,\gamma_2} = \frac{m_{\pi^0}}{M_{\gamma_1,\gamma_2}} E_{\gamma_1,\gamma_2} \tag{4.21}$$

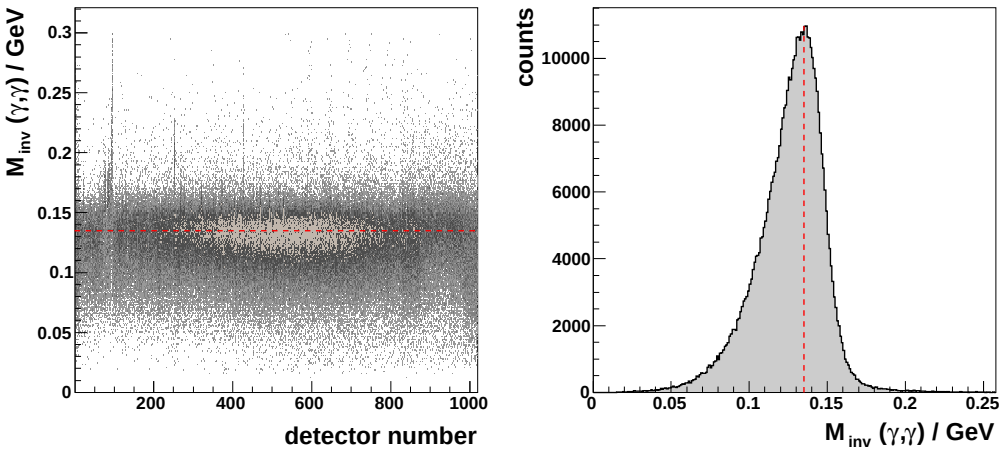

Figure 4.12: Two photon invariant mass distribution versus the detector number in the calorimeter (left). The mass of neutral pion is marked with red dashed line. In the right panel the invariant mass is shown. The peak corresponding to the π^0 mass is clearly seen.

where E'_{γ_1,γ_2} is the uncorrected energy of γ_1 and γ_2, E_{γ_1,γ_2} is the energy after applying corrections, m_{π^0} is mass of neutral pion and M_{γ_1,γ_2} is the invariant mass of two photons. This procedure is repeated until the invariant mass distributions of all modules in the SEC is centered at the exact mass of neutral pion. In the left panel of Fig. 4.12 the invariant mass distribution versus the module number in calorimeter is presented. The right panel of Fig. 4.12 shows the invariant mass of two photons stemming from dd $\rightarrow {}^3$Henπ^0 reaction.

4.3 Track Reconstruction

In case of the WASA detector we can distinguish two major parts where particles can be detected, namely the forward and the central part. Depending on which part of the WASA detector a particle traversed, two different algorithms for the tracks reconstruction are available in RootSorter framework. In general, both of these reconstruction procedures attempt to reproduce the particle trajectories with properly assigned four-momentum vectors. First, the algorithm has to determine which hits originate from the same particle. Those hits are merged into clusters which are the base components of tracks. In the following sections the description of the algorithms used for the reconstruction of ^{3}He and π^0 tracks will be given.

4.3.1 Track Reconstruction in the Forward Detector

As already mentioned in the previous section most helium originating from dd $\rightarrow {}^3$Henπ^0 reaction are stopped in the second layer of the FTH detector. This implies that in the track

reconstruction routine following detectors can be involved: two layers of FWC, straight layer of FTH and Forward Proportional Chamber. To minimize the frequency of occurrence of random hits the reconstruction algorithm works on pre-calibrated HitBanks. First, all hits from both layers of FWC detector are put into two temporary arrays. The index of an element in such an array corresponds to the number of hit module in the detector. This unique pattern allows to select only hits which come from overlapping elements. If there is more then one such a combination additional constraints are applied e.g. the smallest time difference between hits or the energy deposit thresholds. The overlap between elements in FWC defines the information about the azimuthal angle for the track candidate. Based on that, the track is extrapolated to the next detector which is the FPC. Here, hit straws from four independent modules are combined into clusters. To form the cluster the geometrical overlap between the hit sensing wires is checked. If we assumed an ideal case when a cluster would contain only hits stemming from the impact of one particle then due to the orientation of straws (see section 3.3.1.2) we can expect in total four overlapping clusters in the FPC detector. In reality, this number can be increased due to electronic noise or artifacts in the reconstruction. The exclusion of additional clusters is realized by comparing the azimuthal overlap. Algorithm starts with cluster in first plane and tries to match it with another one from an adjacent layer. If succeeded then the search of third best matching cluster from any unused layer is performed. After all possible combinations have been checked, overlapping clusters are merged into so-called detector track. To determine the coordinates of clusters the position of the sensing wires is used. The crossing point of all wires defines the coordinates of the track, assuming its origin in the origin of the WASA coordinate system. In Fig. 4.13 the residuals and efficiency for modules used in track finding procedure are presented. The residuals are defined as a difference between measured and calculated position of cluster in given module. Let us denote four possible clusters which can form track in FPC by X, Y, U, V (each cluster represents one module). If, for instance we want to estimate residual for cluster X then we have to check what was the measured position and compare it to the expected position calculated from clusters Y, U, V. In an analogous manner we can determine the residuals for remaining modules. The residuals centered at zero mean that geometry of FPC used in the track reconstruction is compatible with the one measured experimentally. To determine the efficiency of given module we have to prepare sample of FPC tracks without requesting this particular detector plane. In this work the efficiency of reconstructing FPC clusters have been studied on ^{3}He sample stemming from dd $\rightarrow$ ^{3}Hen reaction. The ratio of the number of reconstructed tracks with a cluster in the investigated detector plane to the total number of reconstructed tracks defines the detection efficiency. In the right column of Fig. 4.13 efficiency for individual modules as a function of cluster position in particular module is plotted. As can be seen, efficiency for all planes is close to 100%. The dip around zero corresponds to the holes in each module which are necessary to provide the room for beam pipe. Subsequently, the track segments from the FWC and FPC are checked for an azimuthal overlap. If the condition is fulfilled then they are assigned to the same track. In the last step the track finding procedure searches for the hits in the straight layer of FTH and again if there is an azimuthal overlap with already formed FWC-FPC track, those

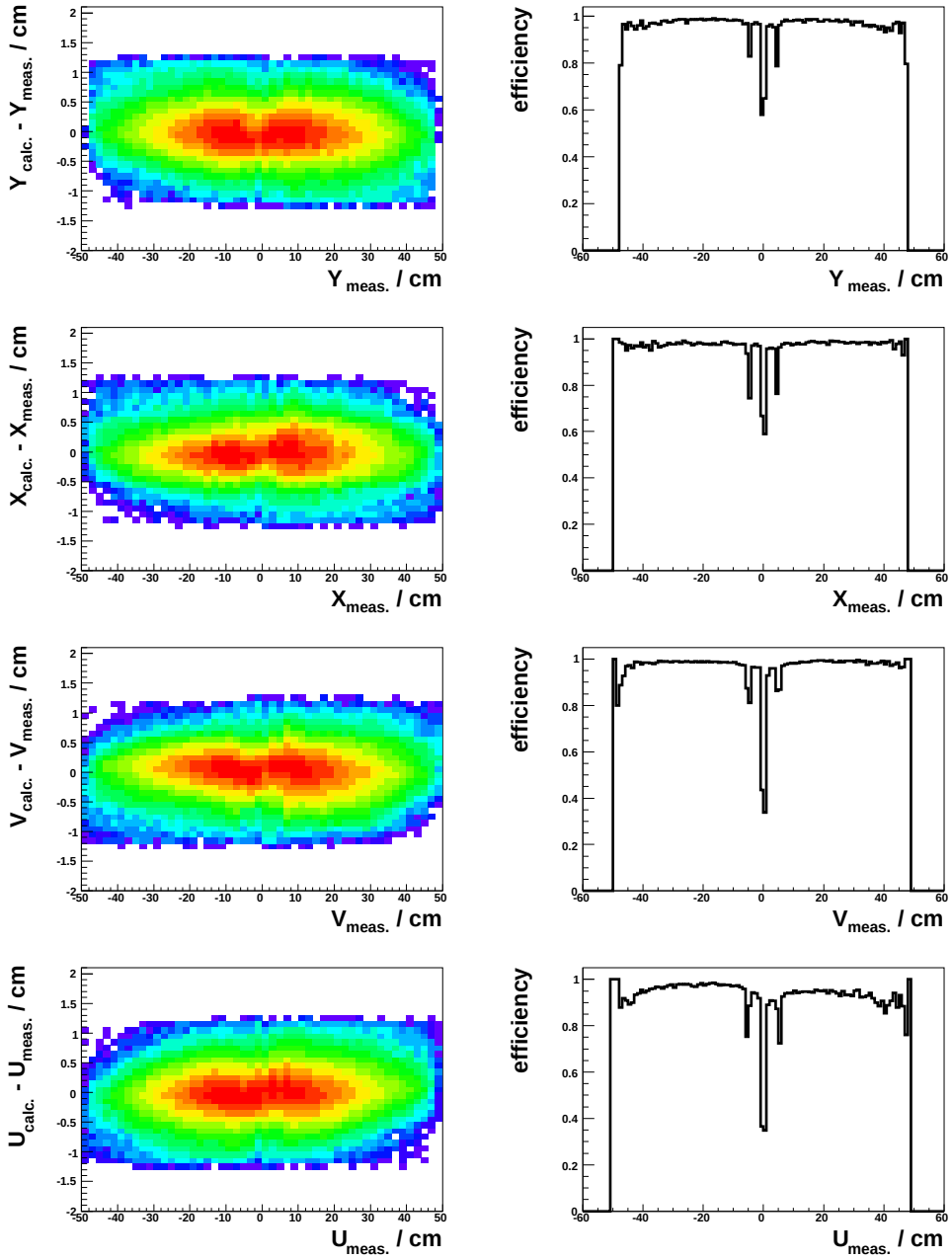

Figure 4.13: The distribution of residuals as a function of measured cluster position for individual modules in FPC detector (left column). Efficiency for four modules used in the track reconstruction procedure for ^{3}He originating from dd $\rightarrow$ ^{3}Hen reaction.

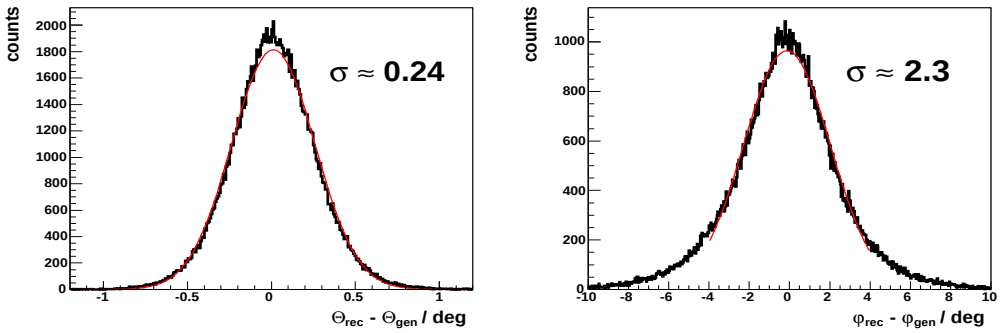

Figure 4.14: The resolution of polar (left) and azimuthal (right) angles. The angles reconstructed by means of FPC have been compared to the initial ones given by generator.

hits are merged into this track. The sizes of the overlaps, time differences and a minimum amount of deposited energy for clusters contributing to the track are defined as set of external parameters. The presented scheme of track reconstruction allows to connect a group of modules from different detectors which were hit by one particle. At this stage also the spatial information of the track is known. What is missing to get four-vector for given particle is the energy. It can be calculated using the procedure described in section 3.2.2. The algorithm for kinetic energy reconstruction operates on the energy deposits from the modules of the detectors which are assigned to the track. In each track the time information is available which is defined by the time of the hit stemming from FTH1 detector being the part of the track. In Fig. 4.14 the averaged angular resolution for reconstructed ^{3}He track is demonstrated.

4.3.2 Track Reconstruction in the Central Detector

The track reconstruction in the central detector makes use of an information provided by three different types of detectors, namely Mini Drift Chamber, Plastic Scintillator Barrel and Electromagnetic Calorimeter. For each of them separate routines for cluster reconstruction have been implemented. The role of track reconstruction procedure is to assign those clusters which belong to the same particle. The track finding algorithm is capable to reproduce charged as well as neutral tracks. In this work it was employed for the neutral tracks only, since we were interested in the measurement of the neutral pion. To reconstruct the neutral tracks, it was sufficient to possess the information about the clusters from PSB and SEC. The MDC detector was not of importance here, it plays crucial role for the charged particles but for the neutral can be omitted in the track finding routine. Here, a neutral track is defined by the presence of a cluster in the SEC with no matching cluster in PSB detector. When photons traverse the crystals in the calorimeter they produce an electromagnetic shower which develops over a group of adjacent crystals. The size of the shower depends on the energy of the photons. Modules involved in an electromagnetic shower form a cluster. It is a task of the cluster finding routine to identify and

merge all crystals belonging to one electromagnetic shower originating from one primary particle. The algorithm used for that purpose is an iterative procedure which operates on the two-dimensional space. In first step routine searches for the crystal which contains hit with the highest energy deposit. This element becomes the center of the new cluster. Adjacent neighbors are scanned and joined to the cluster. The required criterion is that each hit included into cluster should have energy deposit of at least 2 MeV. Moreover, an appropriate hits should not be separated in time from reference hit by more than 50 ns. Algorithm pursues search for new crystal with highest energy deposit, which is not included in the previous cluster and the procedure to find neighboring elements is repeated. This process is iterated until all hits in neighboring crystals have been used. Furthermore, the routine rejects clusters with a total energy below 10 MeV. This condition reduce so-called split-off contributions which occur due to the interactions of hadrons and leptons with the active materials in the calorimeter. These interactions can fake electromagnetic showers which might be considered as true neutral candidates by the reconstruction algorithm. The total energy deposit of a cluster is evaluated by summing up the individual energy deposits from crystals which have been assigned to the cluster. The time information of the cluster is defined by the time extracted from the element with the highest deposited energy. The position $\vec{X}$ of the cluster is calculated as the weighted sum of positions $\vec{x_i}$ of individual modules that form the cluster:

$$\vec{X} = \frac{\sum_i w_i \vec{x_i}}{\sum_i w_i}, \tag{4.22}$$

where the weights w_i are associated with the energy deposited E_i in the single crystals:

$$w_i = \mathrm{MAX}\{0, W_0 + \ln\frac{E_i}{\sum_i E_i}\}. \tag{4.23}$$

The value of the constant W_0 has been found to be equal to 4 [68]. To distinguish neutral clusters from the charged ones in the calorimeter the information from the Plastic Scintillator Barrel is mandatory. The neutral cluster in SEC is defined by the absence of a corresponding cluster in PSB which can be formed only when charged particles traverse the detector. A cluster in the Plastic Scintillator Barrel can be formed by a single hit or two hits. The latter case occurs when particle impinging the overlap region of two adjacent elements in the detector. The hits from neighboring modules are merged into cluster if they are separated in time by less than 10 ns and each of them has a minimum deposited energy of 0.5 MeV. The time information of the cluster is calculated as the mean value of the time associated to the contributing hits. The deposited energy assigned to a cluster is extracted from the hit with the highest energy deposit. The assignment of clusters from SEC and PSB described in the following section allows to classify particles measured in the central detector as the neutral one.

4.4 Particle Identification

The identification of particles in the Forward Detector has been done by means of the specific energy loss which is described by Bethe-Bloch formula [69]. The used $\Delta E - \Delta E$

technique relies on the comparison of the deposited energy in different layers of the FD detector. When plotting $\Delta E - \Delta E$, a distinct correlation for different particles types can be observed. In the left panel of Fig. 4.15 the energy loss in one layer of FWC detector versus the energy loss in the first layer of FTH detector is presented. The scatter plot is dominated

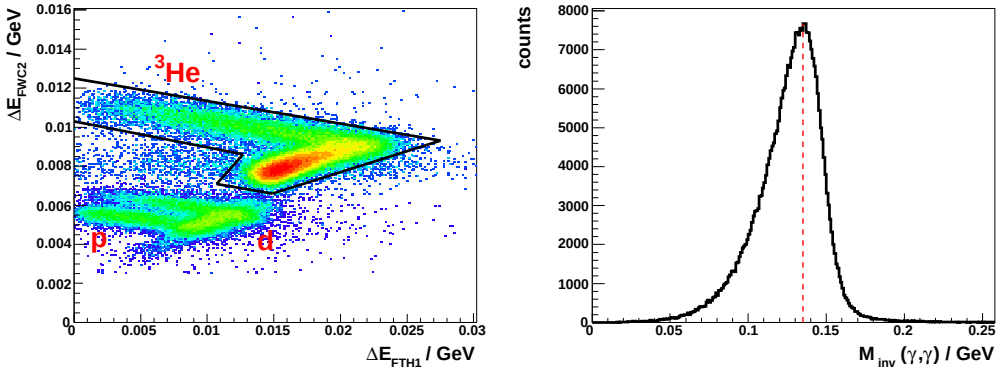

Figure 4.15: The energy loss in the Forward Window Counter versus energy loss in the first layer of the Forward Trigger Hodoscope. The obtained energy patterns allow to distinguish between different particles types. The graphical cut indicated by black line represents the region used to select ^{3}He candidates (left). Two photon invariant mass distribution, the peak corresponding to the π^0 mass is clearly visible (right).

by ^{3}He stemming from dd $\rightarrow$ ^{3}He$n\pi^0$. As expected, the energy resolution is good enough to clearly distinguish between bands formed by different particles types. The descending band inside the graphical cut indicates ^{3}He particles stopped in the straight layer of FTH while the lower ascending band corresponds to helium punching through the detector. Below the marked region the energy loss patterns for deuterons and protons originating mainly from breakup reactions are visible. Due to the threshold (see Section 6.1) in FWC only the branch where stopped protons are grouped survived, the rest with lower energy losses was cut out by the trigger.

After identification of ^{3}He in the forward detector two neutral tracks in the central detector are requested and the corresponding invariant mass is constructed. This combination provides a very efficient way for the selection of the dd $\rightarrow$ ^{3}He$n\pi^0$ channel. In the right panel of Fig. 4.15 the two photon invariant mass distribution is demonstrated. More details about the coincidence technique used for particle selection will be given in section where the experimental trigger is described.

5 Phenomenological Models

At present there is no microscopic theoretical model for description of dd $\rightarrow {}^3\mathrm{He}n\pi^0$ reaction. However, some model describing the data at least qualitatively is necessary for the acceptance corrections. Therefore simple model based on physical assumptions was constructed. It will be used not only for acceptance corrections but it deliver also some physical information about the reaction process. Therefore the comparison of such model with experimental data deliver already some constraints on the microscopic calculations that will be performed in the future.

In this section first the independent variables necessary for the presentation of three-body reaction data are briefly discussed and the expressions for some differential cross sections are given. Than the components of quasi-free reaction process are presented. Finally the partial-wave decomposition for three-body reaction is introduced. All these together are the ingredients of the phenomenological model used in the analysis of present data.

5.1 Choice of Independent Variables

Generally for a reaction of two particles leading to *n* particles in the final state there are 3n degrees of freedom corresponding to variables necessary to completely describe the final state. The four momentum conservation reduces this number to $3n-4$. Additionally, if the particles in the initial state are not polarised, the initial state have axial symmetry. Therefore there is one trivial variable corresponding to rotation around the beam axis direction. Than finally for the complete description of a three-body reaction $3n-5$ non-trivial independent variables are necessary. Therefore for the investigated reaction dd $\rightarrow {}^3\mathrm{He}n\pi^0$ with unpolarised particles in the initial state and three particles in the final state there are four independent variables fully describing the reaction kinematics.

The natural coordinate system used commonly for the description of the three-body reactions is given by the Jacobi-coordinates. The momenta $\vec{\mathrm{P}}$, $\vec{\mathrm{p}}$ and $\vec{\mathrm{q}}$ in this system are defined by

$$\begin{aligned}
\vec{P} &= \vec{p}_1 + \vec{p}_2 + \vec{p}_3 \\
\vec{p} &= \frac{1}{E_2+E_3}\left(E_3\vec{p}_2 - E_2\vec{p}_3\right) \\
\vec{q} &= \frac{1}{E_1+E_2+E_3}\left[\left(E_2+E_3\right)\vec{p}_1 - E_1\left(\vec{p}_2+\vec{p}_3\right)\right]
\end{aligned} \tag{5.1}$$

where the outgoing particles momenta are denoted by $\vec{p}_1$, $\vec{p}_2$, $\vec{p}_3$ and the total energies of particles are E_1, E_2, E_3. Using the cyclic permutation of indices it is possible to obtain other two equivalent sets of Jacobi momenta. For the description of the reaction it is most convenient to use the center-of-mass reference frame. Then the Jacobi momenta have simple interpretation visible in Fig. 5.1. In the following this coordinate system will be used with the z-axis along the beam momentum direction. Since the description is in center-of-mass system than $\vec{P} = 0$ and one obtain the condition $\vec{p}_2 + \vec{p}_3 = -\vec{p}_1$. Solving Eq. 5.1 with this condition and applying Lorentz transformation to the subsystem of particles 2-3 one obtains expressions for momenta $\vec{p}$ and $\vec{q}$

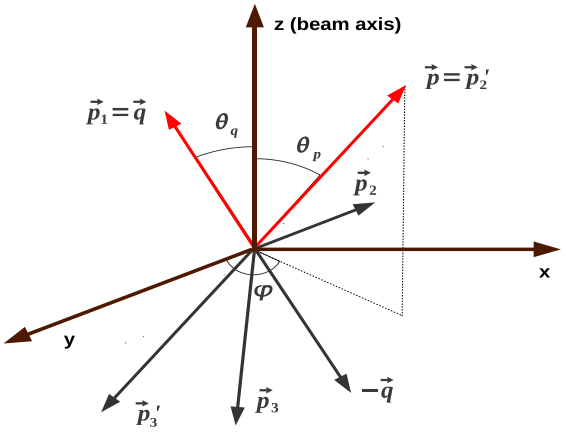

Figure 5.1: Jacobi momenta and angles definitions for a three-body reaction.

$$\begin{aligned}
\vec{p} &= \frac{1}{E_2+E_3}\left(E_3\vec{p}_2 - E_2\vec{p}_3\right) = \vec{p}'_2\,, \\
\vec{p} &= -\frac{1}{E_2+E_3}\left(E_3\vec{p}_2 - E_2\vec{p}_3\right) = -\vec{p}'_3\,, \\
\vec{q} &= \vec{p}_1\,.
\end{aligned} \tag{5.2}$$

Therefore the interpretation of Jacobi momenta is following: $\vec{q}$ is the momentum of a particle 1 in the global center-of-mass system, $\vec{p}$ is the momentum $\vec{p'}_2$ of particle 2 in center-of-mass of the subsystem 2-3.

The momentum vectors $\vec{p}$ and $\vec{q}$ fully describe the kinematics of the three-body reaction. However for three-body reaction there are only four independent variables necessary for the full description. In the following they will be chosen as: M_{23} - invariant mass of the 2-3 subsystem, $\cos\theta_q$ - cosine of the angle between the momentum vector $\vec{q}$ and beam momentum (z-axis) in global center-of-mass system, $\cos\theta_p$ - cosine of the angle between momentum vector $\vec{p}$ and beam momentum (z-axis) in the global center-of-mass system and φ - relative angle between planes defined by $\vec{q}$ and beam momentum and by $\vec{p}$ and beam momentum.

5.2 Cross Section

The total cross section is a normalised integral of the transition probability over the whole available phase space. According to [70] the total cross section for 3-body reaction may by expressed by

$$\sigma = \frac{1}{2\sqrt{\lambda(s, M_a^2, M_b^2)}(2\pi)^5} \int \prod_{i=1}^{3} \frac{d^3 p_i}{2E_i} \delta^4 \left(P_a + P_b - \sum_{j=1}^{3} P_j \right) |T|^2 , \tag{5.3}$$

where *s* is the square of invariant mass in the entrance channel, M_a, M_b are the masses of beam and target particles, P_a, P_b and P_j denote four-momenta of the beam, target and outgoing particles, p_i are components of momentum vectors of outgoing particles. The transition matrix T is a function of four independent variables which are expressed by the momenta of all particles involved in the reaction. The λ function is defined as

$$\lambda(x, y, z) = x^2 + y^2 + z^2 - 2xy - 2yz - 2zx . \tag{5.4}$$

Using the λ function, the entrance channel center-of-mass momentum may be expressed as

$$P_a^* = P_b^* = \frac{\sqrt{\lambda(s, M_a^2, M_b^2)}}{2\sqrt{s}} . \tag{5.5}$$

Similarly the absolute value of the Jacobi momenta may be calculated

$$q = \frac{\sqrt{\lambda(s, M_1^2, M_{23}^2)}}{2\sqrt{s}} , \qquad p = \frac{\sqrt{\lambda(M_{23}^2, M_2^2, M_3^2)}}{2M_{23}} , \tag{5.6}$$

where M_1, M_2 and M_3 are the masses of the outgoing particles.

In the expression 5.3 certain integrations may be performed up to the moment when only four independent variables remain. For these integrations it is sufficient to calculate phase space only since $|T|^2$ is a function of four independent variables only. The three-body phase space R_3 my be calculated from the formula [70]

$$R_3 = \int ds_{23} R_2(s, M_1^2, s_{23}) R_2(s_{23}, M_2^2, M_3^2)\,, \tag{5.7}$$

where $s_{23} = M_{23}^2$. As the 2-body phase space R_2 one may use the formulae [70]

$$\begin{aligned} R_2(s, M_1^2, s_{23}) &= \tfrac{q}{4\sqrt{s}} \int d\Omega_q = \tfrac{q}{4\sqrt{s}} \int d\cos\theta_q d\varphi_q\,, \\ R_2(s_{23}, M_2^2, M_3^2) &= \tfrac{p}{4\sqrt{s_{23}}} \int d\Omega_p = \tfrac{p}{4\sqrt{s_{23}}} \int d\cos\theta_p d\varphi_p\,, \end{aligned} \tag{5.8}$$

where $d\Omega_p$ and $d\Omega_q$ are the solid angles, θ_p and θ_q are polar angles, φ_p and φ_q are azimuthal angles of momentum vectors $\vec{p}$ and $\vec{q}$ in global center-of-mass system. Inserting equation 5.8 to expression 5.7 one obtains

$$R_3 = \frac{1}{16\sqrt{s}} \int pq \frac{ds_{23}}{\sqrt{s_{23}}} d\cos\theta_q d\varphi_q d\cos\theta_p d\varphi_p\,. \tag{5.9}$$

For the unpolarised beam and target one may integrate over one of the polar angles living only the relative polar angle $\varphi = \varphi_p - \varphi_q$. One may use invariant mass $M_{23} = \sqrt{s_{23}}$ of the subsystem 2-3 instead of using s_{23}. Using these substitution equation 5.9 may be rewritten in the form

$$R_3 = \frac{2\pi}{8\sqrt{s}} \int pq dM_{23} d\cos\theta_q d\cos\theta_p d\varphi\,. \tag{5.10}$$

The choice with equations 5.8 and further steps define the independent variables that may be used for description of three-body reaction and they are M_{23}, $\cos\theta_q$, $\cos\theta_p$ and φ. Up to now the integrations were performed over dependent variables therefore the result given by equation 5.10 for the phase space is valid also for the cross section. Inserting equation 5.10 into equation 5.3 and using equation 5.5 the four-fold differential cross section may be expressed in the form

$$\frac{d^4\sigma}{2\pi dM_{23} d\cos\theta_q d\cos\theta_p d\varphi} = \frac{1}{32(2\pi)^5 s P_a^*} pq|T|^2\,. \tag{5.11}$$

The integration over some of independent variables leads to the expressions for single differential cross sections as e.g. $d\sigma/dM_{23}$, $d\sigma/2\pi d\cos\theta_q$, $d\sigma/2\pi d\cos\theta_p$, $d\sigma/d\varphi$.

5.3 Quasi-Free Reaction Model

A neutron and a proton are loosely bound in a deuteron. Therefore in high momentum transfer reactions in which deuteron is involved, the reaction can proceed via interaction with a single nucleon of the deuteron, while the second nucleon is a spectator. The importance of such reaction mechanism is limited only to some regions of the phase space, in which the spectator nucleon have the same momentum as in the deuteron. This remains the main characteristic of the quasi-free reaction mechanism and is used to check the validity of this model. Experimentally the quasi-free approximation was checked comparing data for proton-proton induced reactions with reactions induced by proton-deuteron initial state with a neutron spectator. The comparison was performed for pion production reactions [71, 72] and for η production [73, 74]. Very good agreement of the total cross sections measured with these two methods demonstrated validity of the quasi-free approximation. In present analysis the quasi-free reaction model was used as a part of the theoretical approach. The two-body reaction pd $\rightarrow {}^3\mathrm{He}\pi^0$ was considered as the quasi-free part of the three-body dd $\rightarrow {}^3\mathrm{He}n\pi^0$ reaction. Since in investigated reaction two deuteron's are involved the reaction may proceed with projectile or target neutron spectator. The quasi-free reaction have been shown schematically in Fig. 4.3 in Section 4.1.2. It is seen that full description of the quasi-free contribution to dd $\rightarrow {}^3\mathrm{He}n\pi^0$ reaction can be obtained using the cross section for pd $\rightarrow {}^3\mathrm{He}\pi^0$ in the proper energy range convoluted with the momentum distribution of the proton in the deuteron. The calculations of the cross section for pd $\rightarrow {}^3\mathrm{He}\pi^0$ reaction are rather difficult. Therefore, instead of the theoretical calculations the existing data parametrisation was used. The available data for the differential cross section for pd $\rightarrow {}^3\mathrm{He}\pi^0$ reaction cover the energy range from the threshold up to 10 MeV above threshold [75]. There are also measurements at higher energies corresponding to excess energy above threshold of 40, 60 and 80 MeV [76]. Use of the parametrised experimental cross section for pd $\rightarrow {}^3\mathrm{He}\pi^0$ reaction have additional advantage. It may be expected that in such treatment the quasi-free contribution will be absolutely normalised. The momentum distribution of the nucleons in the deuteron can be obtained using deuteron wave-function. In the present analysis an analytically parametrised deuteron wave function based on the Paris potential [60] was used. In the data that we have collected not whole distribution of the proton momentum in deuteron is accessible. The deuteron beam momentum for dp $\rightarrow {}^3\mathrm{He}\pi^0$ reaction (with target proton at rest) corresponding to the reaction threshold is 1.284 MeV/c. In the present experiment the deuteron beam momentum was 1.2 MeV/c. Therefore in present data the dp $\rightarrow {}^3\mathrm{He}\pi^0$ reaction will occur as quasi-free process only involving protons which sufficiently large momenta in the deuteron target. In order to reach the threshold for dp $\rightarrow {}^3\mathrm{He}\pi^0$ reaction the proton in the deuteron target must have the momentum of at least 35 MeV/c.

5.4 Partial Wave Expansion for a Three-Body Reaction

Partial wave expansion is a commonly used method for the analysis of nuclear and elementary particle reactions [77, 78]. This method is very useful since due to short range of strong interaction only limited number of partial waves (and accordingly limited number of expansion coefficients) is sufficient for description of the reaction. Each partial wave corresponds to the angular momentum within the system. If the energy available for the reaction is small than only small angular momenta are allowed. In a special case of a reaction with the energy close to reaction threshold it is usually sufficient to consider only processes with *s*-wave (angular momentum equal 0) and *p*-wave (angular momentum equal 1).

In the textbooks as e.g. [77] usually the formulae for two-body reaction are given. Here the general formulae for the three-body case are presented, which are more complicated since more couplings of spins and angular momenta are required. In following these couplings are directly related to the choice of independent variables used in the description of the three-body reaction as discussed in section 5.1.

Denote spin of the incident particles by $\vec{s}_a$, $\vec{s}_b$ and for outgoing particles by $\vec{s}_1$, $\vec{s}_2$ and $\vec{s}_3$. The orbital angular momenta are $\vec{L}_i$ - entrance channel, $\vec{L}_1$ - particle 1 in global center-of-mass system, $\vec{L}_{23}$ - particle 2 in subsystem 2-3. The total angular momenta are $\vec{J}$ - entrance and exit channel (they are equal due to angular momentum conservation), $\vec{j}_1$ - particle 1 in global center-of mass system, $\vec{j}_{23}$ - particle 2 in subsystem 2-3. As the quantisation axis (z-axis) it is most convenient to use the beam direction.

For the entrance channel one may define total spin $\vec{s}_i = \vec{s}_a + \vec{s}_b$, than the total angular momentum is $\vec{J} = \vec{s}_i + \vec{L}_i$. When adding spins and/or angular momenta one has to use Clebsch-Gordan coefficients which contain the projections onto z-axis (m_a, m_b, m_{L_i}, m_J for spins, orbital angular momentum and total angular momentum correspondingly).

For exit channel one may define spin for subsystem 2-3 $\vec{s}_{23} = \vec{s}_2 + \vec{s}_3$ and total angular momentum for subsystem 2-3 $\vec{j}_{23} = \vec{s}_{23} + \vec{L}_{23}$. Similarly one may define total angular momentum for particle 1 $\vec{j}_1 = \vec{s}_1 + \vec{L}_1$. These total angular momenta are coupled to entrance total angular momentum $\vec{J} = \vec{j}_1 + \vec{j}_{23}$. For each sum of spins and/or angular momenta one has to use their projections onto z-axis (denoted by m_1, m_2, m_3 for spins, m_{L_1}, $m_{L_{23}}$ for orbital angular momenta and m_{j_1}, $m_{j_{23}}$ for total angular momenta) and corresponding Clebsch-Gordan coefficients.

The coupling may be performed in a different order, first adding all spins to the total exit channel spin, then adding all orbital angular momenta to total angular momentum in the exit channel, and then adding total spin and total orbital angular momentum to total angular momentum J. Such coupling is equivalent to the coupling described above. One obtain the same number of amplitudes, however, they are labeled by different set of the quantum numbers. There is a unique relation between the amplitudes obtained with these two couplings.

With such decomposition one obtains amplitudes a_α which are labeled by quantum numbers denoted by $\alpha = (s_i, L_i, s_{23}, j_{23}, L_{23}, L_1, j_1, J)$. Using these amplitudes one my obtain total transition amplitude which is labeled by projections of all spins involved. This transition amplitude is obtained as a sum over all possible α of the product of corresponding Clebsch-Gordan coefficients, amplitudes a_α and spherical harmonics for L_{23} and L_1. The spherical harmonics $Y_{L_{23}}^{m_{L_{23}}}(\hat{p})$ and $Y_{L_1}^{m_{L_1}}(\hat{q})$ as the argument have the direction of versors $\hat{p}$ and $\hat{q}$ with respect to the z-axis.

Additionally the parity conservation constraints should be inserted into the formula. Internal parity of the particles participating in the reaction is denoted by Π_a, Π_b, Π_1, Π_2, Π_3. Then the entrance channel parity is $\Pi_i = (-1)^{L_i}\Pi_a\Pi_b$ and the exit channel parity is $\Pi_f = (-1)^{L_1+L_{23}}\Pi_1\Pi_2\Pi_3$. Parity conservation requires that $\Pi_i = \Pi_f$ therefore one should include in the formula for amplitude the Kronecker delta function δ_{Π_i,Π_f}.

For identical particles in the entrance channel additional constraints on the $L_i + s_i$ should be included. For identical bosons the symmetry of the entrance channel wave function requires that $L_i + s_i$ should be even, while for fermions the antisymmetry of the wave function requires that $L_i + s_i$ should be odd. Therefore for identical bosons the identity function is $\delta_{\text{identity}} = \delta_{L_i+s_i \pmod 2,0}$ and for identical fermions it is $\delta_{\text{identity}} = \delta_{L_i+s_i \pmod 2,1}$.

Finally the transition amplitude labelled with all spin projections may be written in the form

$$\begin{aligned} T_{m_1,m_2,m_3}^{m_a,m_b} = \sum_{\substack{s_i,L_i,s_{23},j_{23},\\ L_{23},L_1,j_1,J}} & \langle s_a, m_a, s_b, m_b | s_i, m_a + m_b \rangle \langle L_i, 0, s_i, m_a + m_b | J, m_a + m_b \rangle \\ & \langle s_2, m_2, s_3, m_3 | s_{23}, m_2 + m_3 \rangle \langle s_1, m_1, L_1, m_{L_1} | j_1, m_{j_1} \rangle \\ & \langle s_{23}, m_2 + m_3, L_{23}, m_{L_{23}} | j_{23}, m_{j_{23}} \rangle \langle j_1, m_{j_1}, j_{23}, m_{j_{23}} | J, m_a + m_b \rangle \\ & \delta_{\Pi_i,\Pi_f}\delta_{\text{identity}} a_{s_i,L_i,s_{23},j_{23},L_{23},L_1,j_1,J} \sqrt{2L_i+1} Y_{L_{23}}^{m_{L_{23}}}(\hat{p}) Y_{L_1}^{m_{L_1}}(\hat{q}) \end{aligned} \tag{5.12}$$

with following substitution $m_{j_1} = m_1 + m_{L_1}$, $m_{L_{23}} = m_a + m_b - m_{L_1} - m_1 - m_2 - m_3$, $m_{j_{23}} = m_a + m_b - m_{L_1} - m_1$.

The transition probability is obtained by averaging over spin projections in the entrance channel and sum over all spin projections in the exit channel of the squared transition amplitude

$$|T|^2 = \frac{1}{(2s_a+1)(2s_b+1)} \sum_{\substack{m_a,m_b,\\ m_1,m_2,m_3}} |T_{m_1,m_2,m_3}^{m_a,m_b}|^2 . \tag{5.13}$$

5.4.1 Momentum Dependence of Partial Amplitudes

The transition probability $|T|^2$ in equation 5.13 is a function of four independent variables: M_{23}, θ_p, θ_q and φ. The dependence on the angles is explicitly contained in the spherical harmonics in equation 5.12. There the amplitudes a_α may depend only on M_{23} or equivalently on momenta p and q. This dependence cannot be found without microscopic calculations, however, one can make some predictions under simple assumptions.

Generally when deriving the transition amplitude f the integral of some transition operator V multiplied by the initial Ψ_i and final Ψ_f state asymptotic wave functions have to be calculated. The wave function Ψ_i depend on the initial momentum and the wave function Ψ_f for the three-body depend on momenta p and q.

$$f \propto \langle \Psi_f(p,q)|V|\Psi_i(P_a^*)\rangle \,. \tag{5.14}$$

If there are no long range interactions (as e.g. Coulomb interaction) the wave functions can be approximated by the plane waves. The plane wave for momentum Q can be expanded in terms of partial waves and asymptotically can be expressed by the Bessel function $j_L(QR)$, where R is a range of interaction and L is an angular momentum [78]. Expanding the Bessel function into powers of QR leads to the first term proportional to Q^L. Therefore in good approximation each plane wave Ψ_{PW} can be approximated by

$$\Psi_{PW}(Q) \propto Q^L \,. \tag{5.15}$$

In the investigated $dd \to {}^3He n\pi^0$ reaction all outgoing particles are neutral. Therefore it is well justified to replace the final state wave function by product of two plane wave functions, which can be expressed by the first term of the expansion of the Bessel function. Finally it may be expected that the momentum dependence of the transition amplitude for the three-body reaction can be well approximated by

$$f \propto p^{L_{23}} q^{L_1} \,. \tag{5.16}$$

Therefore additional momentum dependence of amplitudes a_α in equation 5.12 was taken in the form $p^{L_{23}} q^{L_1}$. This leads to the explicit momentum dependence of the cross section of the form $p^{2L_{23}} q^{2L_1}$.

It should be pointed out that this approach neglect other possible momentum dependencies of the transition amplitude. They may appear e.g. due to final state interaction or due to the presence of the resonances in any subsystem of two final particles. The pions have usually small final state interaction with nucleons, therefore it may be neglected for ${}^3He - \pi^0$ and $n - \pi^0$. The final state interaction ${}^3He - n$ can be strong. However, for $dd \to {}^3He n\pi^0$ reaction the isospin symmetry requires the ${}^3He - n$ system to be in the state with the total isospin equal to one. The first ${}^4He$ excited levels with isospin one which may be responsible for final state interaction are at about 20 MeV and are quite broad [79]. Therefore no strong final state ${}^3He - n$ interaction is expected.

assignment number	particle 1	particle 2	particle 3	subsystem 2 – 3
1	^{3}He	n	π^0	n – π^0
2	n	π^0	^{3}He	π^0 – ^{3}He
3	π^0	^{3}He	n	^{3}He – n

Table 5.1: Possible independent assignments of the particles for dd $\rightarrow$ ^{3}Henπ^0 reaction. The permutation of the particles in subsystem 2-3 leads to the same description of the reaction.

5.4.2 Cross Section for dd $\rightarrow$ ^{3}Henπ^0 Reaction

Using MATHEMATICA [80] the partial wave expansion for dd $\rightarrow$ ^{3}Henπ^0 reaction was performed limiting to the *s*- and *p*-wave in the exit channel. In the choice of independent variables described in section 5.1 as well in the partial wave expansion there is a freedom to assign particle denoted by 1 and two remaining particles forming subsystem 2-3. In the present case the three independent assignments shown in Tab. 5.1 are possible. For each assignment it is possible to perform the partial wave expansion. It results in the partial wave amplitudes a_α which are labelled by quantum numbers specific for a chosen assignment and therefore they have different interpretation. However, it is always possible to express amplitudes a_α for a given assignment by such amplitudes for other assignment with the proper re-coupling of spins and angular momenta. An example of the resulting amplitudes a_α for assignment 2 from Tab. 5.1 is presented in Appendix A.

With these amplitudes and taking into account explicitly their dependence on the momenta the four-fold differential cross section may be generally represented as:

$$\frac{d^4\sigma}{2\pi dM_{23} d\cos\theta_p d\cos\theta_q d\varphi} = \frac{pq}{32(2\pi)^5 s P_a^* (2s_a+1)(2s_b+1)} \Big[A_0 + A_1 q^2 + A_3 p^2 + \frac{1}{4} A_2 q^2 \left(1+3\cos 2\theta_q\right) + \frac{1}{4} A_4 p^2 \left(1+3\cos 2\theta_p\right) + A_5 pq \cos\theta_p \cos\theta_q + A_6 pq \sin\theta_p \sin\theta_q \cos\varphi \Big]. \quad (5.17)$$

The term with A_0 corresponds to *sS* partial waves, the terms with A_1 and A_2 correspond to *pS* partial waves, the terms with A_3 and A_4 correspond to *sP* partial waves and terms with A_5 and A_6 correspond to *pS* and *sP* waves interference. If there are no additional dependencies of A_i on the outgoing particles momenta the equation 5.17 should fully describe the cross section for a three-body reaction.

The general form of the cross section 5.17 is the same for all possible assignments of the particles given in table 5.1. However, the physical meaning of amplitudes A_i depend on the specific assignment. There is no direct relation between amplitudes A_i for different particle assignments similar to that which can be found for amplitudes a_α.

The cross section 5.17 can be integrated over some of the independent variables in order to obtain single differential cross section used in further analysis. The integration over angles may be performed analytically, while the integration over M_{23} have to be performed numerically. The corresponding integrals over M_{23} will be denoted by

$$I_{sS} = \int_{(M_2+M_3)^2}^{(\sqrt{s}-M_1)^2} pq dM_{23}\,, \tag{5.18}$$

$$I_{pS} = \int_{(M_2+M_3)^2}^{(\sqrt{s}-M_1)^2} pq^3 dM_{23}\,, \tag{5.19}$$

$$I_{sP} = \int_{(M_2+M_3)^2}^{(\sqrt{s}-M_1)^2} p^3 q dM_{23}\,, \tag{5.20}$$

$$I_{pS+sP} = \int_{(M_2+M_3)^2}^{(\sqrt{s}-M_1)^2} p^2 q^2 dM_{23}\,, \tag{5.21}$$

The constant factor in equation 5.17 will be denoted by

$$C = \frac{1}{32(2\pi)^5 s P_a^*} \frac{1}{(2s_a+1)(2s_b+1)} \tag{5.22}$$

The integration over $\cos\theta_p$, $\cos\theta_q$ and φ gives the invariant mass M_{23} distribution

$$\frac{d\sigma}{dM_{23}} = 16\pi^2 C pq \left[A_0 + A_1 q^2 + A_3 p^2\right]. \tag{5.23}$$

The integration over M_{23}, $\cos\theta_q$ and φ gives the angular distribution for θ_p

$$\frac{d\sigma}{2\pi d\cos\theta_p} = 4\pi C \left[A_0 I_{sS} + A_1 I_{pS} + A_3 I_{sP} + \frac{1}{4} A_4 \left(1 + 3\cos 2\theta_p\right) I_{sP}\right], \tag{5.24}$$

and similarly the integration over M_{23}, $\cos\theta_p$ and φ gives the angular distribution for θ_q

$$\frac{d\sigma}{2\pi d\cos\theta_q} = 4\pi C \left[A_0 I_{sS} + A_1 I_{pS} + A_3 I_{sP} + \frac{1}{4} A_2 \left(1 + 3\cos 2\theta_q\right) I_{pS}\right]. \tag{5.25}$$

Finally the distribution for φ is obtained by integration over M_{23}, $\cos\theta_p$ and $\cos\theta_q$

$$\frac{d\sigma}{d\varphi} = 8\pi C \left[A_0 I_{sS} + A_1 I_{pS} + A_3 I_{sP} + \frac{\pi^2}{16} A_6 I_{pS+sP} \cos\varphi \right]. \tag{5.26}$$

In the single cross section formulae for four the independent variables the term with amplitude A_5 does not appear. This term describes the correlation between θ_p and θ_q angles. It is possible to construct the expression for the cross section containing term A_5 using different variables as e.g. $\cos\theta_p - \cos\theta_q$ or $\cos\theta_p + \cos\theta_q$. The differential cross section in these variables has a form:

$$\begin{aligned}
\frac{d\sigma}{2\pi d(\cos\theta_p \pm \cos\theta_q)} = 4\pi C \Big[& A_0 I_{sS} + A_1 I_{pS} + A_3 I_{sP} \mp \frac{1}{3} A_5 I_{pS+sP} - \\
& \frac{1}{2} \left(A_0 I_{sS} + A_1 I_{pS} + A_3 I_{sP} + A_2 I_{pS} + A_4 I_{sP} \pm A_5 I_{pS+sP} \right) |\cos\theta_p - \cos\theta_q| + \\
& \frac{3}{4} \left(A_2 I_{pS} + A_4 I_{sP} \right) |\cos\theta_p - \cos\theta_q|^2 - \\
& \frac{1}{4} \left(A_2 I_{pS} + A_4 I_{sP} \mp \frac{1}{3} A_5 I_{pS+sP} \right) |\cos\theta_p - \cos\theta_q|^3 \Big].
\end{aligned} \tag{5.27}$$

6 Analysis of the dd$\rightarrow{}^3$He n π^0

6.1 Run Summary

The data presented in this work have been collected during ten days of production run in the end of 2007. In the experiment the deuteron beam with kinetic energy E_{kin} = 0.350 GeV ($p_{beam} = 1.2 GeV/c$) impinging on a deuterium pellet target was used to initiate the reaction dd $\rightarrow {}^3$He$n\pi^0$. In the Tab. 6.1 an overview of experimental conditions during the data taking period is presented. In the left panel of Fig. 6.1 the beam intensity as mea-

beam energy	0.350 GeV
beam momentum	1.2 GeV/c
pellet rate	4 - 8 kHz
events per pellet	2 - 4
deuterons in flat top	$6 \cdot 10^9$
typical luminosity	$\approx 10^{30}$ cm^{-2}s^{-1}
integrated luminosity	≈ 350 nb^{-1}
magnetic field of the solenoid	1 T
main trigger	fwHea1|fwHeb1|Vfrha1|seln1
cycle length	54 s
data taking within cycle	43 s
duty factor	0.8
DAQ life time	88 %
effective data taking time	420000 s

Table 6.1: List of the parameters valid for production run performed in November 2007.

sured by a beam current transformer (BCT) over the time in cycles is shown. A typical beam cycle obtained during the experiment had a length of 54 s. The visible drop in the intensity is due to the beam target interaction. The flat top period when the beam energy is kept constant and the data are registered by the DAQ system was approximately 43 s. The

variation of the trigger rates over the cycle are illustrated in the right panel of Fig. 6.1. By measuring the ratio of issued and accepted trigger signals, the life time of the data acquisition system was estimated to be 88%.

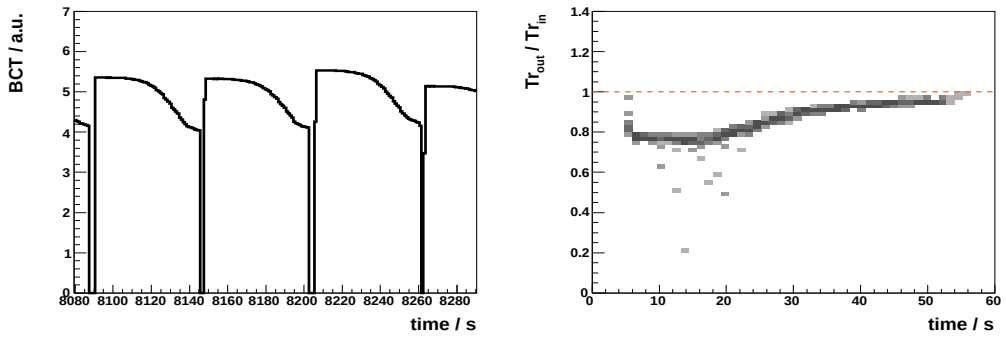

Figure 6.1: The beam intensity over the time in cycles (left). The ratio of accepted to the incoming triggers as a function of time in cycle (right).

During the experiment all detector components of WASA-at-COSY were fully operating. The newly installed Forward Window Counter showed an excellent performance. All modules revealed very uniform (i.e. position independent) response, which was crucial for triggering. This made possible to achieve a high selectivity and efficient background suppression already on the trigger level. For triggering on dd $\rightarrow$ ^{3}Henπ^0 a coincidence between a high energy deposit in both layers of the Forward Window Counter, one or more low energy (E > 20 MeV) neutral clusters in the calorimeter and a veto condition on the first layer of the Forward Range Hodoscope was used. The latter criterion was imposed by small energy of helium ejectiles which are stopped latest in the third layer of the FTH. The threshold in FWC was chosen such that protons (mainly from deuteron break-up) were discriminated while tritons were still in trigger. With these settings the rate from main trigger occupied only up to 20% of the DAQ capabilities (i.e. less than 2000 trigger/s). Thus, it was sufficient room to include into the trigger also other isospin conserving channels as dd $\rightarrow$ ^{3}Hepπ^-, dd $\rightarrow$ tpπ^0 and dd $\rightarrow$ tnπ^+.

To verify if any severe changes of the beam momentum have occurred over the accelerator cycle the behavior of the neutron missing mass in function of time has been checked. The distribution shown in left panel of Fig. 6.2 indicates that beam momentum was kept stable over the time in cycle. This is proven by the position of the missing mass which is centered at the exact mass of the neutron. In order to monitor the performance of the central detector during the experiment, the position of invariant mass of two photons as a function of run number was plotted. The obtained dependence is shown in right panel of Fig. 6.2. The data points are positioned at the pion mass within the statistical fluctuations.

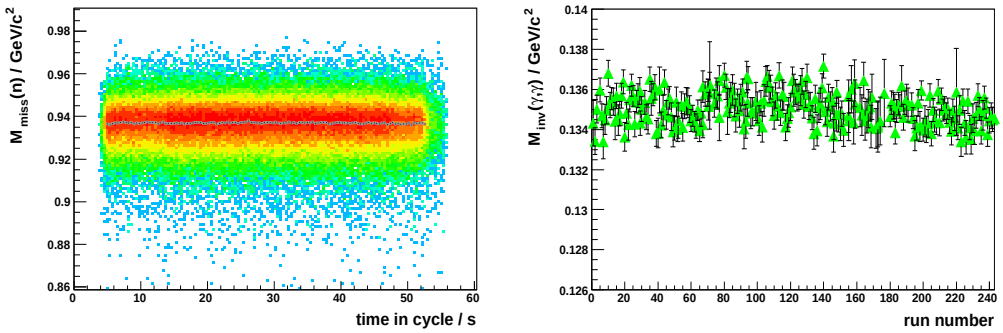

Figure 6.2: The behavior of the neutron missing mass reconstructed from ^{3}He and π^0 over the time in cycle. The slices of the two dimensional distribution were projected onto Y-axis and fitted with gauss function. The mean value obtained from the fit for each slice is indicated by gray horizontal line (left). The invariant mass of two photons as a function of run number (right).

6.2 Event Selection

This chapter contains the preselection criteria that were designed to preferentially select dd $\rightarrow$ ^{3}Henπ^0 events over background processes. In this work two stages of event selection can be distinguished. First is based on hardware triggers while the second makes use of characteristic signature of the physics process we are interested in.

The main trigger fwHea1|fwHeb1|Vfrha1|seln1 set up during the experiment was based on a logic AND of the following trigger patterns:

fwHea1|fwHeb1 - a high threshold on signals from geometrically overlapping elements in both layers of Forward Window Counter detector;

Vfrha1 - veto on any hits in the Forward Veto Hodoscope;

seln1 - one or more neutral clusters in the calorimeter.

The data picked up by this trigger still consists of a large collection of unwanted events. In order to keep only events of interest and to reduce computation time a preselection has been performed. The data were presorted by imposing set of relatively loose requirements listed in Tab. 6.2. The most influential cut applied on light output in FWC1 detector reduced the initial amount of data by approximately 80%. The optimal value for this condition has been found by varying the level of cut and checking how the invariant mass of the two photons is influenced. The multiplicity condition set for the Forward Detector means that we require exactly one charged particle track. In order to be able to reconstruct the angles of particles detected in FD the demand on number of clusters in FPC detector is imposed. Additional selection criteria are based on the

information from Central Detector. To select event candidates for the decay of $\pi^0 \rightarrow \gamma\gamma$ only those events are accepted which contain two neutral clusters in the calorimeter. The MC simulations have shown that photons originating from dd $\rightarrow {}^3$Henπ^0 have energy above 20 MeV and opening angle larger than 30°. Those restrictions were set during the preselection to suppress signals not stemming from the channel of interest. The time difference between the detection of products of pion decay has to be smaller than 40 ns (see Fig. 6.3). It is noteworthy that all conditions applied for the Central

Forward Detector	
Track multiplicity	= 1
Cluster multiplicity in FPC	≥ 2
Light output in FWC1	$\geq$ 3800 ch
The reference signals from the LPS	ON
Central Detector	
Cluster multiplicity in PSB	= 0
Cluster multiplicity in SE	= 2
Time difference between clusters in SE	$\leq$ 40 ns
Opening angle between clusters in SE	$\geq 30^\circ$
Cluster energy in SE	$\geq$ 20 MeV
The reference signals from the LPS	ON

Table 6.2: The criteria of events preselection.

and the Forward detectors have to be fulfilled in coincidence. To ensure that ^{3}He and photons originate from the same event, a cut on the time correlation shown in Fig. 6.3 has been performed. In order to correct for the gain drifts, information from the light pulser system was included during the preselection process. To minimize edge effects due to the geometry of the detector, an additional constraint was applied to the scattering angles of the reconstructed tracks. In the Forward Detector tracks with scattering angles from 3° to 18° were considered while in the Central Detector only photons with θ angles limited to the range between 20° - 169° have been accepted. The validation of the trigger condition was achieved by a request that each event must have energy deposit in both layers of the FWC detector and in the first layer of the FTH as well as one or more neutral clusters in calorimeter. Moreover, there should be no hit in FVH.

For the selected events the four-vectors of the reconstructed particles were used to calculate the missing mass according to formula:

$$\mathrm{MM}(^3\mathrm{He}\pi^0) = \sqrt{\mathbb{P}_{\mathrm{d}}^{\mathrm{b}} + \mathbb{P}_{\mathrm{d}}^{\mathrm{t}} - \mathbb{P}_{^3\mathrm{He}} - \mathbb{P}_{\pi^0}}\,. \tag{6.1}$$

The right panel of Fig. 6.3 presents the missing mass, built of helium and two photons obtained during presorting. The distribution shows the expected peak at the mass of the neutron.

Utilizing presented cuts, a relatively pure sample of dd $\rightarrow$ ^{3}Henπ^0 candidates have been obtained. This preselected data were refined by improving the energy calibration and applying the kinematic fit. The precise calibration guarantees the separation of ^{3}He from lighter particles what yields to complete background elimination. On this level of analysis energy resolution and thresholds for individual detectors are computed. These values are used to smear Monte Carlo data in order to reproduce the experimental resolution.

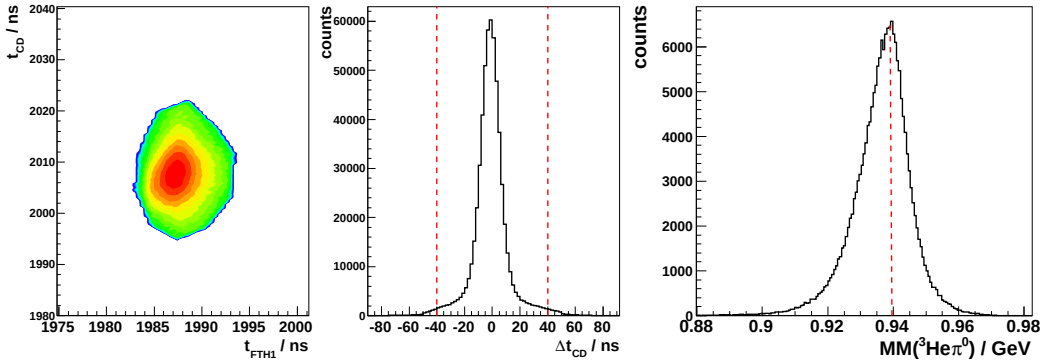

Figure 6.3: The correlation between mean time of two neutral cluster in calorimeter and time detection of ^{3}He measured by FTH1 detector (left). Time difference between two neutral tracks in Central Detector. The tracks are accepted within a time window denoted by red dashed lines (middle). Missing mass reconstructed from ^{3}He detected in the Forward Detector and two photons measured in the Central Detector (right).

6.3 Kinematic Fit

The kinematic fit is a least-square fit with constraints based on the Lagrange multipliers technique. The detailed description of the method can be found in Ref. [81,82]. The basic idea behind the use of kinematic fit is to improve the resolution of measured kinematical variables. All quantities we measure, e.g. energy or angles, have uncertainties which can manifests itself in the population of kinematically forbidden regions of the phase space. The purpose of kinematic fit procedure is to vary measured observables within the uncertainty until certain kinematic constraints are fulfilled. Limits for variation of measured

parameters are determined by the experimental resolution. The constraints are based on physical properties of studied processes and are used to test hypotheses for given reaction. As a result of the kinematic fit the corrected values of energies and angles as well as a value of the correspondingχ^2 is returned. The latter is used to validate fit results. If the proper hypothesis is selected and all resolutions used as input for the kinematic fit are Gaussian shaped then the χ^2 probability function with N degrees of freedom defined as:

$$P(\chi^2|N) = \frac{1}{\sqrt{2^N\Gamma(\frac{1}{2}N)}} \int_{\chi^2}^{\infty} e^{-\frac{1}{2}t} t^{\frac{1}{2}N-1} dt \tag{6.2}$$

should have flat distribution between 0 and 1.

6.3.1 Fit Constraints

The kinematic fit for the reaction dd $\rightarrow {}^3$Henπ^0 makes use of five constraints. Four of them are related to the overall energy and momentum conservation. Additionally the demand on mass of π^0 has been applied. After the definition of reaction hypothesis the information about measured and unmeasured parameters are passed to the fitting routine. In our case we measure 3×3 parameters namely the energy, polar and azimuthal angles of helium and two photons. The neutron is undetected thus we have 3 unmeasured parameters. Having that information the number of degrees of freedom can be calculated as:

$$N = 4 + n_c - u \tag{6.3}$$

where 4 stands for the four conditions due to the four-momentum conservation, n_c is the number of additional constraints and u denotes the number of unmeasured variables. Inserting appropriate values to the Eq. 2.2 results in N = 2.

6.3.2 Error Parametrization

Proper parametrization of uncertainties of the measured physical quantities is one of the most critical part when preparing input for kinematic fit. This is because the fitting routine minimises the χ^2 using the constraints supplied by varying the experimentally measured parameters. The error description can be determined from MC simulation, by comparing the reconstructed observables to the initial values given by the event generator. This procedure can be applied only when experimental data are well reproduced by simulation. Such a prerequisite is realized by smearing of the simulated observables until they match experimental resolutions. The errors for the kinetic energies, polar and azimuthal angles are computed as the absolute difference of the reconstructed and true values from generator.

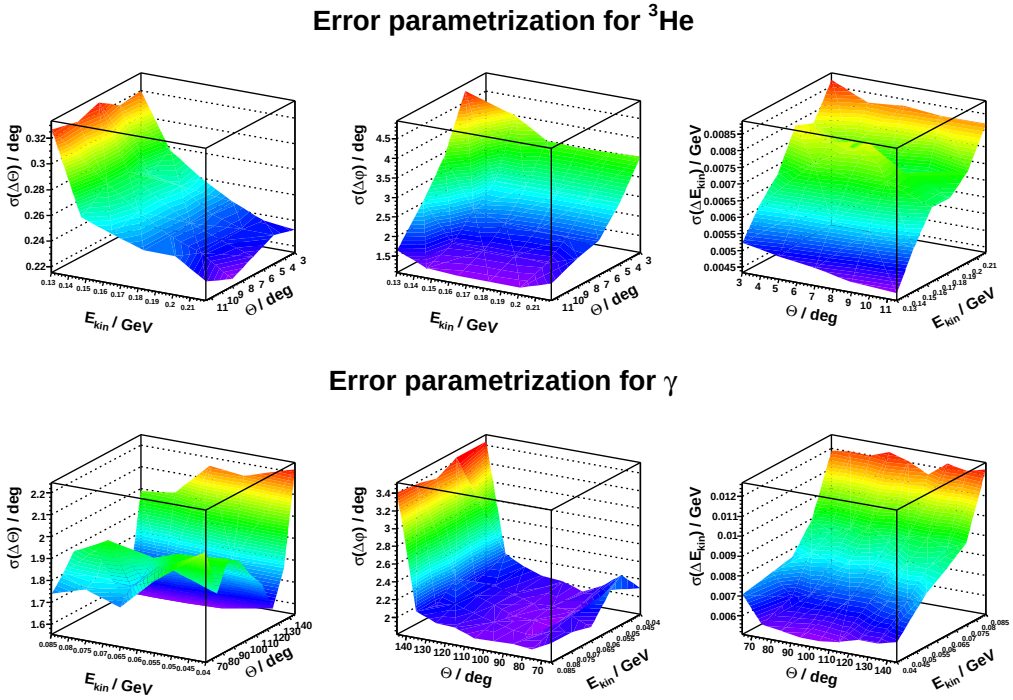

Figure 6.4: The error parametrization of the reconstructed variables θ,φ and E_{kin}.

$$\begin{aligned} \Delta E_{kin} &= E_{rec} - E_{gen}\,, \\ \Delta\theta &= \theta_{rec} - \theta_{gen}\,, \\ \Delta\varphi &= \varphi_{rec} - \varphi_{gen}\,. \end{aligned}$$

The distributions are fitted with a Gaussian function and the obtained width σ is treated as an error of given variable. Systematic studies of the error distributions have been performed by checking if $\sigma(\Delta E_{kin})$, $\sigma(\Delta\theta)$ or $\sigma(\Delta\varphi)$ depend on kinetic energy and scattering angle. For that purpose two dimensional parametrization was applied. The kinetic energy range 130 - 220 MeV for ^{3}He was divided into seven slices of 12 MeV each and the scattering angle range 15° was divided into fifteen intervals of 1° size. In that way whole two dimensional space can be separated into close to one hundred cells. For each cell the errors of E_{kin}, θ and φ are computed. The variation of errors as function of kinetic energy and scattering angle for ^{3}He are presented in upper row in Fig. 6.4. Here, the left plot shows that errors of polar angles of ^{3}He decrease exponentially with the kinetic energy. In the middle picture of the same row, the resolution of the ^{3}He azimuthal angle is shown. As can be seen the error is independent of the energy and rises approximately

linearly with increasing polar angle. The last plot in upper row illustrates the behavior of the error of kinetic energy. One can notice there is almost no dependence on scattering angle and the error is dominated by changes in kinetic energy itself. The resolution gets worse for high energetic ^{3}He. Worsening of resolution can be attributed to smaller energy deposit of ^{3}He in the detector, what affects the energy reconstruction procedure. In the lower row of Fig. 6.4 similar considerations were conducted for photons. Left plot shows that the error of polar angle can depend on the part of the calorimeter where photons were detected. For the forward and backward end-caps where the sizes of crystals are smaller than in the central part the errors are larger. This situation holds also for description of the error of azimuthal angle. In the most right plot the errors of kinetic energy are displayed. They do not depend on scattering angle and get larger with the increase of the energy.

For the parametrization of errors of the kinematic observables which reveal only dependence on one variable, an analytic functions were used. In case of $\sigma(\Delta E_{kin})$ for ^{3}He and $\sigma(\Delta\theta)$ for photons, where variation of errors behave in more complicated way two dimensional tables were prepared. For given value of kinetic energy and scattering angle we can do a table lookup and extract corresponding error.

Before applying the error parametrization some additional studies of systematic deviations have been performed. One noteworthy example is the azimuthal angle of ^{3}He measured in the Forward Detector. The procedure which reconstructs the angles assumes that particles in FD follows a straight track from the vertex, but in reality part of the track lies in the magnetic field of the solenoid. This results in curved trajectories in the region close to vertex. To compensate for this effect the corrections according to [83] have been applied:

$$\Delta\varphi = \frac{0.3 \cdot L \cdot z \cdot B}{P \cdot \cos\theta} \tag{6.4}$$

where z is the charge of the particle in units of electron charge, B is the magnetic field in Tesla, L is the longitudinal component of the particle trajectory in meters, P is the momentum of the particle in GeV/c and θ is the polar angle.

6.3.3 Probability Distribution

The measured parameters of two photons and helium which are given as an input to the kinematic fit are modified within the error limits of that parameter. These modified values can be interpreted in terms of probabilities and χ^2 distribution.

In Fig. 6.5 the χ^2 and the corresponding probability distribution for all fitted events in the data as well as Monte Carlo simulation are shown. The distributions have been obtained for the dd $\rightarrow {}^3$Henπ^0 hypothesis in the kinematic fit. Events which have high χ^2 values are located in the region close to zero in the probability distribution. Those events are not of interest because they most likely do not well satisfy the constraints applied to the fitting procedure. On this level of analysis the data are almost background free (see the right panel of Fig. 6.3) so the rise in the probability distribution for large χ^2 values can not be attributed to background contributions. Since such a trend is also visible in MC

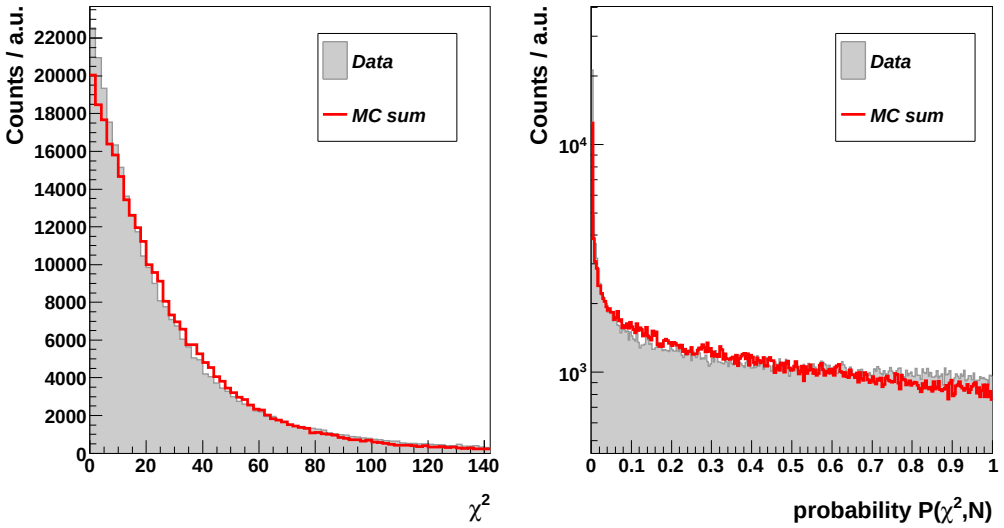

Figure 6.5: χ^2 distribution (left) and the probability distribution (right) obtained from the kinematic fit. The gray histograms represent the data while in red the MC distributions are shown.

it indicates this can be the issue of the error estimation. Least square fit needs Gaussian shaped resolutions as input. Of course, in real life measurement errors rarely follow this distribution exactly and usually have some significant non-Gaussian tails. To verify the correctness of the obtained errors, pull distributions were constructed. The pull value is defined as the difference between measured υ_{rec} and fitted υ_{fit} values obtained by the kinematic fit, normalized by the quadratic error difference.

$$\text{Pull} = \frac{\upsilon_{\text{rec}} - \upsilon_{\text{fit}}}{\sigma^2_{\text{rec}} - \sigma^2_{\text{fit}}} \tag{6.5}$$

The minus sign in the denominator comes from the correlation between the measured and fitted observables. If the errors are correctly estimated and there are no systematic shifts, then the pull quantity will be distributed like a Gaussian centered at zero with σ equal to 1. The examples of pull distributions for experimental data are shown in Fig. 6.6. One can observe that pulls for energy approximately obey a Gaussian distribution. In case of pulls constructed for polar angles, deviation from a Gaussian shape is noticeable. The discrepancy in the width from unity demonstrates the underestimation of the measurement error. On the other hand the reason for such a behavior can also lie in the fact that kinematic fit improves mainly the energy resolution, but has almost no effect on the angular observables. This leads to the situation where in the denominator two comparable quantities appear what can result in some numerical problems. Under investigation was also influence of the fact that neutron was treated in the kinematic fit as an unmeasured particle.

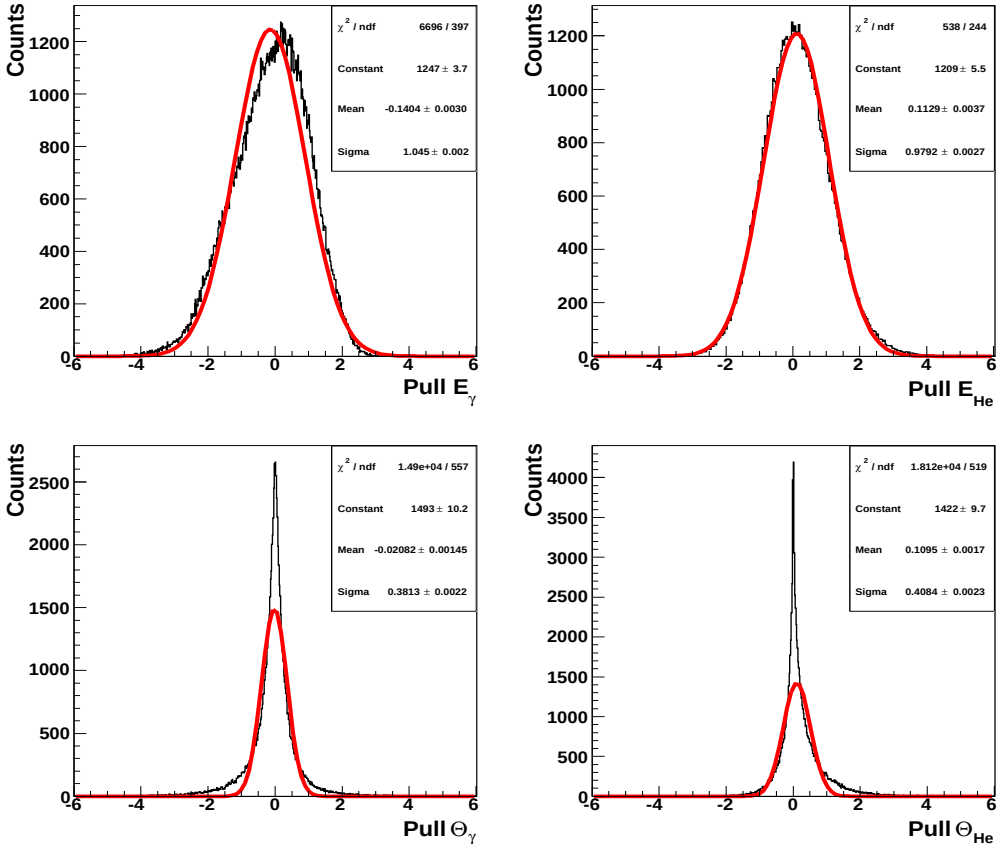

Figure 6.6: Example pull distributions of kinetic energy and polar angle for photons and helium. Plots were made for experimental data. Pulls have been fitted with Gaussian function (red lines). The results of the fit indicate there is no systematic shift between the reconstructed and true values, however errors for some variables after the fit are underestimated.

For such a case it is important to provide reasonable starting values for the unmeasured variables. In this approach the kinematic constraints are linearized at each iteration step and Newton's method is used to find the minimum. Thus to avoid a risks of non convergent solution or finding some other local minimum the starting values for neutron were extracted from the missing four momentum vector.

For further analysis events with a probability value below 0.1 have been excluded. Those events do not well satisfy the constraints applied in kinematic fit, either because they were wrongly reconstructed or they stem from background. The criteria used to select the limit for the probability cut are presented in section 7.2.

6.4 Comparison of Simulation and Experimental Data

Before comparing results of simulations with the experimental data the symmetrization procedure has been applied to the data. This step was performed in order to reproduce events which were lost due to the acceptance limitations. When looking on angular distributions of ^{3}He in center-of-mass system (see left panel of Fig. 6.7) one can observe the lack of events close to $\cos\theta_{He} = 1$ and for $\cos\theta_{He} < 0$. The first appears because of geometrical boundaries of FD detector while the latter is due to the energy threshold. The

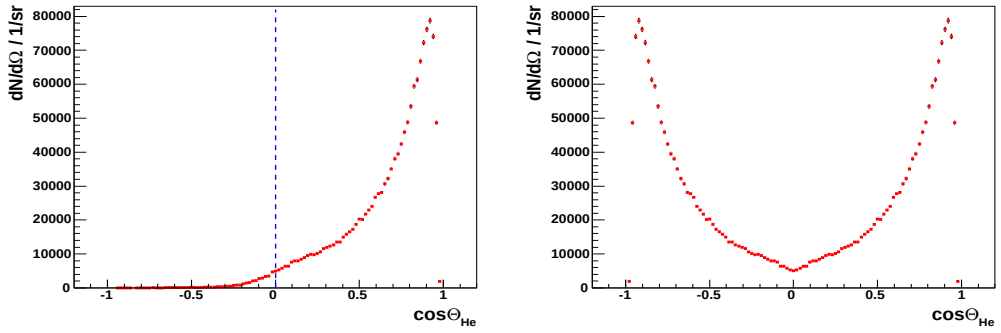

Figure 6.7: The distribution of scattering angle in CM system plotted for ^{3}He. All events located above $\cos\theta > 0$ (denoted by dashed, blue line) undergo of symmetrization (left). The same plot after symmetrization procedure (right).

symmetrization was realized in the following manner. First, ^{3}He four momentum vector is calculated in the global center of mass system and only events which fulfill condition $\cos\theta_{He} > 0$ are considered. In each such an event for helium, neutron and pion the P_z component of momentum vector is replaced by $-P_z$. The symmetrized angular distribution of ^{3}He in center-of-mass system is shown in right panel of Fig. 6.7.

After applying all the selection criteria described in section 6.2, the experimental data can be presented in the Jacobi-coordinates system (see Section 5.1). The corresponding distributions for three independent assignments (see Tab. 5.1) of the particles in dd $\rightarrow$ ^{3}Henπ^0 reaction are displayed in Fig. 6.8 - Fig. 6.10. To describe the experimental distributions shown in Fig. 6.8 - Fig. 6.10 two phenomenological models presented in Section 5 were employed. Let us first concentrate on quasi-free reaction model. In this approach, reaction dd $\rightarrow$ ^{3}Henπ^0 may proceed with a spectator neutron stemming from the deuteron beam or the deuteron target. For the latter case we have constructed generator (description in 4.1.2 and 5.3) in which any produced spectrum can be absolutely normalized. Such a treatment allows to compare normalized data directly with the generator output passed through the WMC (see 4.1.4) and judge about the quasi-free contribution. For the quasi-free reaction, sample of one million events have been prepared. Half of the events were generated according to the case where neutron spectator comes from the

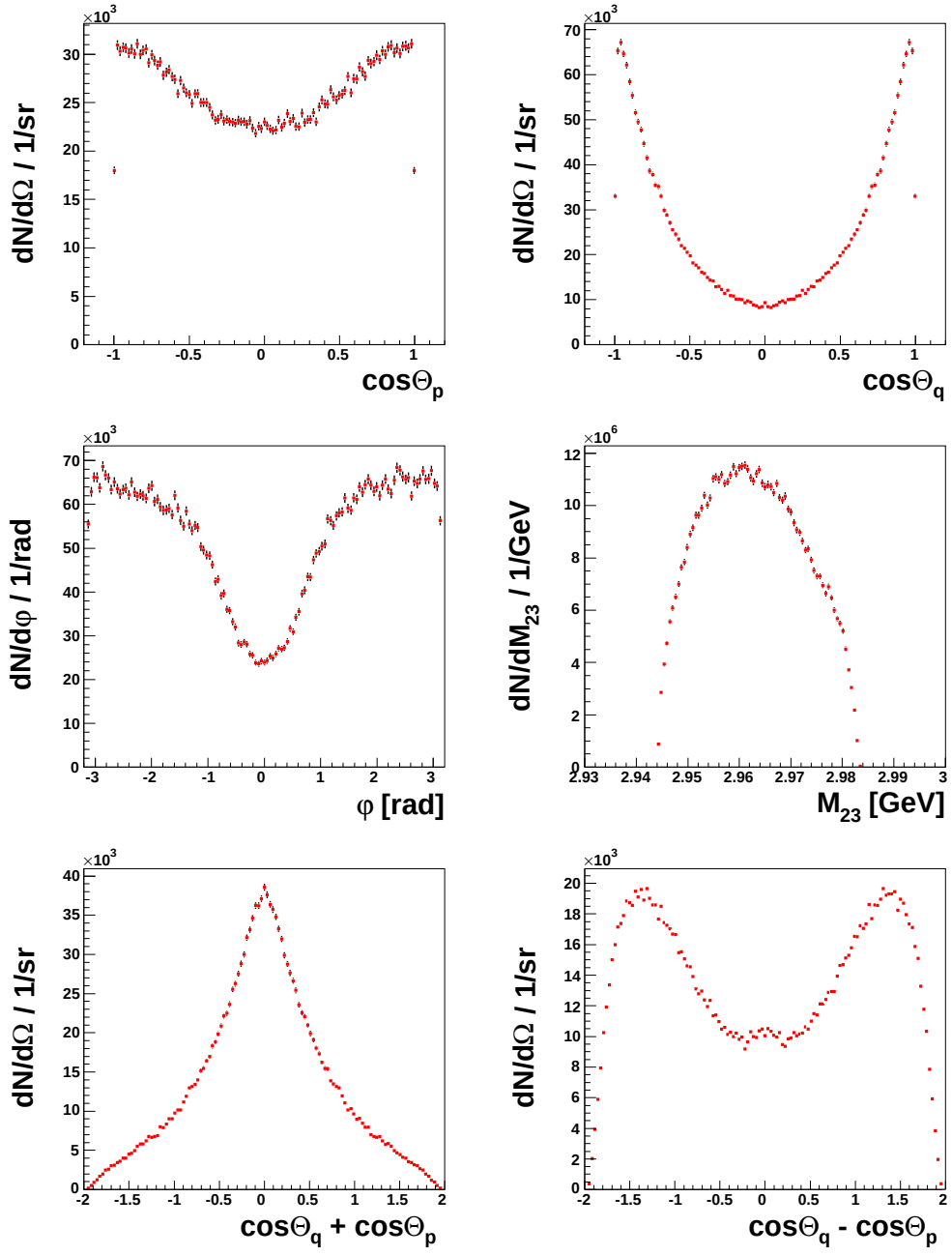

Figure 6.8: Experimental differential distributions (no acceptance corrections) in variables (see Section 5.1) chosen for description of 3-body reaction dd $\rightarrow$ ^{3}Henπ^0. The plots are made for "assignment number" equals to two (see Tab. 5.1).

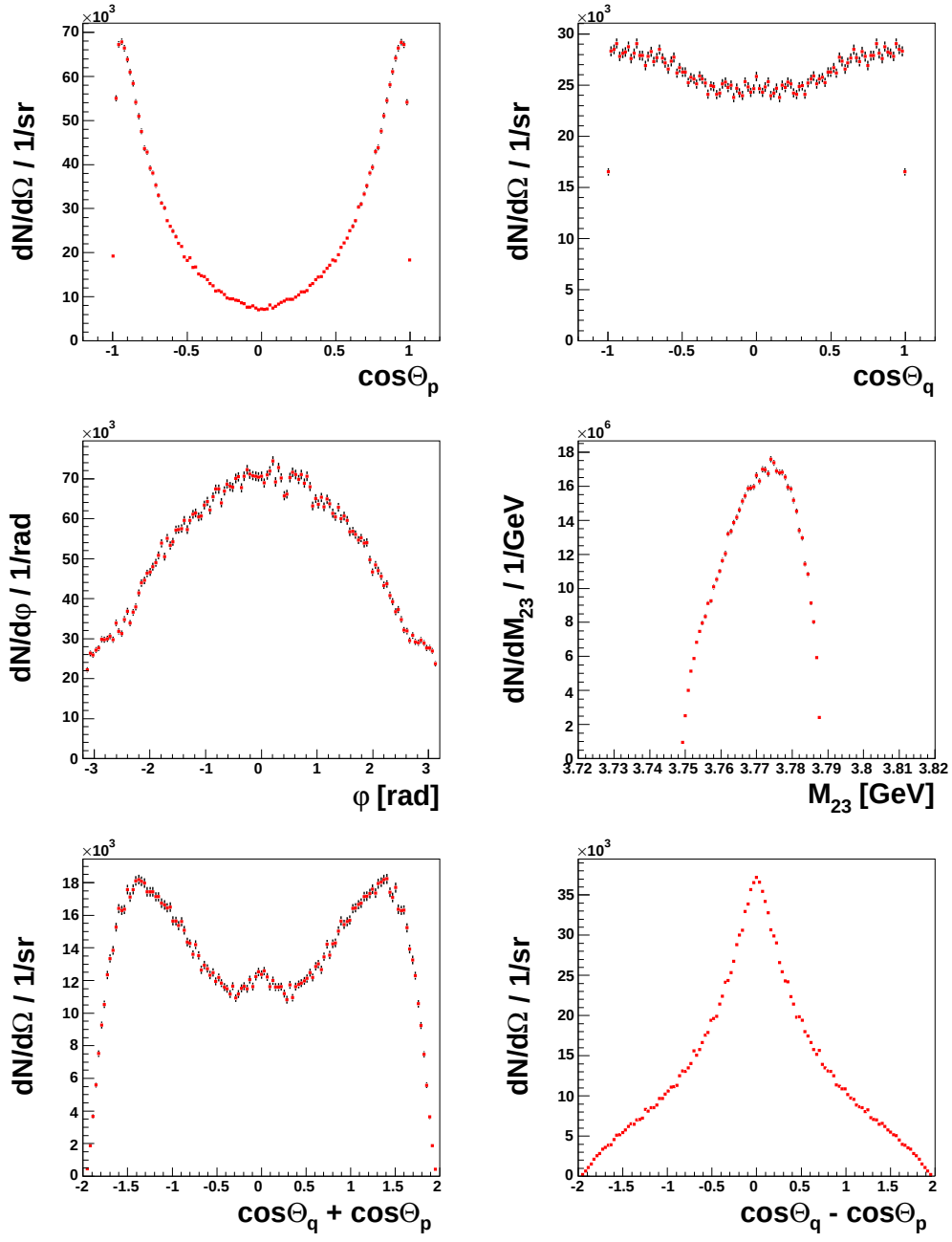

Figure 6.9: Experimental differential distributions (no acceptance corrections) in variables (see Section 5.1) chosen for description of 3-body reaction dd $\rightarrow {}^3\mathrm{He}n\pi^0$. The plots are made for "assignment number" equals to three (see Tab. 5.1).

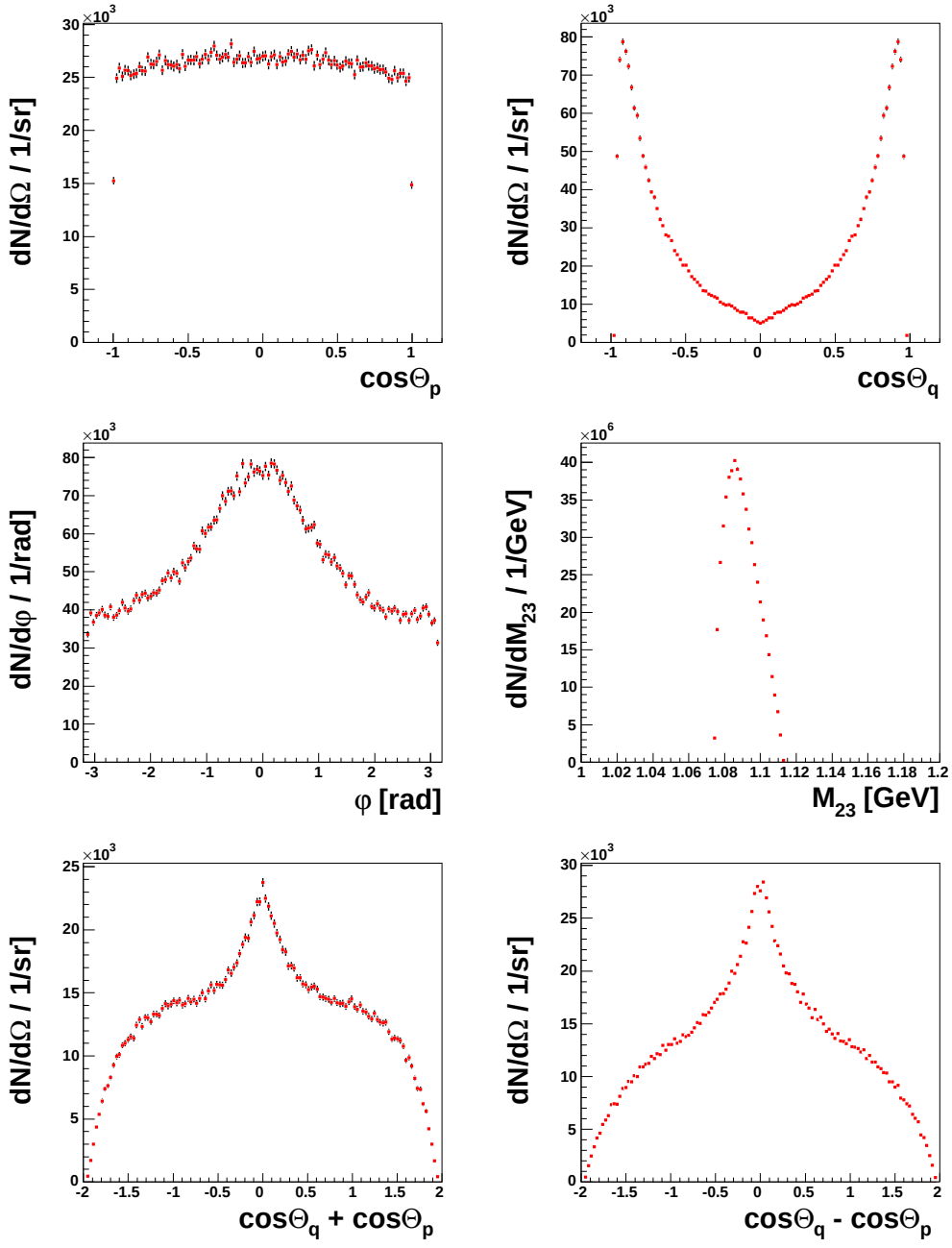

Figure 6.10: Experimental differential distributions (no acceptance corrections) in variables (see Section 5.1) chosen for description of 3-body reaction dd $\rightarrow {}^3$Henπ^0. The plots are made for "assignment number" equals to one (see Tab. 5.1).

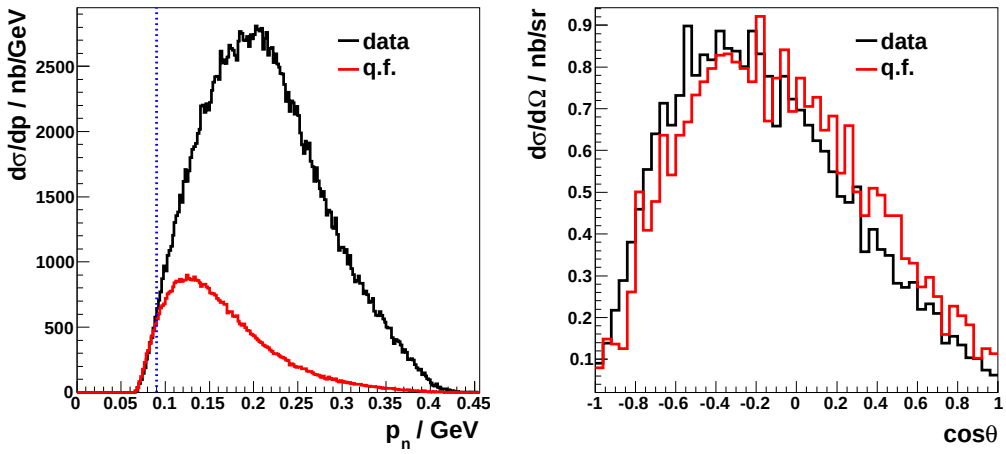

Figure 6.11: In the left panel the momentum distribution of the neutron stemming from $dd \rightarrow {}^3He n\pi^0$ for data (black line) and quasi-free model (red line) is shown. In the right panel the scattering angle of pion in center of mass of subsystem ${}^3He - \pi^0$ is presented. The distribution contains only events for which the neutron momentum is smaller then 90 MeV (the cut is indicated by blue dashed line in left panel). The data and model calculations are not corrected for acceptance.

target and the other half corresponds to the situation where the neutron spectator originates from the beam. The obtained sample was used as an input for MC simulation. After a full detector simulation has been conducted, MC sample was analyzed with the same conditions as used in the analysis of experimental data. Before experimental distributions were compared to the corresponding MC spectra, the absolute normalization had been applied. The quasi-free reaction was normalized using the cross section presented in Section 4.1.2. In order to normalize data, the integrated luminosity calculated in section 6.7 was exploited.

To verify the agreement between the absolutely normalised data and the MC simulations the distribution of the neutron momentum has been checked. In the left panel of Fig. 6.11 differential cross-section as a function of neutron momentum is shown. One can notice that in the region of neutron momentum below 90 MeV the data are dominated by the quasi-free reaction. It is clearly visible when comparing the scattering angle of the pion in center-of-mass of subsystem ${}^3He - \pi^0$. This distribution, obtained after applying cut (indicated by blue dashed line) on neutron momentum is presented in right panel of Fig. 6.11. The experimental shape is fairly well reproduced by quasi-free model with a spectator neutron stemming from the deuteron target. This result allows to fix the contribution of quasi-free process in the data. As Monte Carlo studies have shown, the contribution of quasi-free reaction with neutron spectator originating from the deuteron beam is negligible. This is caused by ${}^3He$'s energy due to which most of them are stopped before first layer of FWC detector, therefore those events can not be reconstructed.

The second step of comparison of MC simulation and data is the inclusion of model based on partial wave expansion for three-body reaction. As described in Section 5.4.2 in this approach the total cross section can be expressed by seven terms corresponding to different partial waves. Those terms in form of matrix elements $|T|^2$ (definition in Section 4.1.3) were used as a weights during the event generation. Based on that seven samples of 10^6 events have been simulated.

The comparison of the experimental data and Monte Carlo simulations represented in the Jacobi-coordinates was done by fitting the sum of the simulated distributions to the experimental distributions. The ideal situation would be to fit the data in four-dimensional space defined by independent variables $M_{23}, \cos\theta_q, \cos\theta_p$ and φ. However, this solution is not feasible due to the statistical limitations. If each fitted histogram would be divided into ten bins then our four-dimensional space would contain 10^4 cells. The total statistics achieved in the analysis yields to about 170000 events what gives less then twenty events per cell. Therefore, for fitting the projections of four-dimensional space were used. Besides $M_{23}, \cos\theta_q, \cos\theta_p, \varphi$ histograms two additional spectra have been included for fitting: $\cos\theta_p - \cos\theta_q$ and $\cos\theta_p + \cos\theta_q$. For the fit the following χ^2 function was defined:

$$\begin{aligned} F_{mc} &= A_0H_0 + (A_1 + A_2)H_1 + (A_1 - A_2/2)H_2 + (A_3 + A_4)H_3 \\ &\quad + (A_3 - A_4/2)H_4 + A_5H_5 + A_6H_6 + A_7H_7 \end{aligned} \tag{6.6}$$

$$\chi^2 = \sum_{k=1}^{nbin} \frac{(F_{exp} - F_{mc})^2}{\sigma_{exp}^2 + \sigma_{mc}^2} \tag{6.7}$$

The expression for F_{mc} is transformed formula 5.17 derived from partial wave decomposition with added term A_7H_7 corresponding to quasi-free process. In the expression Eq. 6.6 the fit coefficients appear as $A_0, .., A_7$, while $H_0, .., H_7$ are different MC contributions as defined in Tab. 4.1. To obtain the fit parameters $A_0, .., A_7$ which would minimize the deviations of the MC predictions from the experimental points represented by F_{exp}, the χ^2 minimization method was used. It is noteworthy that during the minimization the parameter A_7 which corresponds to quasi-free contribution was fixed and equal to one. The results of the fit for three different assignments (see Tab. 5.1) of the particles are presented in Fig. 6.12 - Fig. 6.14. From the comparison we can conclude that the model used for Monte Carlo simulations describes the experimental data very well. Of course the final conclusion can be drawn after the differential cross-section for experimental data are acceptance corrected. Then the resulting distributions can be compared directly to the theoretical predictions.

6.5 Reconstruction Efficiency

Before we proceed with the evaluation of corrections for the detector acceptance some studies related to reconstruction efficiency will be shown. During the estimation of overall reconstruction efficiency following factors should be considered: the geometric accep-

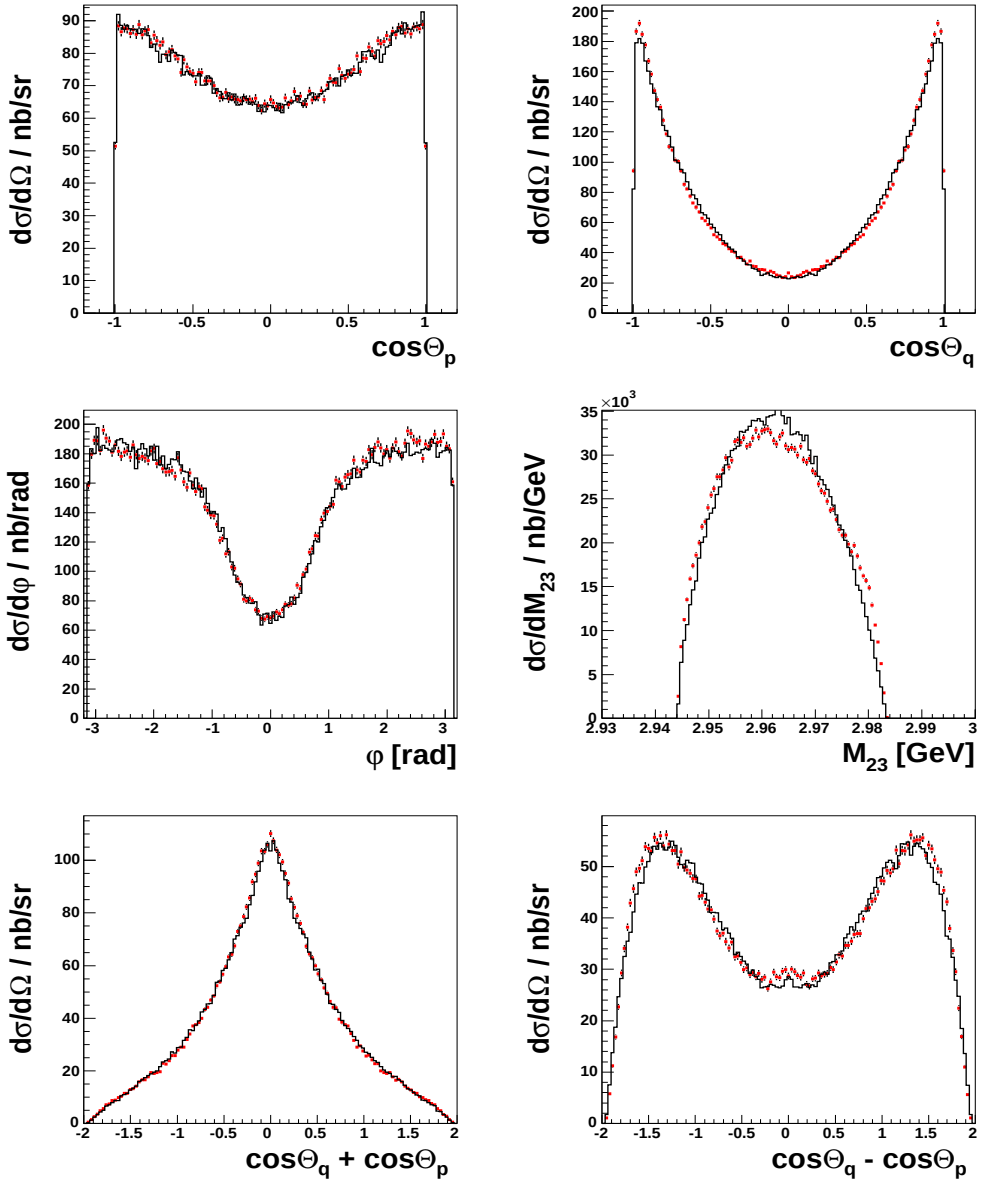

Figure 6.12: The distributions of independent variables calculated according to the quasi-free and partial wave decomposition of dd $\rightarrow {}^3$Henπ^0 reaction. The six spectra compares the experimental data (red dots) with the results from the MC (black solid line). The data are absolutely normalised but not corrected for acceptance, similarly as MC results. The MC curve corresponds to the sum of quasi-free and seven terms from partial wave decomposition. The plots are made for "assignment number" equals to two (see Tab. 5.1).

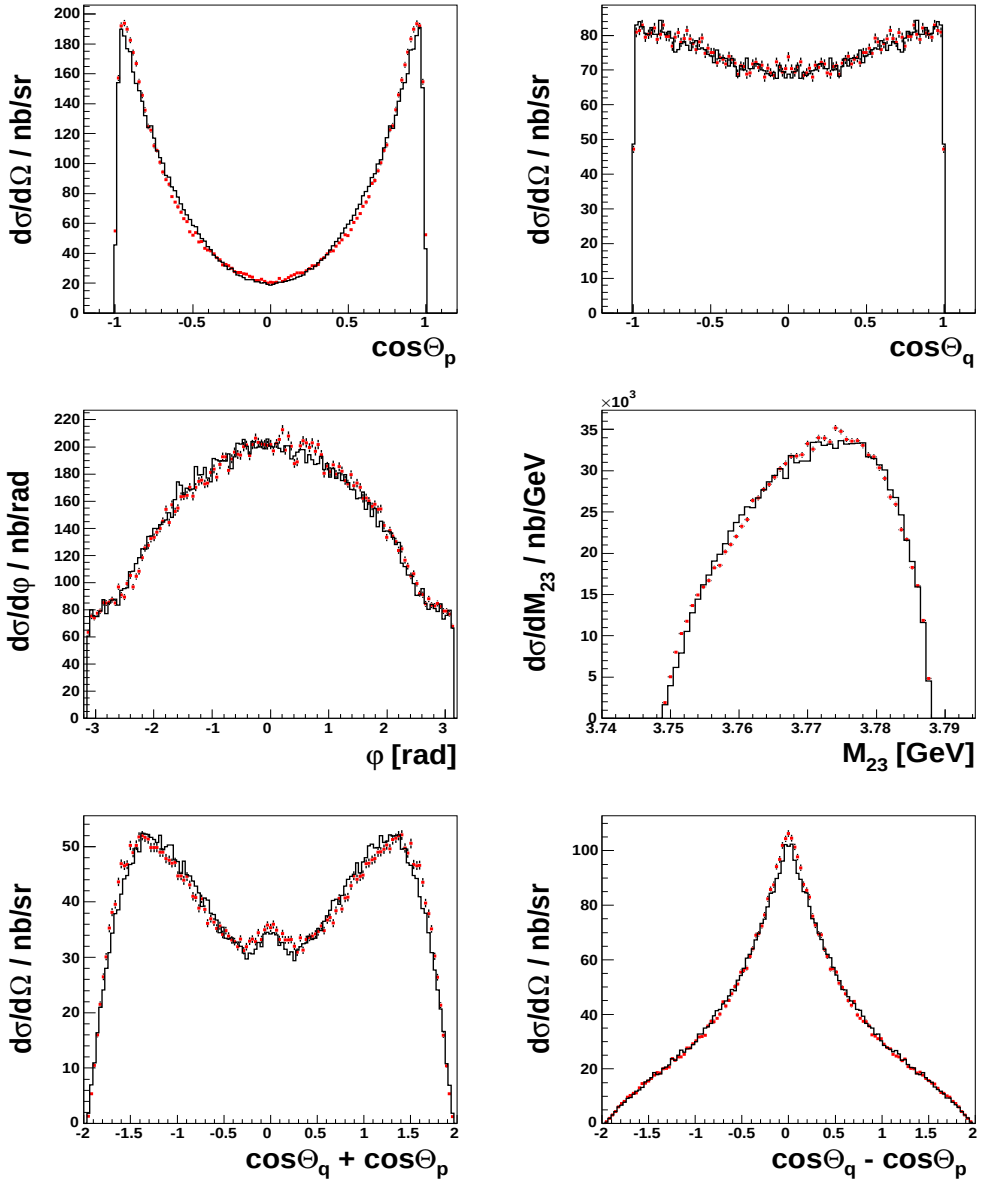

Figure 6.13: The distributions of independent variables calculated according to the quasi-free and partial wave decomposition of dd $\rightarrow {}^3$Henπ^0 reaction. The six spectra compares the experimental data (red dots) with the results from the MC (black solid line). The data are absolutely normalised but not corrected for acceptance, similarly as MC results. The MC curve corresponds to the sum of quasi-free and seven terms from partial wave decomposition. The plots are made for "assignment number" equals to three (see Tab. 5.1).

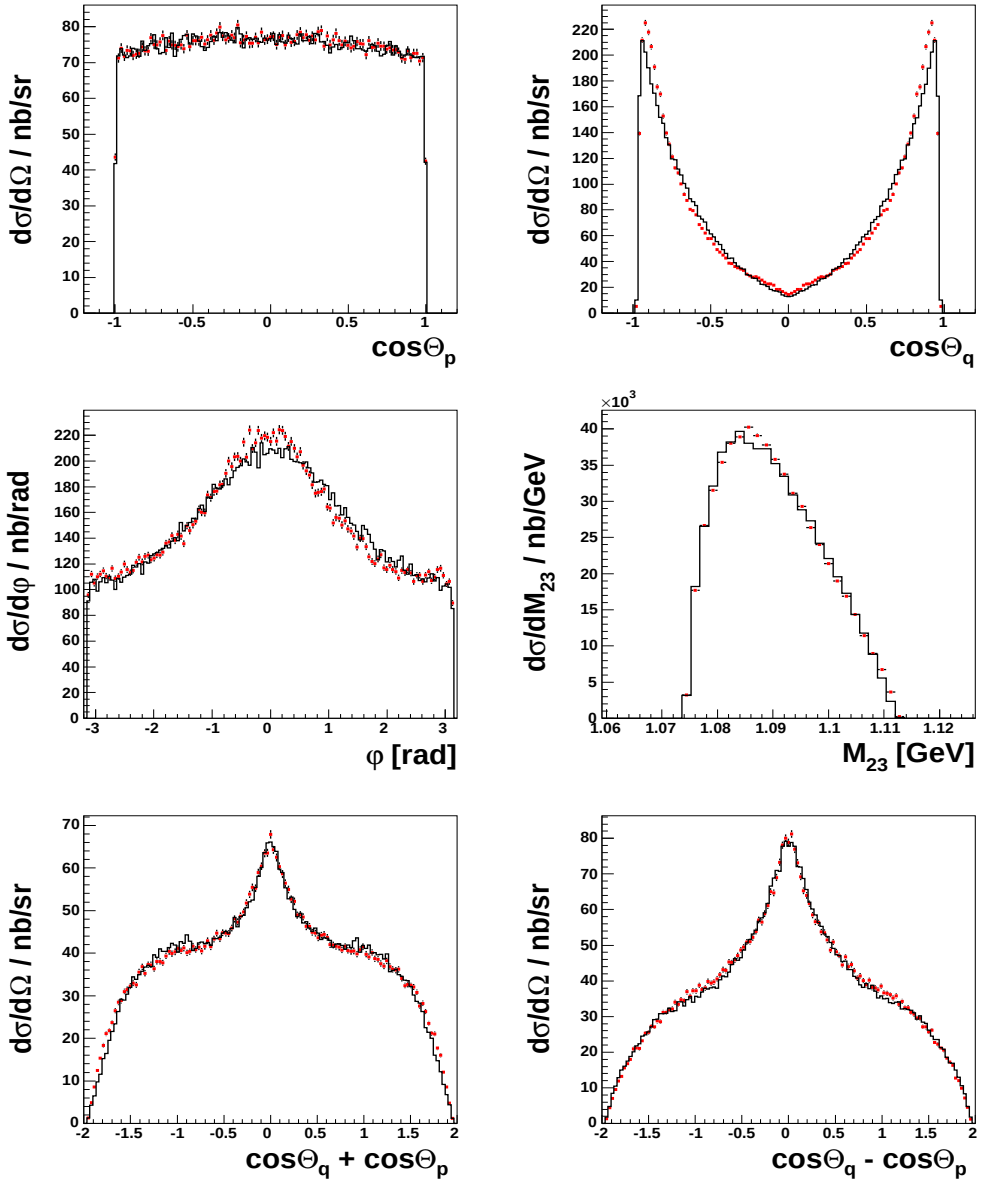

Figure 6.14: The distributions of independent variables calculated according to the quasi-free and partial wave decomposition of dd $\rightarrow {}^3$Henπ^0 reaction. The six spectra compares the experimental data (red dots) with the results from the MC (black solid line). The data are absolutely normalised but not corrected for acceptance, similarly as MC results. The MC curve corresponds to the sum of quasi-free and seven terms from partial wave decomposition. The plots are made for "assignment number" equals to one (see Tab. 5.1).

tance, the detection efficiency and the efficiency of algorithms used for events reconstruction. The influence of those effects on data and MC sample can be tested by comparison the number of events on different stages of the analysis. If MC simulations reproduce experimental distributions then any cut applied during the analysis chain should affect data and MC in comparable way. This is valid under assumption that real data and simulations are analyzed with exactly the same software program.

To determine purely geometric acceptance for the dd $\rightarrow {}^3$Henπ^0 it is sufficient to use information from event generator after imposing restriction on scattering angles according to the geometry of detection setup. In Fig. 6.15 the kinematical distribution for helium and photons are displayed, where the blue lines indicate the acceptance of the WASA detector. The geometric acceptance calculated under assumption that ^{3}He and two photons are detected in coincidence inside the sensitive ranges of the WASA system is found to be 82%. In order to evaluate the reconstruction efficiency, the WASA Monte Carlo simulation was

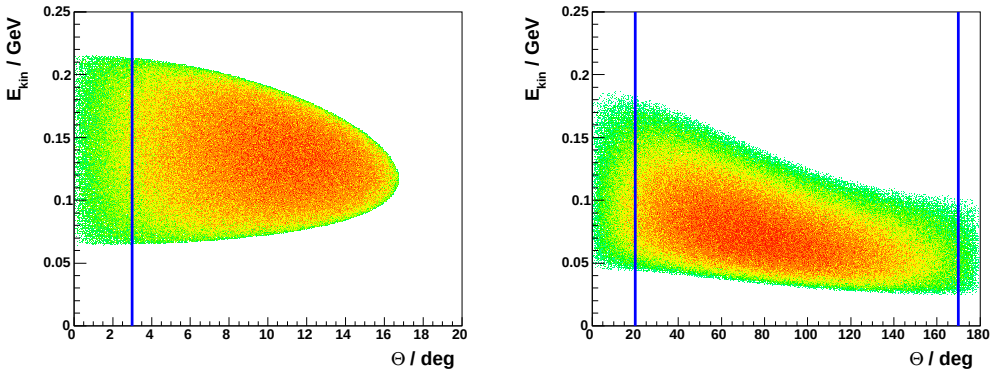

Figure 6.15: The correlation between the kinetic energy and the scattering angle for ^{3}He measured in FD detector (left), and photons detected in CD detector (right). The blue lines indicate the geometrical acceptance of the WASA detector.

used. A sample of $7 \cdot 10^6$ dd $\rightarrow {}^3$Henπ^0 events according to the approach based on partial wave expansion have been generated. Additionally the MC input was supplemented by 10^6 events for the quasi-free reaction. Both samples have been processed by the MC simulation and the output was analyzed with the same program as the experimental data. The reconstruction efficiency was computed as the ratio of events which remain after specific cuts in the analysis and the total number of generated events. In Table 6.3 the efficiencies of the selected cuts applied for data and MC simulation are gathered. The notations used for cut description is following: C1 - number of events after selection of candidates for the dd $\rightarrow {}^3$Henπ^0, C2 - for each event the kinetic energy of ^{3}He has to be reconstructed, the missing mass of neutron should fulfill condition: $0.925 \leq m_n \leq 0.950$ [GeV], C3 - only events with cut on probability distribution $P(\chi^2, N) > 0.1$ are accepted. As can be seen from Table 6.3 the largest drop of efficiency is due to the event candidate selection. After this step data are expected to be background free, what is visible in Fig. 6.3. Therefore,

Cut	MC Phase Space	MC Quasi – free	MC Sum	Data
-	$7 \cdot 10^6$	10^6	$8 \cdot 10^6$	
C1	1726284	147722	1874006	288135
C2	1323112	121635	1444747 (77%)	221473 (77%)
C3	1049958	97068	1147026 (79%)	169824 (77%)

Table 6.3: The overall reconstruction efficiency for the reaction dd $\rightarrow {}^3\mathrm{He}n\pi^0$. In fourth and fifth column the efficiencies of the cuts applied for combined Monte Carlo samples and data are shown. The efficiencies for the subsequent cuts are computed relative to the previous one.

any further selection criteria (kinematic fit) which aimed mainly for increasing resolution should affect data and MC simulation in roughly the same way. This is reflected by the results given in fourth and fifth column of Table 6.3. The fact that cut on probability distribution of the kinematic fit $P(\chi^2, N) > 0.1$ rejects instead of 10% almost 23% can be attributed to non-Gaussian error distribution. This makes that probability distribution is not flat but peaked towards the small values of $P(\chi^2, N)$. The influence of the overall reconstruction efficiency on the different distributions will be discussed in Section 7.2.

6.6 Acceptance Correction

Before any physics conclusion in the interpretation of the data can be drawn, all experimental distributions have to be corrected for the overall efficiency. If the data covered full acceptance range than any model would be applicable to perform acceptance and inefficiencies corrections. In our experiment that was not the case. Therefore, it was crucial to provide model which describes experimental data as good as possible. This should also help to minimize effects like finite resolution or limited acceptance which causes that event migration from the histogram bins they are supposed to populate according to their original kinematics to the neighboring ones.

In principle, two methods can be applied to perform acceptance corrections. First is based on multidimensional corrections. In this case acceptance is expressed as a function of independent variables which describe the studied reaction unambiguously. For 3-body unpolarized reaction four independent variables can be identified to correct data in a model independent way. In this approach, each experimental event is weighted by 4-dimensional function. There were attempts to employ the method for this work, however, due to the

statistics limitations and acceptance holes a multidimensional corrections did not provide satisfying results. Instead, one-dimensional corrections have been used. The application of this type of corrections requires model that resembles the data. As can be seen from Fig. 6.12 - Fig. 6.14 the model presented in Section 5 meets those requirements. The

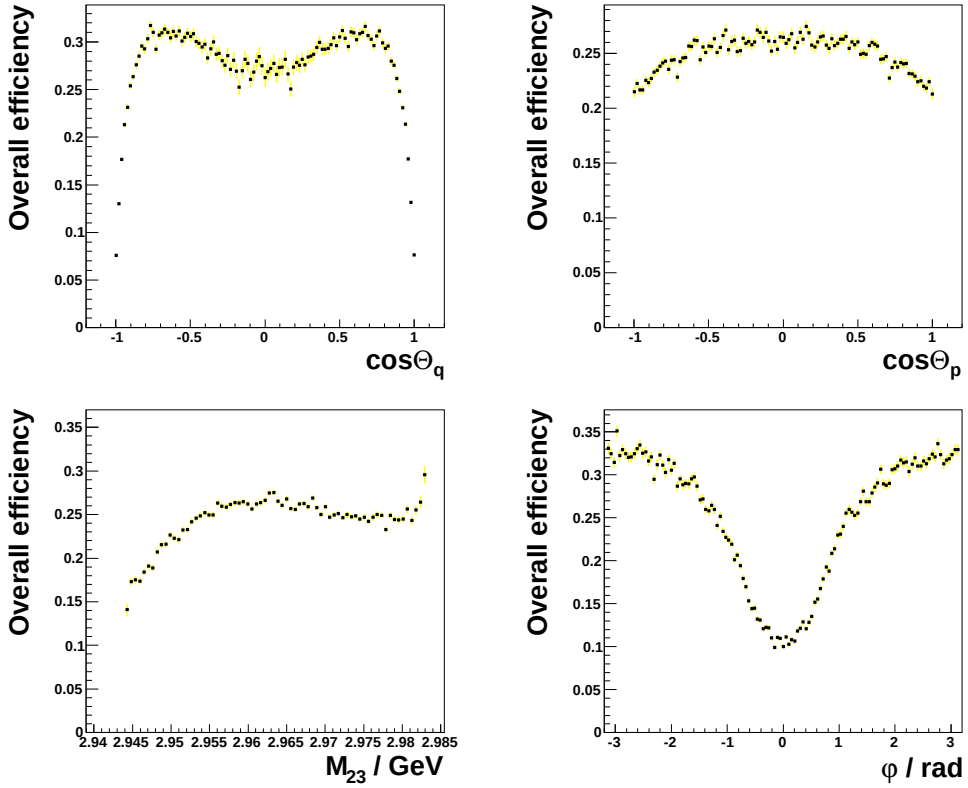

Figure 6.16: Overall efficiency corrections for independent variables $\cos\theta_q, \cos\theta_p, M_{23}, \varphi$. The acceptance correction functions were obtained using mixture of quasi-free process and model based on partial wave expansion for three-body reaction (see Section 6.4).

acceptance correction factors for distributions of interest were prepared in form of one-dimensional histograms according to following formula:

$$F_{\text{eff}-\text{acc}} = \sum_{k=0}^{7} A_k R_k / \sum_{k=0}^{7} A_k H_k \tag{6.8}$$

where H_k denotes the histograms obtained from the generator while R_k refers to the reconstructed histograms from MC simulations. The number of terms in the sum corresponds to the number of MC contributions fitted to the data (see Eq. 6.6) with A_k being the fit coefficients. The acceptance correction distributions derived for exemplary differential cross-sections are shown in Fig. 6.16.

6.7 Luminosity Determination

In order to calculate the cross section for dd $\rightarrow$ ^{3}Henπ^0 the luminosity has to be determined. The relation between luminosity L and the cross section σ can be written as:

$$L = \frac{N_{exp}}{\sigma \, \varepsilon} \tag{6.9}$$

where N_{exp} is the number of dd $\rightarrow$ ^{3}Hen events measured in the experiment, ε is the efficiency and acceptance correction function and σ is the cross section of reference reaction measured at the same beam energy as dd $\rightarrow$ ^{3}Henπ^0.

In this work to determine luminosity the measurement of dd $\rightarrow$ ^{3}Hen has been performed. The events were collected with the minimum bias trigger (prescaled with a factor of 100) which requires exactly one hit in first plane of FRH detector. In order to extract only events of interest a set of selection criteria has been applied. To start with, one charged track in FD is required, that gives a signal in the FPC and reaches the FRH1 plane. The latter condition is exploited for comparison of the energy deposited by different particles. Since ^{3}He stemming from dd $\rightarrow$ ^{3}Hen are mostly stopped in FRH1 they form distinct peak which is clearly separated from the protons and deuterons stemming from break-up reactions. Applying cut on energy deposit $\Delta E_{FRH1} \geq 100$MeV we were able to reduce background contribution to negligible level. It is also noteworthy that events were

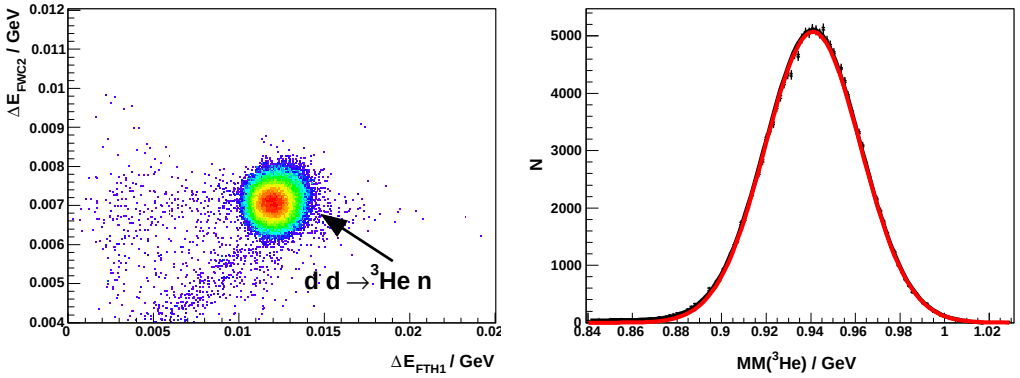

Figure 6.17: The correlation between energy deposited in FWC2 versus FTH1 for ^{3}He stemming from binary reaction (left). In the right panel the ^{3}He missing mass distribution is shown. Pronounced peak at the mass of the neutron can be observed. A Gaussian fit is represented by red line.

selected without any requirement on reconstruction of the neutron. The quality of background suppression is demonstrated in Fig. 6.17. Left panel shows the correlation between energy loss of ^{3}He in first layer of the Forward Window Counter versus energy loss in the first layer of the Forward Trigger Hodoscope. Right panel displays helium missing mass

calculated according to the formula:

$$\mathrm{MM}(^3\mathrm{He}) = \sqrt{\mathbb{P}_{\mathrm{d}}^{\mathrm{b}} + \mathbb{P}_{\mathrm{d}}^{\mathrm{t}} - \mathbb{P}_{^3\mathrm{He}}} \tag{6.10}$$

The resulting missing mass distribution reveals a background free peak at the mass of the

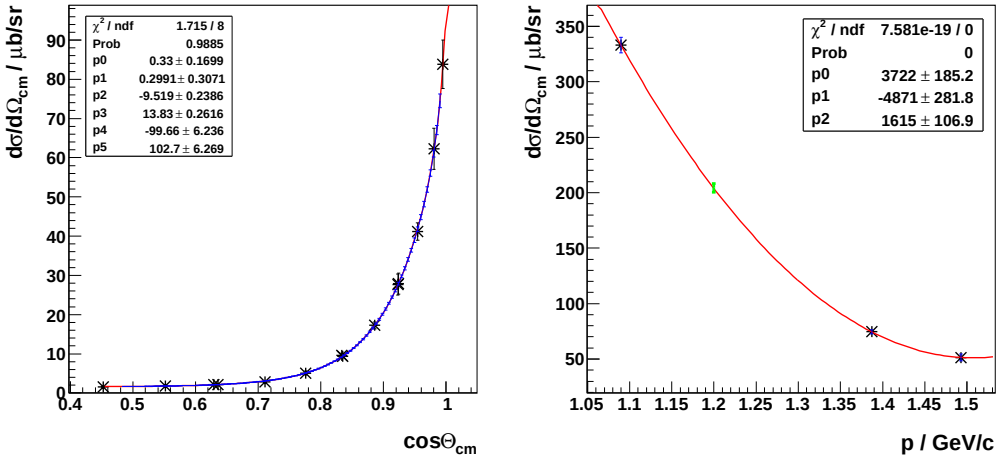

Figure 6.18: In left panel dependence $d\sigma/d\Omega_{cm}(\cos\theta_{cm})$ for selected momentum (1.387 GeV/c) is fitted with function 6.12. Fit function is shown in red. The blue bars correspond to confidence intervals calculated for fitted function. Right panel shows $d\sigma/d\Omega_{cm}$ as a function of momentum. The dependence was fitted by a polynomial of second order. The value of cross section for our beam momentum (1.2 GeV/c) is displayed in green. The width of the bar corresponds to the error calculated as confidence interval.

neutron. This spectrum is fitted with a Gaussian function and from the fit parameters the total number N_{exp} of detected dd $\rightarrow$ ^{3}Hen events was extracted. To determine the cross section we used the data presented in Ref. [84]. Authors measured the dd $\rightarrow$ tp reaction for several beam momenta between 1.09 GeV/c - 1.78 GeV/c and dd $\rightarrow$ ^{3}Hen for beam momenta in the range of 1.1 GeV/c - 2.5 GeV/c. Moreover, they showed that cross sections for both channels measured at the same beam momentum (1.65 GeV/c) are almost identical. Based on that assumption we employed the dd $\rightarrow$ tp reaction to perform interpolation and calculate σ for our beam momentum. We have chosen this channel instead of dd $\rightarrow$ ^{3}Hen because it delivers more points for interpolation in the region close to the 1.2 GeV/c. The tritons cover the c.m. angular range between 0 and 65° what corresponds to 0° - 22° interval in the laboratory system. Those boundaries coincide with the region where we measure ^{3}He from binary reaction. In order to perform interpolation, data for beam momenta of 1.109 GeV/c, 1.387 GeV/c, 1.493 GeV/c and 1.651 GeV/c were exploited.

First, the original data are recalculated from $d\sigma/dt$ to $d\sigma/d\Omega_{cm}$ using following formula:

$$\frac{d\sigma}{d\Omega_{cm}} = \frac{1}{\pi} p^*_d p^*_{He} \frac{d\sigma}{dt} \tag{6.11}$$

where p^*_d and p^*_{He} denote the momenta of deuteron and helium in global c.m. system.

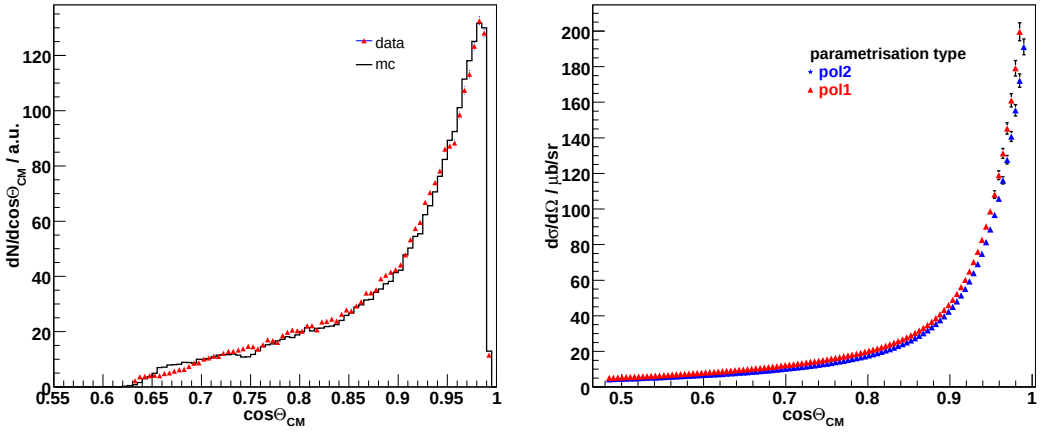

Figure 6.19: Left: Comparison of angular distribution of ^{3}He for MC simulation and data. The Monte Carlo sample was generated based on parametrized cross section from [84] data. The MC distribution has been normalized to the number of events in the experimental spectrum. Right: Parametrized differential cross section of the reaction dd $\rightarrow$ ^{3}Hen at p_{beam} = 1.2 GeV/c. Different colors represent different fit functions.

In the next step for each momentum, $d\sigma/d\Omega_{cm}$ is plotted as a function of $\cos\theta_{cm}$ and fitted (see left panel of Fig. 6.18) with the empirical parametrization [84]:

$$f(\theta_{cm}) = \sum_{i=1}^{3} \alpha_i e^{\beta_i \cos\,\theta_{cm}} \tag{6.12}$$

Using the α_i and β_i constants from the fit we can now choose $\theta_1, ..., \theta_n$ points and calculate the corresponding values of the function $f(\theta_1), ..., f(\theta_n)$, the errors $\sigma(f(\theta_1)), ..., \sigma(f(\theta_n))$ are computed as the confidence intervals for fitted function. After that for each θ_i the momentum dependence of the differential cross section was fitted and interpolated to p_{beam} = 1.2 GeV/c. Here, we tried to fit either polynomial of second order using three points for interpolation (see right panel of Fig.6.19) or linear function using two points in the neighborhood of interpolated value. The results of parametrisation, depending on which type of function was used, are presented in right panel of Fig. 6.19. The acceptance corrections were determined using a GEANT-based simulation program for which the parametrised cross section was used as an input distribution. In left panel of Fig. 6.19 the output from the simulation is compared to the data. Based on that comparison we select

the range $\cos\theta_{cm} \in (0.76 - 0.96)$ and for this interval, the integrated total cross section was computed using formula:

$$\sigma = \int_0^{2\pi} d\phi \int_{0.76}^{0.96} \frac{d\sigma}{d\Omega_{cm}} d\cos\theta_{cm} . \tag{6.13}$$

As a result the following values for the integrated cross section of $dd \rightarrow {}^3He n$ were obtained:

$$\begin{aligned} \sigma_1 &= 49.8 \pm 0.33\ \mu b \\ \sigma_2 &= 53.6 \pm 0.17\ \mu b \end{aligned} \tag{6.14}$$

where indices '1' and '2' refer to the type of function (polynomial or linear) used for fitting distribution presented in right panel of Fig. 6.19. The uncertainties of cross sections were computed numerically during the integration of distribution shown in left panel of Fig. 6.19. In this spectrum the information about the error propagation from all steps of parametrization method is included.

Taking into account N_{exp} = 174062 of the detected (in the range $\cos\theta_{cm} \in (0.76 - 0.96)$) $dd \rightarrow {}^3He n$ events and prescaling factor of 100, we obtained following result for integrated luminosity:

$$L_{int} = (350.1 \pm 1.8_{stat.} \pm 24.8_{sys.})\ nb^{-1} \tag{6.15}$$

In the calculation of L_{int} for the cross section the value of σ_1 has been used. The systematic error is connected to the difference between cross sections calculated using either linear or polynomial parametrization. The statistical error is related to the number of detected ^3He. The total uncertainty of the normalisation can be obtained by adding the uncertainties of Ref. [84] data which is 7% in the absolute normalisation.

7 Results of the analysis

In this chapter the results of the comparison of the collected data with physical models are discussed. The total cross section as well as possible reaction mechanisms for the reaction $dd \rightarrow {}^3He n\pi^0$ investigated at beam momentum of 1.2 GeV/c are presented.

7.1 The Total Cross Section of $dd \rightarrow {}^3He n\pi^0$

As already mentioned in previous chapter the total cross section for given reaction can be calculated according to the following relation:

$$\sigma = \frac{N_{exp}}{\varepsilon \, L_{int}} \tag{7.1}$$

with L_{int} being the integrated luminosity, ε - the overall efficiency and N_{exp} the total number of reconstructed events. After applying all selection criteria described in chapter 6 and taking into account the symmetrization of events as presented in beginning of section 6.4, we have obtained N_{exp} = 331206 events of interest. This information combined with the value of the luminosity given by Eq. 6.15 and acceptance correction factor of 24.8%, leads to the following result for the total cross section:

$$\sigma_{tot} = (3.81 \pm 0.01_{stat.} \pm 0.42_{sys.}) \; \mu b \tag{7.2}$$

In the next section the main sources of systematic uncertainties are discussed.

7.2 Systematic Uncertainties

Along with the statistical fluctuations associated with a sample of limited size there are a number of effects that could lead to systematic uncertainties on the final result of the total and differential cross section. In this work, one of the dominant source of systematic error originates from the luminosity evaluation. The error estimated from the luminosity estimation procedure, was found to be $\sim 7\%$. Onto this result, additional 7% from the overall uncertainty in the absolute normalization of data [84] used for luminosity evaluation should be propagated.

Another important component of systematic error is associated with the cut on the probability distribution. In the kinematic fit procedure, hypothesis that event can be considered as dd $\rightarrow {}^3\mathrm{He}n\pi^0$ was confirmed by requiring that the $P(\chi^2|N)$ distribution is flat. In Section 6.3.3 the probability distribution was considered flat for probabilities $P(\chi^2|N) \geq 0.1$. In order to estimate how this cut affects the results, different regions of the probability distribution were tested. In Fig. 7.1 different conditions applied to the $\mathrm{P}(\chi^2|\mathrm{N})$

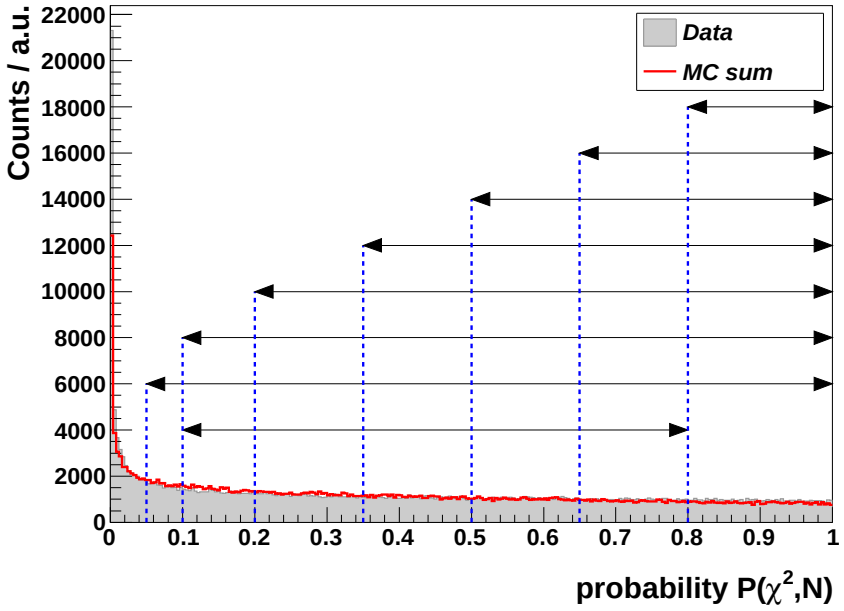

Figure 7.1: The probability distribution obtained from the analysis of the selected data. The gray histograms represent the data while in red the MC distribution is shown. The black arrows show the different regions of $\mathrm{P}(\chi^2|\mathrm{N})$ distribution which were used for the systematic error studies.

distribution are indicated by black arrows. For each marked region, the analysis have been repeated and the number of reconstructed events in the experiment, overall efficiency and the total cross section were determined. The corresponding results are gathered in Table 7.1. The cross section values obtained for different selection region were compared to the nominal value calculated for confidence level $\geq 10\%$. From the comparison the contribution of uncertainty was estimated to be below 5%. This number corresponds to the cut $\geq 80\%$ on probability distribution for which the deviation of cross section with respect to the reference value $P(\chi^2|N) \geq 0.1$ is maximal.

Systematical errors due to the acceptance corrections were checked by varying the starting values for the fit parameters $\mathrm{A}_0, .., \mathrm{A}_7$ in relation 6.6. Subsequently, the acceptance corrections maps (see Fig. 6.16) for slightly different fit coefficients were compared. The deviations turned out to be smaller then 0.1%.

$\mathbf{P(\chi^2\|N) \geq X}$ [%]	$\mathbf{N_{rec}}$	**Overall Eff.**[%]	$\sigma_{\mathbf{tot}}$ [μ**b**]
0.05	355883	26.6	3.82 $\pm$ 0.27
0.1	**331206**	**24.8**	**3.81 $\pm$ 0.27**
0.2	285876	16.2	3.87 $\pm$ 0.28
0.35	225836	16.4	3.91 $\pm$ 0.28
0.5	170118	12.3	3.94 $\pm$ 0.28
0.65	114410	8	3.96 $\pm$ 0.28
0.8	65662	4.68	4.0 $\pm$ 0.28
0.1 - 0.8	220214	16.6	3.8 $\pm$ 0.27

Table 7.1: The number of reconstructed events, the overall efficiency and the total cross section calculated for various cuts (see Fig. 7.1) on the probability distribution. The errors given for cross sections include only uncertainties from luminosity estimation.

Additionally, series of cross-checks regarding cut on energy deposit of ^{3}He have been performed. This condition was very important because it allowed to completely eliminate background. Variation of the limits for this cut did not show any significant influence on the value of the cross section. Taking into account all aforementioned sources of uncertainties the the total systematic error for the cross section was estimated to be 11%.

7.3 Differential Cross Section Distributions

In order to obtain the final differential cross section, the distributions shown in Fig. 6.12 - Fig. 6.14 have been corrected for the acceptance. These distributions were compared with a combination of two purely phenomenological models, namely the quasi-free approach and the model based on partial wave expansion for three-body reaction. As discussed in 6.4 the absolute value of the quasi-free contribution was fixed by use of the parametrized cross section for the experimental data for pd $\rightarrow^3$ Heπ^0 reaction. The integrated quasi-free (with neutron being spectator either from target or beam) cross section contributing to the investigated reaction amount to 2$\times$580 nb, what corresponds to 30% of the total cross section for dd $\rightarrow^3$ Henπ^0 reaction. The rest of the observed cross section should be attributed to some other processes in which all entrance channel nucleons and all exit channel particles are involved. The properties of these other processes were investigated using partial wave expansion and fitting various contributions to the experimental differ-

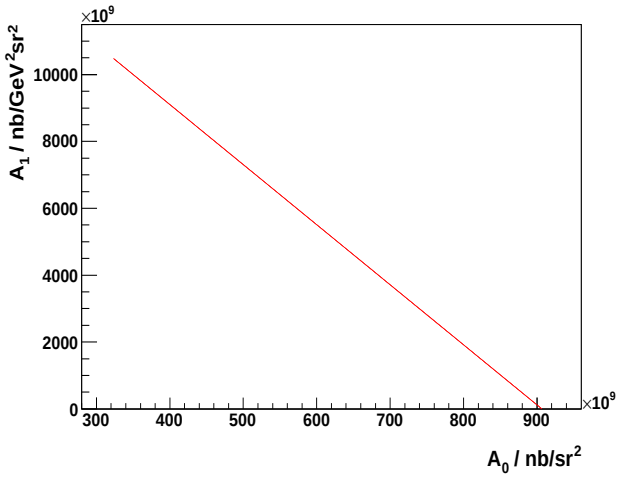

Figure 7.2: The correlation between parameters A_0 and A_1 obtained from the fit of M_{23} distribution. The allowed region for those parameters was determined based on assumption that they both should be positive and on the χ^2 value of the fit.

ential distributions. Exploiting the fact that reaction dd $\rightarrow {}^3\mathrm{He}n\pi^0$ have been measured close to the threshold, the partial wave expansion was limited to the processes with total angular momentum not larger than one in the final state. This implies that six independent parameters (see Appendix A) should be used for full description of the differential cross section given by equation 5.17. The fixed value of the quasi-free cross section was used while amplitudes $A_0,\ldots,A_6$ were fitted to the differential distributions with the previously described set of variables: M_{23}, $\cos\theta_p$, $\cos\theta_q$, φ and $\cos\theta_p \pm \cos\theta_q$.

To obtain all terms A_i occurring in equations 5.17, the differential distributions were fitted simultaneously using relations 5.23 - 5.27. After the fit has been performed, the covariance matrix of fit parameters was inspected in order to determine whether the variables are dependent on one another. As can be seen from Table 7.2 the fit parameters A_0, A_1, A_3 are almost fully correlated and for the rest parameters the correlation was not observed. A reason for such correlation is that the shape of M_{23} spectrum is only the one, which determines the values of A_0, A_1 and A_3 parameters. We tried to get rid of correlation by splitting the fit into two steps. In first step all differential distributions except of M_{23} were fitted simultaneously. In the fit functions 5.24 - 5.27 the linear combination $A_0 I_{sS} + A_1 I_{pS} + A_3 I_{sP}$ was replaced by one parameter A_{013}. Than only four parameters A_2, A_4, A_6, A_5 and A_{013} were fixed by the fit, which appeared to be not correlated. The parameter A_3 was then calculated as

$$A_3 = \frac{1}{I_{sP}}\left(A_{013} - A_0 I_{sS} - A_1 I_{pS}\right) \tag{7.3}$$

and replaced into equation 5.23. In that way the fit function for M_{23} contained only two

	A_0	A_1	A_2	A_3	A_4	A_5	A_6
A_0	1.000	-0.913	0.013	-0.895	0.000	0.000	0.014
A_1	-0.913	1.000	0.038	0.648	-0.002	-0.032	-0.056
A_2	0.013	0.038	1.000	0.006	-0.046	-0.069	0.074
A_3	-0.895	0.648	0.006	1.000	0.007	0.029	0.115
A_4	0.000	-0.002	-0.046	0.007	1.000	0.031	-0.137
A_5	0.000	-0.032	-0.069	0.029	0.031	1.000	0.009
A_6	0.014	-0.056	0.074	0.115	-0.137	0.009	1.000

Table 7.2: The covariance matrix obtained for fit parameters. The fit parameters $A_0, .., A_6$ are defined in Section 5.4.2).

free parameters A_0 and A_1. Subsequently, the M_{23} distribution have been fitted requiring that A_0, A_1 and A_3 are positive, since all these parameters are expressed via a_α^2 amplitudes (see equations A.1, A.2 and A.4). Unfortunately, the fit results for A_0 and A_1 parameters turn out to be still correlated. Hence, we checked this correlation by fixing parameter A_1 and allowing to vary A_0 in the fit of M_{23} distribution. In this procedure it was required that the χ^2 in the fit cannot be larger than $2 \cdot \chi^2_{\text{min}}$. The χ^2_{min} is the value obtained from the fit for case where no any condition on fit parameters was imposed. The resulting dependence of the fixed A_1 parameter as a function of A_0 parameter are shown in Fig. 7.2. The observed correlation may be represented by $A_1 = 16.0 \cdot 10^{12} - 17.6 \times A_0$ dependence. The limits of the correlation presented in Fig. 7.2 were used to compute the coverage of parameter A_3. The final results for all coefficients A_i are gathered in Table 7.3. It is seen that uncorrelated parameters A_2, A_4, A_5 are determined with the accuracy better than 3% and A_6 parameter have uncertainty of about 10%. For the parameters A_0, A_1, A_3 which are correlated only their ranges were determined. The parameters A_0 and A_3 may be varied by factor 3 within given range, however the uncertainty for their certain values are about few percent. The value of parameter A_1 is badly determined and it can be varied in a very broad range.

The comparison of the experimental differential distributions with quasi-free contribution, fitted partial wave based model and their sum for "assignment number" equals to two (see Tab. 5.1) are presented in Fig. 7.3. Similar results were obtained for the comparison of the experimental differential distributions with model prediction for "assignment number" equal one and three (see Tab. 5.1). Contributions from quasi-free model, partial wave decomposition and their sum are shown in blue, green and red, respectively. In the left upper panel of Fig. 7.3 the cosine of angle θ_p between ^{3}He momentum in the center-of-mass of subsystem $^3\text{He} - \pi^0$ and beam momentum (z-axis) is displayed. The shape of the quasi-free contribution and the partial wave model are quite similar and reveal the shape of the experimental distribution and their sum very well describes the data.

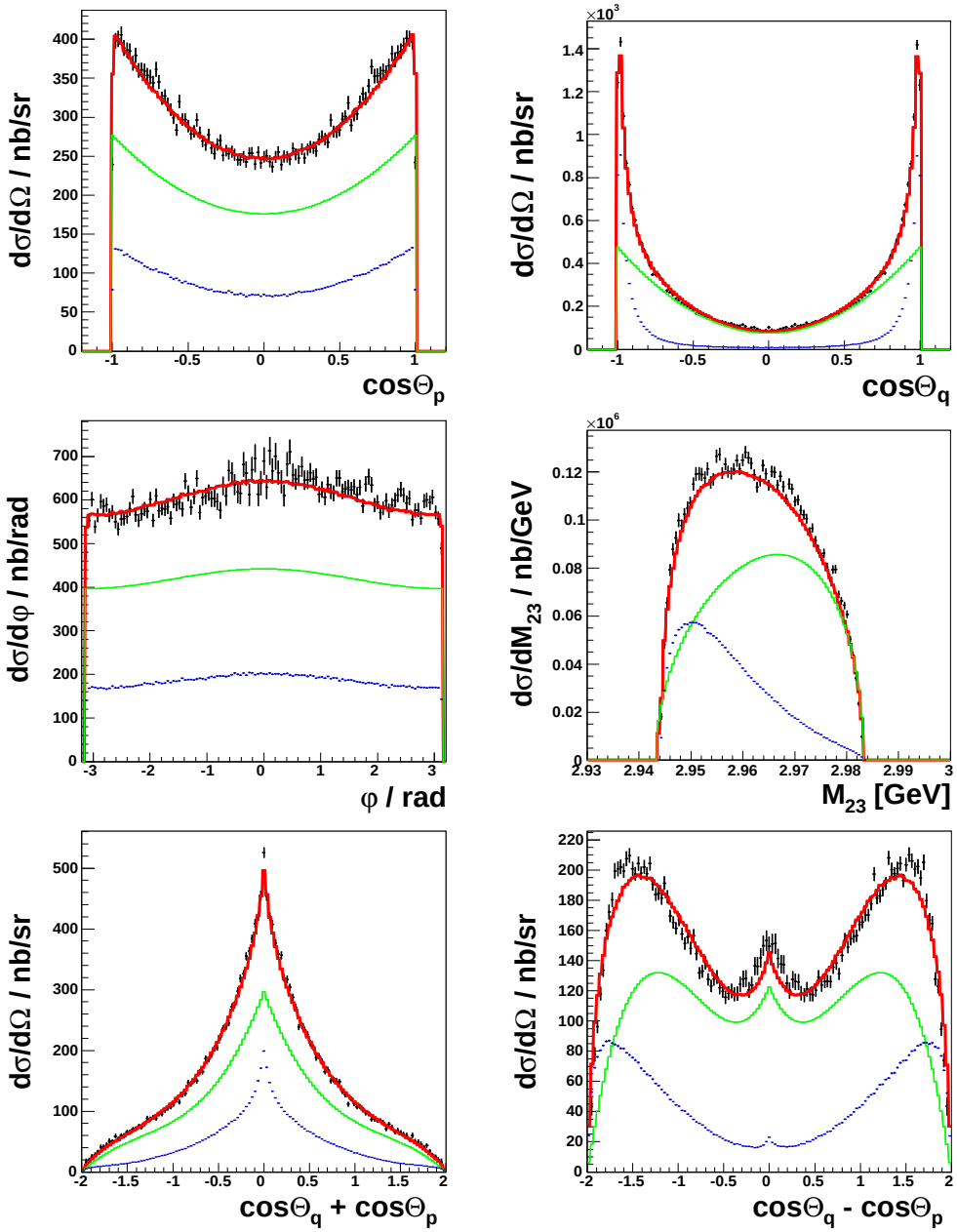

Figure 7.3: The experimental distributions (black) corrected for acceptance are compared to theoretical predictions (red line) based on phenomenological models which were described in details in Chapter 5. The plots are made for "assignment number" equals to two (see Tab. 5.1). Individual contributions from partial wave decomposition and quasi-free model are shown in green and blue, respectively.

Fit results		
sS wave	$\mathbf{A_0}$ [$\mathbf{nb/sr^2}$] $(3.23 - 9.27)\cdot 10^{11} \pm 1.12\cdot 10^{10}$	
pS wave	$\mathbf{A_1}$ [$\mathbf{nb/GeV^2sr^2}$] $2.53\cdot 10^{9} - 10^{13}$	$\mathbf{A_2}$ [$\mathbf{nb/GeV^2sr^2}$] $4.76\cdot 10^{13} \pm 3.03\cdot 10^{11}$
Sp wave	$\mathbf{A_3}$ [$\mathbf{nb/GeV^2sr^2}$] $(2.72 - 7.80)\cdot 10^{13} \pm 2.11\cdot 10^{12}$	$\mathbf{A_4}$ [$\mathbf{nb/GeV^2sr^2}$] $6.07\cdot 10^{13} \pm 1.53\cdot 10^{12}$
$pS+Sp$ interference	$\mathbf{A_5}$ [$\mathbf{nb/GeV^2sr^2}$] $-1.24\cdot 10^{14} \pm 1.12\cdot 10^{12}$	$\mathbf{A_6}$ [$\mathbf{nb/GeV^2sr^2}$] $8.74\cdot 10^{12} \pm 9.05\cdot 10^{11}$

Table 7.3: Amplitudes obtained in the fit of experimental differential cross sections with the model based on partial wave decomposition. The uncertainties correspond to one sigma deviations of the fitted parameters (there is no uncertainty for parameter A_1 since it was fixed on certain values). For the parameters A_0, A_1 and A_3 which are correlated in the fit only their range is given.

While the quasi-free contribution is of about 30% of the observed cross section the observed agreement with the data demonstrate the importance of the *p*-wave in $^3\mathrm{He}-\pi^0$ subsystem. The right upper panel of Fig. 7.3 shows the cosine of angle θ_q between neutron momentum in global center-of-mass system and beam momentum. One can notice that distribution rises steeply at the borders. This shape could not be reproduced only by *p*-wave contribution alone. It is seen that for the observed rising of the differential cross section at small and large θ_q angles the quasi-free process is responsible. It is most likely that in the quasi-free contribution higher partial waves are involved what causes the shape is more steeper then the quadratic dependence on $\cos\theta_q$ expected for *p*-wave contribution. For θ_q angles around 90° the experimental cross section is completely dominated by model based on partial wave decomposition. Very good agreement of the model with the experimental differential cross section as function of $\cos\theta_q$ demonstrate the validity of the applied model and the importance of the neutron *p*-wave contribution to the reaction mechanism. In the middle row (left panel) of Fig. 7.3 the relative angle φ between planes defined by ^{3}He momentum and beam momentum and by neutron momentum and beam momentum is presented. The experimental points are fairly well described by sum of quasi-free and partial wave contributions. As it is seen the observed anisotropy may arise for quasi-free reaction and when *pS* and *sP* interference is present. The contribution of *pS* and *sP* interference dominates the experimental differential cross section. In the right panel of the middle row the invariant mass of the $^3\mathrm{He}-\pi^0$ subsystem is plotted. It is seen that quasi-free reaction contributes mainly for low $^3\mathrm{He}-\pi^0$ invariant mass, where

it accounts for about 50% of the observed cross section. Higher invariant masses are very well reproduced by the part of the model based on partial wave decomposition. One can notice, that theoretical curve shows small deviation from experimental distribution. One of the reason for that can be the assumption that transition amplitudes are proportional to $p^{L_{23}} q^{L_1}$. Such dependence is only some approximation and it may happen that this approach is not strictly fulfilled. Additional effects which are not implemented in the model as e.g. final state interaction or presence of the resonances in any subsystem of two final particles may also influence the $^3\mathrm{He} - \pi^0$ invariant mass distribution. In the lower row of Fig. 7.3 $\cos\theta_p + \cos\theta_q$ and $\cos\theta_p - \cos\theta_q$ distributions are presented. They were used for extraction of the term with the amplitude A_5 which does not appear in any of the single cross section formulae for variables described before. The A_5 term is assigned to the correlation between θ_p and θ_q angles and it is present only for *pS* and *sP* interference.

8 Summary and Outlook

In this thesis the reaction dd $\rightarrow {}^3\mathrm{He}n\pi^0$ measured at p_d = 1.2 GeV/c beam momentum have been investigated using the WASA at COSY facility. For the first time the informations on total cross section and differential distributions of dd $\rightarrow {}^3\mathrm{He}n\pi^0$ reaction were obtained. The measured total cross section equals to $\sigma_{tot} = (3.81 \pm 0.02_{stat.} \pm 0.42_{sys.})$ μb was measured with accuracy of about 11%. The various differential distributions exhibit rich structures indicating important contributions of *s*- and *p*- partial waves.

For the comparison of the experimental differential distributions to the theoretical expectations based on the phenomenological approach the combination of quasi-free model and partial wave expansion model for three-body reaction were used. The contribution of the quasi-free model was fixed based on the available data for pd $\rightarrow {}^3\mathrm{He}\pi^0$ reaction. The partial wave expansion up to the final state angular momenta not higher than 1 was used. The amplitudes of this expansion were fitted to the differential experimental distributions, demonstrating the importance of the *p* partial waves in the final state. The overall agreement of the applied model with the experimental differential distributions is very good. Therefore the present phenomenological model may be considered as a guidance for the microscopic description within Chiral Perturbation Theory, which is under construction. The microscopic model should include the quasi-free reaction mechanism, which accounts for 30% of the total cross section and dominates in specific regions of differential distributions especially for some variables. The large part of the microscopic model should include processes in which all entrance and exit channel particles are involved. These processes have to proceed to the final states described by *s* and *p* partial waves. The importance of the observed *pS* and *sP* interferences should put additional constraints to the microscopic model. Depending on the results delivered by the microscopic model the measurements of the dd $\rightarrow {}^3\mathrm{He}n\pi^0$ reaction may be extended by studies of polarization observables. The experimental data on differential analysing powers should allow to separate the contributions of *s* and *p* partial waves, what was not possible with present data.

Apart from providing rich amount of data for description with microscopic model, the measurement allowed to study the experimental conditions for experimental studies of the dd $\rightarrow {}^4\mathrm{He}\pi^0$ reaction which was identified as one of the key issues of the physics program of the WASA-at-COSY collaboration. In order to study this reaction the knowledge of the cross section for dd $\rightarrow {}^3\mathrm{He}n\pi^0$ is a very valuable information because this is

the main background channel. Presently obtained cross section for dd $\rightarrow {}^3\mathrm{He}n\pi^0$ reaction is by factor of $5 \cdot 10^4$ larger than the expected cross section for dd $\rightarrow {}^4\mathrm{He}\pi^0$ reaction at the same beam momentum. This indicates the necessity of very strong background reduction in future investigations of dd $\rightarrow {}^4\mathrm{He}\pi^0$ reaction. Based on the results and the experiences gained during the dd $\rightarrow {}^3\mathrm{He}n\pi^0$ beam time the two-week measurement of dd $\rightarrow {}^4\mathrm{He}\pi^0$ at p_d = 1.2 GeV/c beam momentum have been performed. The obtained data are currently under analysis [85]. Depending on the results, it will be proposed to perform this measurement with higher statistics and polarized beam. This will allow to extract *p*-wave contributions to the Charge Symmetry Breaking amplitude and to fix some parameters of the Chiral Perturbation Theory terms responsible for this symmetry breaking.

A Appendix

An example of partial wave decomposition for dd $\rightarrow {}^3\mathrm{He}n\pi^0$ reaction assigning neutron as particle 1, π^0 as particle 2 and ^{3}He as particle 3 is presented. The calculations were limited to final state maximum angular momentum equal 1. The resulting amplitudes presented in table A.1 may be grouped to *sS* (amplitudes a_1 and a_2), *sP* (amplitudes a_3 and a_{10}) and *pS*-wave (amplitudes a_{11} and a_{18}). In this notation first index correspond to particle 1 angular momentum in global center-of-mass system and the second index correspond to the relative angular momentum of particles 2 and 3 in subsystem 2-3. The $\mathrm{s_i}$ and $\mathrm{l_i}$ are spin and angular momentum in the entrance channel, $\mathrm{s_{23}}$, $\mathrm{L_{23}}$ and $\mathrm{j_{23}}$ denote spin, angular momentum and total angular momentum in subsystem 2-3, $\mathrm{L_1}$ and $\mathrm{j_1}$ are angular momentum and total angular momentum of particle 1 and J correspond to the total angular momentum of the system in initial and final state. The spherical harmonics were normalized by $\int \mathrm{Y_{l,m}}(\theta,\phi)\mathrm{Y^*_{l,m}}(\theta,\phi)\mathrm{d}\Omega = 1$.

$$A_0 = a_1^2 + 3a_2^2 \tag{A.1}$$

$$A_1 = 5a_{12}^2 + 5a_{17}^2 + 5a_{18}^2 + 3a_{14}^2 + 3a_{15}^2 + a_{11}^2 + a_{13}^2 + 5a_{16}^2 \tag{A.2}$$

$$\begin{aligned} A_2 = &-\frac{15}{14}a_{17}^2 + \frac{25}{7}a_{18}^2 - \frac{3}{2}a_{15}^2 + 5a_{16}^2 - \sqrt{70}\Re(a_{12}a_{17}^*) + 6\Re(a_{12}a_{14}^*) - \\ &3\sqrt{2}\Re(a_{12}a_{15}^*) + 2\sqrt{2}\Re(a_{12}a_{13}^*) - \frac{12}{7}\sqrt{5}\Re(a_{17}a_{18}^*) - 3\sqrt{\frac{10}{7}}\Re(a_{17}a_{14}^*) + \\ &3\sqrt{\frac{5}{7}}\Re(a_{17}a_{15}^*) - 4\sqrt{\frac{5}{7}}\Re(a_{17}a_{13}^*) - 12\sqrt{\frac{2}{7}}\Re(a_{18}a_{14}^*) + \frac{12}{\sqrt{7}}\Re(a_{18}a_{15}^*) + \\ &\frac{12}{\sqrt{7}}\Re(a_{18}a_{13}^*) - 3\sqrt{2}\Re(a_{14}a_{15}^*) + 2\sqrt{10}\Re(a_{11}a_{16}^*) \end{aligned} \tag{A.3}$$

$$A_3 = 5a_4^2 + 5a_9^2 + 5a_{10}^2 + 3a_6^2 + 3a_7^2 + a_3^2 + 5a_8^2 + a_5^2 \tag{A.4}$$

amplitude	s_i	l_i	s_{23}	L_{23}	j_{23}	L_1	j_1	J	transition	
a_1	1	1	$\frac{1}{2}$	0	$\frac{1}{2}$	0	$\frac{1}{2}$	0	${}^3P_0 \to {}^1S_1\ {}^1S_1$	sS
a_2	1	1	$\frac{1}{2}$	0	$\frac{1}{2}$	0	$\frac{1}{2}$	1	${}^3P_1 \to {}^1S_1\ {}^1S_1$	
a_3	0	0	$\frac{1}{2}$	1	$\frac{1}{2}$	0	$\frac{1}{2}$	0	${}^1S_0 \to {}^1S_1\ {}^1P_1$	
a_4	2	0	$\frac{1}{2}$	1	$\frac{3}{2}$	0	$\frac{1}{2}$	2	${}^5S_2 \to {}^1S_1\ {}^1P_3$	
a_5	2	2	$\frac{1}{2}$	1	$\frac{1}{2}$	0	$\frac{1}{2}$	0	${}^5D_0 \to {}^1S_1\ {}^1P_1$	
a_6	2	2	$\frac{1}{2}$	1	$\frac{1}{2}$	0	$\frac{1}{2}$	1	${}^5D_1 \to {}^1S_1\ {}^1P_1$	sP
a_7	2	2	$\frac{1}{2}$	1	$\frac{3}{2}$	0	$\frac{1}{2}$	1	${}^5D_1 \to {}^1S_1\ {}^1P_3$	
a_8	0	2	$\frac{1}{2}$	1	$\frac{3}{2}$	0	$\frac{1}{2}$	2	${}^1D_2 \to {}^1S_1\ {}^1P_3$	
a_9	2	2	$\frac{1}{2}$	1	$\frac{3}{2}$	0	$\frac{1}{2}$	2	${}^5D_2 \to {}^1S_1\ {}^1P_3$	
a_{10}	2	4	$\frac{1}{2}$	1	$\frac{3}{2}$	0	$\frac{1}{2}$	2	${}^5G_2 \to {}^1S_1\ {}^1P_3$	
a_{11}	0	0	$\frac{1}{2}$	0	$\frac{1}{2}$	1	$\frac{1}{2}$	0	${}^1S_0 \to {}^1P_1\ {}^1S_1$	
a_{12}	2	0	$\frac{1}{2}$	0	$\frac{1}{2}$	1	$\frac{3}{2}$	2	${}^5S_2 \to {}^1P_3\ {}^1S_1$	
a_{13}	2	2	$\frac{1}{2}$	0	$\frac{1}{2}$	1	$\frac{1}{2}$	0	${}^5D_0 \to {}^1P_1\ {}^1S_1$	
a_{14}	2	2	$\frac{1}{2}$	0	$\frac{1}{2}$	1	$\frac{1}{2}$	1	${}^5D_1 \to {}^1P_1\ {}^1S_1$	pS
a_{15}	2	2	$\frac{1}{2}$	0	$\frac{1}{2}$	1	$\frac{3}{2}$	1	${}^5D_1 \to {}^1P_3\ {}^1S_1$	
a_{16}	0	2	$\frac{1}{2}$	0	$\frac{1}{2}$	1	$\frac{3}{2}$	2	${}^1D_2 \to {}^1P_1\ {}^1S_1$	
a_{17}	2	2	$\frac{1}{2}$	0	$\frac{1}{2}$	1	$\frac{3}{2}$	2	${}^5D_2 \to {}^1P_3\ {}^1S_1$	
a_{18}	2	4	$\frac{1}{2}$	0	$\frac{1}{2}$	1	$\frac{3}{2}$	2	${}^5G_2 \to {}^1P_3\ {}^1S_1$	

Table A.1: The amplitudes for lowest partial waves for $dd \to {}^3Hen\pi^0$ reaction.

$$A_4 = -\frac{15}{14}a_9^2 + \frac{25}{7}a_{10}^2 - \frac{3}{2}a_7^2 + 5a_8^2 - \sqrt{70}\Re(a_4a_9^*) + 6\Re(a_4a_6^*) -$$
$$3\sqrt{2}\Re(a_4a_7^*) + 2\sqrt{2}\Re(a_4a_5^*) - \frac{12}{7}\sqrt{5}\Re(a_9a_{10}^*) - 3\sqrt{\frac{10}{7}}\Re(a_9a_6^*) +$$
$$3\sqrt{\frac{5}{7}}\Re(a_9a_7^*) - 4\sqrt{\frac{5}{7}}\Re(a_9a_5^*) - 12\sqrt{\frac{2}{7}}\Re(a_{10}a_6^*) + \frac{12}{\sqrt{7}}\Re(a_{10}a_7^*) +$$
$$\frac{12}{\sqrt{7}}\Re(a_{10}a_5^*) - 3\sqrt{2}\Re(a_6a_7^*) + 2\sqrt{10}\Re(a_3a_8^*) \quad \text{(A.5)}$$

$$A_5 = 10\Re(a_{12}a_4^*) - \sqrt{70}\Re(a_{12}a_9^*) + 6\Re(a_{12}a_6^*) + 3\sqrt{2}\Re(a_{12}a_7^*) -$$
$$2\sqrt{2}\Re(a_{12}a_5^*) - \sqrt{70}\Re(a_{17}a_4^*) + \frac{55}{7}\Re(a_{17}a_9^*) - \frac{12}{7}\sqrt{5}\Re(a_{17}a_{10}^*) -$$
$$3\sqrt{\frac{10}{7}}\Re(a_{17}a_6^*) - 3\sqrt{\frac{5}{7}}\Re(a_{17}a_7^*) + 4\sqrt{\frac{5}{7}}\Re(a_{17}a_5^*) - \frac{12}{7}\sqrt{5}\Re(a_{18}a_9^*) +$$
$$\frac{120}{7}\Re(a_{18}a_{10}^*) - 12\sqrt{\frac{2}{7}}\Re(a_{18}a_6^*) - \frac{12}{\sqrt{7}}\Re(a_{18}a_7^*) - \frac{12}{\sqrt{7}}\Re(a_{18}a_5^*) +$$
$$6\Re(a_4a_{14}^*) - 3\sqrt{2}\Re(a_4a_{15}^*) + 2\sqrt{2}\Re(a_4a_{13}^*) - 3\sqrt{\frac{10}{7}}\Re(a_9a_{14}^*) +$$
$$3\sqrt{\frac{5}{7}}\Re(a_9a_{15}^*) - 4\sqrt{\frac{5}{7}}\Re(a_9a_{13}^*) - 12\sqrt{\frac{2}{7}}\Re(a_{10}a_{14}^*) + \frac{12}{\sqrt{7}}\Re(a_{10}a_{15}^*) +$$
$$\frac{12}{\sqrt{7}}\Re(a_{10}a_{13}^*) + 6\Re(a_{14}a_6^*) + 3\sqrt{2}\Re(a_{14}a_7^*) - 3\sqrt{2}\Re(a_{15}a_6^*) -$$
$$3\Re(a_{15}a_7^*) - 2\Re(a_{11}a_3^*) + 2\sqrt{10}\Re(a_{11}a_8^*) - 2\Re(a_{13}a_5^*) -$$
$$2\sqrt{10}\Re(a_{16}a_3^*) + 20\Re(a_{16}a_8^*) \quad \text{(A.6)}$$

$$
\begin{aligned}
A_6 = 10\Re(a_{12}a_4^*) + \sqrt{\frac{35}{2}}\Re(a_{12}a_9^*) - 3\Re(a_{12}a_6^*) - \frac{3}{\sqrt{2}}\Re(a_{12}a_7^*) + \\
\sqrt{2}\Re(a_{12}a_5) + \sqrt{\frac{35}{2}}\Re(a_{17}a_4^*) + \frac{155}{14}\Re(a_{17}a_9^*) + \frac{6}{7}\sqrt{5}\Re(a_{17}a_{10}^*) + \\
3\sqrt{\frac{5}{14}}\Re(a_{17}a_6^*) + \frac{3}{2}\sqrt{\frac{5}{7}}\Re(a_{17}a_7^*) - 2\sqrt{\frac{5}{7}}\Re(a_{17}a_5^*) + \frac{6}{7}\sqrt{5}\Re(a_{18}a_9^*) + \\
\frac{45}{7}\Re(a_{18}a_{10}^*) + 6\sqrt{\frac{2}{7}}\Re(a_{18}a_6^*) + \frac{6}{\sqrt{7}}\Re(a_{18}a_7^*) + \frac{6}{\sqrt{7}}\Re(a_{18}a_5^*) - \\
3\Re(a_4a_{14}^*) + \frac{3}{\sqrt{2}}\Re(a_4a_{15}^*) - \sqrt{2}\Re(a_4a_{13}^*) + 3\sqrt{\frac{5}{14}}\Re(a_9a_{14}^*) - \\
\frac{3}{2}\sqrt{\frac{5}{7}}\Re(a_9a_{15}^*) + 2\sqrt{\frac{5}{7}}\Re(a_9a_{13}^*) + 6\sqrt{\frac{2}{7}}\Re(a_{10}a_{14}^*) - \frac{6}{\sqrt{7}}\Re(a_{10}a_{15}^*) - \\
\frac{6}{\sqrt{7}}\Re(a_{10}a_{13}^*) + \frac{9}{\sqrt{2}}\Re(a_{14}a_7^*) - \frac{9}{\sqrt{2}}\Re(a_{15}a_6^*) + \frac{9}{2}\Re(a_{15}a_7^*) - \\
2\Re(a_{11}a_3^*) - \sqrt{10}\Re(a_{11}a_8^*) - 2\Re(a_{13}a_5^*) + \\
\sqrt{10}\Re(a_{16}a_3^*) + 5\Re(a_{16}a_8^*) \qquad \text{(A.7)}
\end{aligned}
$$

B Appendix

$\theta[deg]$	p_0	p_1	p_2	p_3	p_4
0 - 3	0.00986	0.02559	-0.30381	0.81094	-0.69083
3 - 6	0.01811	-0.08890	0.27422	-0.4288	0.26453
6 - 9	0.01888	-0.09442	0.29539	-0.46711	0.29103
9 - 12	0.02050	-0.11273	0.384692	-0.65619	0.43539
12 - 15	0.02107	-0.11375	0.38188	-0.64270	0.42276
15 - 18	0.02171	-0.11453	0.37251	-0.59934	0.37311

Table B.1: In FWC1 detector for kinetic energy parametrization polynomial of fourth order was used. In the table values of the fit parameters obtained for six angular bins are presented.

$\theta[deg]$	p_0	p_1	p_2	p_3	p_4
0 - 3	0.02078	-0.123175	0.40310	-0.62650	0.36965
3 - 6	0.02211	-0.14430	0.52482	-0.91648	0.61103
6 - 9	0.02262	-0.14961	0.54760	-0.96025	0.64219
9 - 12	0.02326	-0.15656	0.57956	-1.02582	0.69181
12 - 15	0.02366	-0.15807	0.57895	-1.01374	0.67775
15 - 18	0.02410	-0.16000	0.57981	-0.99792	0.65239

Table B.2: In FWC2 detector for kinetic energy parametrization polynomial of fourth order was used. In the table values of the fit parameters obtained for six angular bins are presented.

$\theta[deg]$	p_0	p_1	p_2
0 - 3	-0.29746	3.86830	-11.8258
3 - 6	-0.09547	0.83669	-0.51588
6 - 9	-0.08032	0.60609	0.32362
9 - 12	0.03639	-1.10801	6.54220
12 - 15	0.03260	-1.05575	6.28564
15 - 18	-0.04486	0.07679	2.07313

Table B.3: For particles stopped in FTH1 detector polynomial of second order was used. In the table values of the fit parameters obtained for six angular bins are presented.

$\theta[deg]$	p_0	p_1	p_2
0 - 3	0.00587	0.12212	0.35640
3 - 6	0.00562	0.10549	0.40415
6 - 9	0.00559	0.10823	0.40520
9 - 12	0.00562	0.109261	0.40716
12 - 15	0.00569	0.10921	0.41013
15 - 18	0.00579	0.10900	0.41361

Table B.4: For particles punching through the FTH1 detector power function of the form: $E_{kin}(E_{dep}) = p_0/(E_{dep} - p_1)^{p_2}$) was used. In the table values of the fit parameters obtained for six angular bins are presented.

Bibliography

[1] G. Miller et al., Phys. Rep. **194** (1990) 1.
[2] O. Dumbrajs et al., Nucl. Phys. **B216** (1983) 277.
[3] R. Abegg et al., Phys. Rev. **D39** (1989) 2464.
[4] L. Knutson et al., Phys. Rev. Lett. **66** (1991) 1410.
[5] S. Vigdor et al., Phys. Rev. **C46** (1992) 410.
[6] R. Abegg et al., Phys. Rev. Lett. **75** (1995) 1711.
[7] M. Iqbal et al., Phys. Lett. **B322** (1994) 7.
[8] T. Hatsuda et al., Phys. Rev. **C49** (1994) 452.
[9] J. Niskanen et al., Phys. Rev. **C65** (2002) 037001.
[10] T. Nasu et al., Phys. Rev. **C66** (2003) 024006.
[11] E. Stephenson et al., Phys. Rev. Lett. **91** (2003) 142302.
[12] A. Opper et al., Phys. Rev. Lett. **91** (2003) 212302.
[13] G. Miller et al., Nucl. Phys. **56** (2006) 253.
[14] V. Bernard et al., Int. J. Mod. Phys. **E4** (1995) 193.
[15] P. Bedaque et al., Nucl. Phys. **52** (2002) 339.
[16] C. Hanhart et al., Phys. Rev. **397** (2004) 155.
[17] A. Gårdestig et al., Phys. Rev. **C69** (2004) 044606.
[18] A. Nogga et al., Phys. Lett. **B639** (2006) 465.
[19] W. MacDonald et al., Phys. Rev. **101** (1956) 271.
[20] J. Banaigs et al., Phys. Rev. Lett. **58** (1987) 1922.
[21] L. Goldzahl et al., Nucl. Phys. **A533** (1991) 675.
[22] C. Wilkin et al., Phys. Lett. **B331** (1993) 275.
[23] E. Epelbaum et al., Eur. Phys. J. **A15** (2002) 543.
[24] T. Cohen et al., Phys. Rev. **C53** (1996) 2661.
[25] C. Hanhart et al., Phys. Rev. Lett. **85** (2000) 2905.
[26] C. Hanhart et al., Phys. Rev. **C66** (2002) 054005.
[27] E. Epelbaum et al., Rev. Mod. Phys. **81** (2009) 1773.
[28] U. van Kolck et al., Phys. Lett. **B493** (2000) 65.
[29] D. Bolton et al., Phys. Rev. **C81** (2010) 014001.
[30] A. Fonseca et al., Phys. Rev. Lett. **83** (1999) 4021.
[31] A. Nogga et al., Phys. Rev. Lett. **85** (2000) 944.
[32] A. Nogga et al., Phys. Rev. **C65** (2002) 054003.
[33] C. Bargholtzand et al., Nucl. Inst. Meth. **A594** (2008) 39.

[34] H. Calen, *CELSIUS experiments. Prepared for 6th International Conference on Nuclear Physics at Storage Rings.*, STORI, Julich, Bonn, Germany, 2005.
[35] H.H. Adam et al., *Proposal for the Wide Angle Shower Apparatus (WASA) at COSY-Juelich*, - 'WASA at COSY'. 2004.
[36] R. Maier et al., Nucl. Phys. **A626** (1997) 395c.
[37] D. Prasuhn et al., Nucl. Inst. Meth. **A441** (200) 167.
[38] R. Gebel et al., *Barrier-bucket RF tests*, IKP/COSY Annual Report 2008.
[39] B. Trostell et al., Nucl. Inst. Meth. **A362** (1995) 41.
[40] A. Pricking et al., *Upgrade of the WASA Detector with a New Forward Window Hodoscope.*, Deutsche Physikalische Gesellschaft Tagung, 2008. HK11.7.
[41] M. Janusz et al., *FPC tests*, IKP/COSY Annual Report 2006.
[42] C. Pauly et al., *Scintillator series tests for the FTH renewal.*, IKP/COSY Annual Report 2007.
[43] C. Pauly., *In-beam efficiency study of the WASA trigger hodoscope.*, IKP/COSY Annual Report 2006.
[44] J. Zabierowski et al., Nucl. Inst. Meth. **A606** (2009) 411.
[45] M. Jacewicz, *Measurement of the reaction* $pp \to pp\pi^o\pi^-\pi^+$ *with CELSIUS/WASA at 1.36 GeV.*, PhD thesis, Uppsala Universitet, Sweden, 2004.
[46] R.J.M.Y. Ruber, *An Ultra-thin-walled Superconducting Solenoid for Meson-decay Physics.*, PhD thesis, Uppsala Universitet, Sweden, 1999.
[47] P. Podkopal et al., *Energy calibration of the WASA Plastic Scintillator Barrel*, IKP/COSY Annual Report 2006.
[48] P. Podkopal et al., *The performance of the new Plastic Scintillator Barrel detector of the WASA-at-COSY*, IKP/COSY Annual Report 2008.
[49] I. Koch, *Measurements of* $2\pi^o$ *and* $3\pi^o$ *Production in Proton-Proton Collisions at a Center of Mass Energy of 2.465 GeV.*, PhD thesis, Uppsala Universitet, Sweden,2004.
[50] H. Kleines et al., IEEE Trans. Nucl. Sci. **53** (2006) 893.
[51] M. Drochner et al., IEEE Trans. Nucl. Sci. **45** (1998) 1882.
[52] P. Wustner et al., *System development for COSY experiments*, presented at the 13th IEEE Real Time Conf., Montreal, Canada, May 18-23, 2003.
[53] P. Marciniewski, *Fast digital Trigger Systems for Experiments in High Energy Physics.*, PhD thesis, Uppsala Universitet, Sweden, 2001.
[54] M.A. Kagarlis, *Pluto++ – a Monte Carlo simulation tool for hadronic physics*, http://www-hades.gsi.de/computing/pluto/html/PlutoIndex.html, 2000.
[55] P. Salabura et al., *A High Acceptance DiElectron Spectrometer*, Nucl. Phys. **B44** (1995) 701 .
[56] P. Senger et al., J. Phys. G: Nucl. Part. Phys. **30** (2004) S1087.
[57] http: // root. cern. ch.
[58] Numerical Recipes in C: The Art of Scientific Computing (Cambridge University Press (2nd edition), 1993).
[59] V.N. Nikulin et al., Phys. Rev. **C54** (1996) 1732.
[60] M. Lacombe et al., Phys. Lett. **101B** (1981) 139.

[61] M. Betigeri et al., GEM collaboration, Phys. Lett. **B472** (2000) 267.
[62] Numerical Recipes in C: The Art of Scientific Computing (Cambridge University Press (2nd edition), 1993).
[63] *GEANT – Detector Description and Simulation Tool*, CERN Program W5013, 1994.
[64] Theory and Practice of Scintillation Counting (Oxford, 1964).
[65] V. Hejny et al., *RootSorter: A New Analysis Framework For ANKE*, IKP/COSY Annual Report 2002.
[66] C. Redmer et al., *Measurements on the light attenuation in the elements of the WASA-at-COSY Forward Trigger Hodoscope*, IKP/COSY Annual Report 2006.
[67] B. Jany, *Assembly and measurements of the electromagnetic calorimeter components for WASA at COSY setup*, MSc thesis, 2006.
[68] V. Hejny, Private Communication.
[69] Techniques for Nuclear and Particle Physics Experiments (Universitetsforlaget, 1994).
[70] Particle Kinematics (John Wiley & Sons, 1973).
[71] F. Duncan et al., Phys. Rev. Lett. **80** (1998) 4390.
[72] H. Hahn et al., Phys. Rev. Lett. **82** (1999) 2258.
[73] H. Calén et al., Phys. Rev. **C58** (1998) 2667.
[74] H. Calén et al., Phys. Rev. Lett. **80** (1998) 2069.
[75] V.N. Nikulin et al., Phys. Rev. **C54** (1996) 1732.
[76] M. Betigeri et al., Nucl. Phys. **A690** (2001) 473.
[77] Direct nuclear reactions (Oxford University Press, 1983).
[78] Quantum Collision Theory (North-Holland, 1975).
[79] D. Tilley et al., Nucl. Phys. **A541** (1992) 1.
[80] Mathematica Edition: Version 7.0 (Wolfram Research, Inc., 2008).
[81] Probability and Statistics in Particle Physic (Universitetsforlaget, 1979).
[82] Data analysis (Springer Verlag, 1999).
[83] C. Amsler et al., Phys. Lett. **B667** (2008) 1.
[84] G. Bizard et al., Phys. Rev. **C22** (1980) 1632.
[85] V. Hejny et al., *Charge Symmetry Breaking in* $\mathrm{dd} \to \alpha\pi^0$ *with Wasa-at-Cosy.*, IKP/COSY Annual Report 2009.

Acknowledgements

During writing my thesis i have lost faith that i will reach this chapter so many times it would be hard to count. Fortunately, there were always people who were able to resurrect the spark of hope in me that i can do that (well sometimes that i have to do that ☺). This is the chapter where I would like to express my gratitude to those people.

First and foremost I would like to thank the supervisor of my PhD studies, Prof. Andrzej Magiera who helped me to find an interesting topic and provided ceaseless help in both structuring and writing this thesis. His knowledge and physics intuition were invaluable during countless discussion we have had. Without his guidance I most likely would have been lost and discouraged.

I express my gratitude to Prof. Hans Ströher for a great opportunity to work in research field of Nuclear Physics at the Institute für Kernphysik in Forschungszentrum Jülich.

I am grateful to Prof. Bogusław Kamys for possibility to prepare this dissertation in the Faculty of Physics, Astronomy and Applied Computer Science of the Jagellonian University.

I am very grateful to Dr. Volker Hejny, my tutor during the stay in Jülich. I have approached you with thousands of questions, and you always knew the answers. Thank you for teaching me an elegant way of programming and for being extraordinarily patient with every mistake I made or idea I misunderstood. It would not have been possible to write this doctoral thesis without your help.

I would like to thank the "boss" of WASA collaboration Dr. Magnus Wolke for creating friendly atmosphere during my stay in Uppsala at the very begin of my way in the world of particle physics.

I am highly indebted to Aleksandra Wrońska and Christian Pauly for several important suggestions.

My sincere thanks are due to Marek Jacewicz and Tytus Smoliński for assistance during the assembling of PSC detector. I would also like to thank others WASA-at-COSY collaborators who have contributed to this work. A warm thank you to all my friends (especially Michał Śmiechowicz) and colleagues in the Institute to keep me in shape.

Finally I would like to extend my deepest gratitude to my Family.